



# A perspective on computational algorithms for aerodynamic analysis and design<sup>☆</sup>

Antony Jameson\*

*Department of Aeronautics and Astronautics, Stanford University, Durand Building, Stanford, CA 94305-4035, USA*

---

## Abstract

This paper examines the use of computational fluid dynamics as a tool for aircraft design. It addresses the requirements for effective industrial use, and trade-offs between modeling accuracy and computational costs. Essential elements of algorithm design are discussed in detail, together with a unified approach to the design of shock capturing schemes. Finally, the paper discusses the use of techniques drawn from control theory to determine optimal aerodynamic shapes. In the future multidisciplinary analysis and optimization should be combined to take account of the trade-offs in the overall performance of the complete system. © 2001 Elsevier Science Ltd. All rights reserved.

---

## Contents

1. Introduction . . . . .	198
2. The complexity of fluid flow and mathematical modeling. . . . .	199
2.1. The hierarchy of mathematical models . . . . .	199
2.2. Computational costs . . . . .	199
2.3. Turbulence modeling. . . . .	200
3. CFD algorithms . . . . .	201
3.1. Difficulties of flow simulation. . . . .	201
3.2. Structured and unstructured meshes. . . . .	201
3.3. Finite difference, finite volume, and finite element schemes. . . . .	202
3.4. Nonoscillatory shock capturing schemes . . . . .	203
3.5. Multidimensional schemes. . . . .	210
3.6. Discretization of the viscous terms. . . . .	210
3.7. Time-stepping schemes. . . . .	211
3.8. Multigrid methods . . . . .	213
3.9. Preconditioning. . . . .	214
3.10. High order schemes and mesh refinement . . . . .	215
4. Current status of numerical simulation. . . . .	216
4.1. One-dimensional shock . . . . .	216
4.2. Euler calculations for airfoils and wings. . . . .	216
4.3. Viscous flow calculations . . . . .	217
4.4. Ship wave resistance calculations. . . . .	217

---

<sup>☆</sup>This paper initially appeared with the same title at the Sixth Taiwan National Conference on Computational Fluid Dynamics, Taitung, Taiwan ROC, August 1999.

\* Tel.: + 1-650-725-6208; fax: + 1-650-725-3377.

E-mail address: [jameson@baboon.stanford.edu](mailto:jameson@baboon.stanford.edu) (A. Jameson).

5. Aerodynamic shape optimization . . . . .	218
5.1. Optimization and design. . . . .	218
5.2. Application of control theory . . . . .	220
5.3. Three-dimensional design using the compressible Euler and Navier–Stokes equations . . . . .	223
5.4. Optimization procedures. . . . .	225
5.5. Industrial experience and results of optimization . . . . .	227
6. Outlook and conclusions . . . . .	236
Acknowledgements . . . . .	237
References. . . . .	237

## 1. Introduction

Computational methods first began to have a significant impact on aerodynamics analysis and design in the period of 1965–75. This decade saw the introduction of panel methods which could solve the linear flow models for arbitrarily complex geometry in both subsonic and supersonic flow [1–3]. It also saw the appearance of the first satisfactory methods for treating the nonlinear equations of transonic flow [4–9], and the development of the hodograph method for the design of shock free supercritical airfoils [10].

Algorithms have been the subject of intensive development for the past two decades. The principles underlying the design and implementation of robust schemes which can accurately resolve shock waves and contact discontinuities in compressible flows are now quite well established. It is also quite well understood how to design high order schemes for viscous flow, including compact schemes and spectral methods. Adaptive refinement of the mesh interval ( $h$ ) and the order of approximations ( $p$ ) has been successfully exploited both separately and in combination in the  $h$ – $p$  method [11]. A continuing obstacle to the treatment of configurations with complex geometry has been the problem of mesh generation. Several general techniques have been developed, including algebraic transformations and methods based on the solution of elliptic and hyperbolic equations. In the last few years methods using unstructured meshes have also begun to gain more general acceptance. The Dassault-INRIA group led the way in developing a finite element method for transonic potential flow. They obtained a solution for a complete Falcon 50 as early as 1982 [12]. Euler methods for unstructured meshes have been the subject of intensive development by several groups since 1985 [13–17], and Navier–Stokes methods on unstructured meshes have also been demonstrated [18–20].

Computational fluid dynamics (CFD) is now widely accepted as a key tool for aerodynamic design. Its effectiveness is still hampered, however, by the long set-up and high costs, both human and computational of complex flow simulations. The essential requirements for

industrial use are:

1. assured accuracy,
2. acceptable computational and human costs,
3. fast turn around.

Improvements are still needed in all three areas. In particular, the fidelity of modeling of high Reynolds number viscous flows continues to be limited by computational costs. Consequently, accurate and cost effective simulation of viscous flow at Reynolds numbers associated with full scale flight, such as the prediction of high lift devices, remains a challenge. Several routes are available toward the reduction of computational costs, including the reduction of mesh requirements by the use of higher order schemes, improved convergence to a steady state by sophisticated acceleration methods, fast inversion methods for implicit schemes, and the exploitation of massively parallel computers.

Another factor limiting the effective use of CFD is the lack of good interfaces to computer aided design (CAD) systems. The geometry models provided by existing CAD systems often fail to meet the requirements of continuity and smoothness needed for flow simulation, with the consequence that they must be modified before they can be used to provide the input for mesh generation. This bottleneck, which impedes the automation of the mesh generation process, needs to be eliminated, and the CFD software should be fully integrated in a numerical design environment. In addition to more accurate and cost-effective flow prediction methods, better optimizations methods are also needed, so that not only can designs be rapidly evaluated, but directions of improvement can be identified. Possession of techniques which result in a faster design cycle gives a crucial advantage in a competitive environment.

A critical issue, examined in the next section, is the choice of mathematical models. What level of complexity is needed to provide sufficient accuracy for aerodynamic design, and what is the impact on cost and turn-around time? Section 3 addresses the design of numerical algorithms for flow simulation. Section 4 presents the results of some numerical calculations which require moderate computer resources and could be completed with the fast

turn-around required by industrial users. Section 5 discusses automatic design procedures which can be used to produce optimum aerodynamic designs. Finally, Section 6 offers an outlook for the future.

## 2. The complexity of fluid flow and mathematical modeling

### 2.1. The hierarchy of mathematical models

Many critical phenomena of fluid flow, such as shock waves and turbulence, are essentially nonlinear. They also exhibit extreme disparities of scales. While the actual thickness of a shock wave is of the order of a mean free path of the gas particles, on a macroscopic scale its thickness is essentially zero. In turbulent flow energy is transferred from large scale motions to progressively smaller eddies until the scale becomes so small that the motion is dissipated by viscosity. The ratio of the length scale of the global flow to that of the smallest persisting eddies is of the order  $Re^{3/4}$ , where  $Re$  is the Reynolds number, typically in the range of 30 million for an aircraft. In order to resolve such scales in all three space directions a computational grid with the order of  $Re^{9/4}$  cells would be required. This is beyond the range of any current or foreseeable computer. Consequently, mathematical models with varying degrees of simplification have to be introduced in order to make computational simulation of flow feasible and produce viable and cost-effective methods.

Fig. 1 (supplied by Pradeep Raj) indicates a hierarchy of models at different levels of simplification which have proved useful in practice. Efficient flight is generally achieved by the use of smooth and streamlined shapes which avoid flow separation and minimize viscous effects, with the consequence that useful predictions can be made using inviscid models. Inviscid calculations with boundary layer corrections can provide quite accurate predictions of lift and drag when the flow remains attached, but iteration between the inviscid outer solution and the inner boundary layer solution becomes increasingly difficult with the onset of separation. Procedures for solving the full viscous equations are likely to be needed for the simulation of arbitrary complex separated flows, which may occur at high angles of attack or with bluff bodies. In order to treat flows at high Reynolds numbers, one is generally forced to estimate turbulent effects by Reynolds averaging of the fluctuating components. This requires the introduction of a turbulence model. As the available computing power increases one may also aspire to large eddy simulation (LES) in which the larger scale eddies are directly calculated, while the influence of turbulence at scales smaller than the mesh interval is represented by a subgrid scale model.

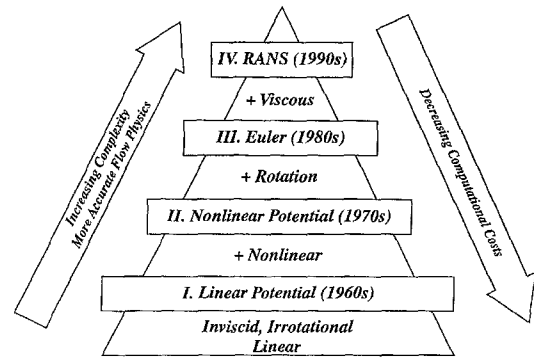


Fig. 1. Hierarchy of fluid flow models.

### 2.2. Computational costs

Computational costs vary drastically with the choice of mathematical model. Panel methods can be effectively used to solve the linear potential flow equation with higher-end personal computers (with an Intel Pentium microprocessor, for example). Studies of the dependency of the result on mesh refinement, performed by this author and others, have demonstrated that inviscid transonic potential flow or Euler solutions for an airfoil can be accurately calculated on a mesh with 160 cells around the section, and 32 cells normal to the section. Using multigrid techniques 10–25 cycles are enough to obtain a converged result. Consequently, airfoil calculations can be performed in seconds on a Cray YMP, and can also be performed on Pentium-class personal computers. Correspondingly, accurate three-dimensional inviscid calculations can be performed for a wing on a mesh, say with  $192 \times 32 \times 48 = 294,912$  cells, in about 5 min on a single processor Cray YMP, or less than a minute with eight processors, or in less than an hour on a workstation such as a Silicon Graphics Indigo 2.

Viscous simulations at high Reynolds numbers require vastly greater resources. Careful two-dimensional studies of mesh requirements have been carried out at Princeton by Martinelli [21]. He found that on the order of 32 mesh intervals were needed to resolve a turbulent boundary layer, in addition to 32 intervals between the boundary layer and the far field, leading to a total of 64 intervals. In order to prevent degradations in accuracy and convergence due to excessively large aspect ratios (in excess of 1000) in the surface mesh cells, the chordwise resolution must also be increased to 512 intervals. Reasonably, accurate solutions can be obtained in a  $512 \times 64$  mesh in 100 multigrid cycles. Translated to three dimensions, this would imply the need for meshes with 5–10 million cells (for example,  $512 \times 64 \times 256 = 8,388,608$  cells as shown in Fig. 2). When simulations are performed on less fine meshes with, say, 500,000 to 1 million cells, it is very hard

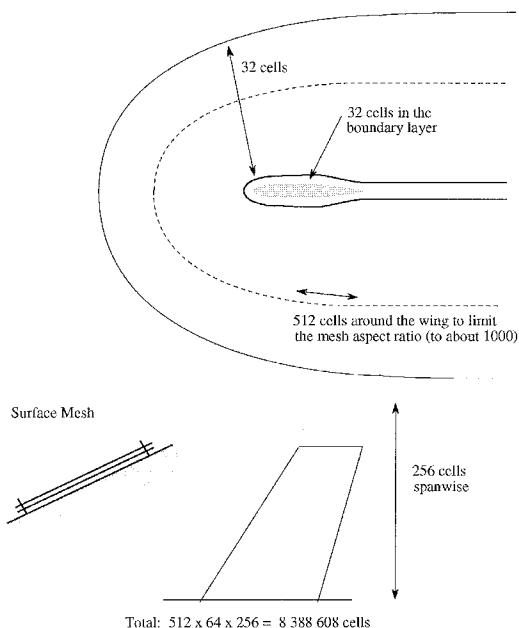


Fig. 2. Mesh requirements for a viscous simulation.

to avoid mesh dependency in the solutions as well as sensitivity to the turbulence model.

A typical algorithm requires of the order of 5000 floating point operations per mesh point in one multigrid iteration. With 10 million mesh points, the operation count is of the order of  $0.5 \times 10^{11}$  per cycle. Given a computer capable of sustaining  $10^{11}$  operations per second (100 gigaflops), 200 cycles could then be performed in 100 s. Simulations of unsteady viscous flows (flutter, buffet) would be likely to require 1000–10,000 time steps. A further progression to large eddy simulation of complex configurations would require even greater resources. The following estimate is due to Jou [22]. Suppose that a conservative estimate of the size of eddies in a boundary layer that ought to be resolved is  $1/5$  of the boundary layer thickness. Assuming that 10 points are needed to resolve a single eddy, the mesh interval should then be  $1/50$  of the boundary layer thickness. Moreover, since the eddies are three dimensional, the same mesh interval should be used in all three directions. Now, if the boundary layer thickness is of the order of  $0.01$  of the chord length, 5000 intervals will be needed in the chordwise direction, and for a wing with an aspect ratio of 10, 50,000 intervals will be needed in the spanwise direction. Thus, of the order of  $50 \times 5000 \times 50,000$  or 12.5 billion mesh points would be needed in the boundary layer. If the time dependent behavior of the eddies is to be fully resolved using time steps on the order of the time for a wave to pass through a mesh interval, and one allows for a total time equal to the time required for waves to

travel three times the length of the chord, of the order of 15,000 time steps would be needed. A more refined estimate which allows for the varying thickness of the boundary layer, recently made by Spalart et al. [23], suggests an even more severe requirement. Performance beyond the teraflop ( $10^{12}$  operations per second) will be needed to attempt calculations of this nature, which also have an information content far beyond what is needed for engineering analysis and design. The designer does not need to know the details of the eddies in the boundary layer. The primary purpose of such calculations is to improve the calculation of averaged quantities such as skin friction, and the prediction of global behavior such as the onset of separation. The main current use of Navier–Stokes and large eddy simulations is to try to gain an improved insight into the physics of turbulent flow, which may in turn lead to the development of more comprehensive and reliable turbulence models.

### 2.3. Turbulence modeling

It is doubtful whether a universally valid turbulence model, capable of describing all complex flows, could be devised [24]. Algebraic models [25,26] have proved fairly satisfactory for the calculation of attached and slightly separated wing flows. These models rely on the boundary layer concept, usually incorporating separate formulas for the inner and outer layers, and they require an estimate of a length scale which depends on the thickness of the boundary layer. The estimation of this quantity by a search for a maximum of the vorticity times a distance to the wall, as in the Baldwin–Lomax model, can lead to ambiguities in internal flows, and also in complex vortical flows over slender bodies and highly swept or delta wings [27,28]. The Johnson–King model [29], which allows for nonequilibrium effects through the introduction of an ordinary differential equation for the maximum shear stress, has improved the prediction of flows with shock induced separation [30,31].

Closure models depending on the solution of transport equations are widely accepted for industrial applications. These models eliminate the need to estimate a length scale by detecting the edge of the boundary layer. Eddy viscosity models typically use two equations for the turbulent kinetic energy  $k$  and the dissipation rate  $\varepsilon$ , or a pair of equivalent quantities [32–37]. Models of this type generally tend to present difficulties in the region very close to the wall. They also tend to be badly conditioned for numerical solution. The  $k-l$  model [38] is designed to alleviate this problem by taking advantage of the linear behavior of the length scale  $l$  near the wall. In an alternative approach to the design of models which are more amenable to numerical solution, new models requiring the solution of one transport equation have recently been introduced [39,40]. The performance of the algebraic models remains competitive for wing flows, but

the one- and two-equation models show promise for broader classes of flows. In order to achieve greater universality, research is also being pursued on more complex Reynolds stress transport models, which require the solution of a larger number of transport equations.

Another direction of research is the attempt to devise more rational models via renormalization group (RNG) theory [41,42]. Both algebraic and two-equation  $k-\epsilon$  models devised by this approach have shown promising results [43].

The selection of sufficiently accurate mathematical models and a judgment of their cost-effectiveness ultimately rests with industry. Aircraft and spacecraft designs normally pass through the three phases of conceptual design, preliminary design, and detailed design. Correspondingly, the appropriate CFD models will vary in complexity. In the conceptual and preliminary design phases, the emphasis will be on relatively simple models which can give results with very rapid turnaround and low computer costs, in order to evaluate alternative configurations and perform quick parametric studies. The detailed design stage requires the most complete simulation that can be achieved with acceptable cost. In the past, the low level of confidence that could be placed on numerical predictions has forced the extensive use of wind tunnel testing at an early stage of the design. This practice was very expensive. The limited number of models that could be fabricated also limited the range of design variations that could be evaluated. It can be anticipated that in the future, the role of wind tunnel testing in the design process will be more one of verification. Experimental research to improve our understanding of the physics of complex flows will continue, however, to play a vital role.

### 3. CFD algorithms

#### 3.1. Difficulties of flow simulation

The computational simulation of fluid flow presents a number of severe challenges for algorithm design. At the level of inviscid modeling, the inherent nonlinearity of the fluid flow equations leads to the formation of singularities such as shock waves and contact discontinuities. Moreover, the geometric configurations of interest are extremely complex, and generally contain sharp edges which lead to the shedding of vortex sheets. Extreme gradients near stagnation points or wing tips may also lead to numerical errors that can have global influence. Numerically generated entropy may be convected from the leading edge for example, causing the formation of a numerically induced boundary layer which can lead to separation. The need to treat exterior domains of infinite extent is also a source of difficulty. Boundary conditions imposed at artificial outer boundaries may cause reflected

waves which significantly interfere with the flow. When viscous effects are also included in the simulation, the extreme difference of the scales in the viscous boundary layer and the outer flow, which is essentially inviscid, is another source of difficulty, forcing the use of meshes with extreme variations in mesh interval. For these reasons CFD, has been a driving force for the development of numerical algorithms.

#### 3.2. Structured and unstructured meshes

The algorithm designer faces a number of critical decisions. The first choice that must be made is the nature of the mesh used to divide the flow field into discrete subdomains. The discretization procedure must allow for the treatment of complex configurations. The principal alternatives are Cartesian meshes, body-fitted curvilinear meshes, and unstructured tetrahedral meshes. Each of these approaches has advantages which have led to their use. The Cartesian mesh minimizes the complexity of the algorithm at interior points and facilitates the use of high order discretization procedures, at the expense of greater complexity, and possibly a loss of accuracy, in the treatment of boundary conditions at curved surfaces. This difficulty may be alleviated by using mesh refinement procedures near the surface. With their aid, schemes which use Cartesian meshes have recently been developed to treat very complex configurations [44–47].

Body-fitted meshes have been widely used and are particularly well suited to the treatment of viscous flow because they readily allow the mesh to be compressed near the body surface. With this approach, the problem of mesh generation itself has proved to be a major pacing item. The most commonly used procedures are algebraic transformations [48–51], methods based on the solution of elliptic equations, pioneered by Thompson [52–55], and methods based on the solution of hyperbolic equations marching out from the body [56]. In order to treat very complex configurations it generally proves expedient to use a multiblock [57,58] procedure, with separately generated meshes in each block, which may then be patched at block faces, or allowed to overlap, as in the Chimera scheme [59,60]. While a number of interactive software systems for grid generation have been developed, such as EAGLE, GRIDGEN, and ICEM, the generation of a satisfactory grid for a very complex configuration may require months of effort.

The alternative is to use an unstructured mesh in which the domain is subdivided into tetrahedra. This in turn requires the development of solution algorithms capable of yielding the required accuracy on unstructured meshes. This approach has been gaining acceptance, as it is becoming apparent that it can lead to a speed-up and reduction in the cost of mesh generation that more than offsets the increased complexity and cost of the flow simulations. Two competing procedures for

generating triangulations which have both proved successful are Delaunay triangulation [61,20], based on concepts introduced at the beginning of the century by Voronoi [62], and the moving front method [63].

### 3.3. Finite difference, finite volume, and finite element schemes

Associated with choice of mesh type is the formulation of the discretization procedure for the equations of fluid flow, which can be expressed as differential conservation laws. In the Cartesian tensor notation, let  $x_i$  be the coordinates,  $p$ ,  $\rho$ ,  $T$ , and  $E$  the pressure, density, temperature, and total energy, and  $u_i$  the velocity components. Using the convention that summation over  $j = 1, 2, 3$  is implied by a repeated subscript  $j$ , each conservation equation has the form

$$\frac{\partial w}{\partial t} + \frac{\partial f_j}{\partial x_j} - \frac{\partial f_{vj}}{\partial x_j} = 0, \quad (1)$$

where  $f_j$  are the inviscid (convective) fluxes, and  $f_{vj}$  are the viscous fluxes. For the mass equation

$$w = \rho, \quad f_j = \rho u_j.$$

For the  $i$  momentum equation

$$w_i = \rho u_i, \quad f_{ij} = \rho u_i u_j + p \delta_{ij}, \quad f_{vij} = \sigma_{ij},$$

where  $\sigma_{ij}$  is the viscous stress tensor. For the energy equation

$$w = \rho E, \quad f_j = p H u_j, \quad f_{vj} = \sigma_{jk} u_k - k \frac{\partial T}{\partial x_j},$$

where  $k$  is the coefficient of thermal conductivity. The pressure is related to the density and energy by the equation of state

$$p = (\gamma - 1)\rho(E - \frac{1}{2}u_i u_i) \quad (2)$$

in which  $\gamma$  is the ratio of specific heats and the stagnation enthalpy is given by

$$H = E + \frac{p}{\rho}$$

while

$$E = c_v T + \frac{1}{2}u_i u_i,$$

where  $c_v$  is the specific heat at constant volume. In the Navier–Stokes equations the viscous stresses are assumed to be linearly proportional to the rate of strain, or

$$\sigma_{ij} = \mu \left( \frac{\partial u_i}{\partial x_j} + \frac{\partial u_j}{\partial x_i} \right) + \lambda \delta_{ij} \left( \frac{\partial u_k}{\partial x_k} \right), \quad (3)$$

where  $\mu$  and  $\lambda$  are the coefficients of viscosity and bulk viscosity, and usually  $\lambda = -2\mu/3$ . The coefficient of

thermal conductivity and temperature are given by the relations

$$k = \frac{c_p \mu}{\text{Pr}}, \quad T = \frac{p}{R\rho},$$

where  $c_p$  is the specific heat at constant pressure,  $R$  is the gas constant, and  $\text{Pr}$  is the Prandtl number.

The finite difference method, which requires the use of a Cartesian or a structured curvilinear mesh, directly approximates the differential operators appearing in these equations. In the finite volume method [64], the discretization is accomplished by dividing the domain of the flow into a large number of small subdomains, and applying the conservation laws in the integral form

$$\frac{\partial}{\partial t} \int_{\Omega} w \, dV + \int_{\partial\Omega} \mathbf{f} \cdot d\mathbf{S} = 0.$$

Here  $\mathbf{f}$  is the flux appearing in Eq. (1) and  $d\mathbf{S}$  is the directed surface element of the boundary  $\partial\Omega$  of the domain  $\Omega$ . The use of the integral form has the advantage that no assumption of the differentiability of the solutions is implied, with the result that it remains a valid statement for a subdomain containing a shock wave. In general, the subdomains could be arbitrary, but it is convenient to use either hexahedral cells in a body conforming curvilinear mesh or tetrahedrons in an unstructured mesh.

Alternative discretization schemes may be obtained by storing flow variables at either the cell centers or the vertices. These variations are illustrated in Fig. 3 for the two-dimensional case. With a cell-centered scheme the discrete conservation law takes the form

$$\frac{d}{dt} wV + \sum_{\text{faces}} \mathbf{f} \cdot \mathbf{S} = 0, \quad (4)$$

where  $V$  is the cell volume, and  $\mathbf{f}$  is now a numerical estimate of the flux vector through each face.  $\mathbf{f}$  may be evaluated from values of the flow variables in the cells separated by each face, using upwind biasing to allow for the directions of wave propagation. With hexahedral cells, Eq. (4) is very similar to a finite difference scheme in curvilinear coordinates. Under a transformation to curvilinear coordinates  $\xi_j$ , Eq. (1) becomes

$$\frac{\partial}{\partial t} (Jw) + \frac{\partial}{\partial \xi_i} \left( J \frac{\partial \xi_i}{\partial x_j} f_j \right) = 0, \quad (5)$$

where  $J$  is the Jacobian determinant of the transformation matrix  $[\partial x_i / \partial \xi_j]$ . The transformed flux  $J(\partial \xi_i / \partial x_j) f_j$  corresponds to the dot product of the flux  $\mathbf{f}$  with a vector face area  $J \partial \xi_i / \partial x_j$ , while  $J$  represents the transformation of the cell volume. The finite volume form (4) has the advantages that it is valid for both structured and unstructured meshes, and that it assures that a uniform flow exactly satisfies the equations, because  $\sum_{\text{faces}} \mathbf{S} = 0$  for

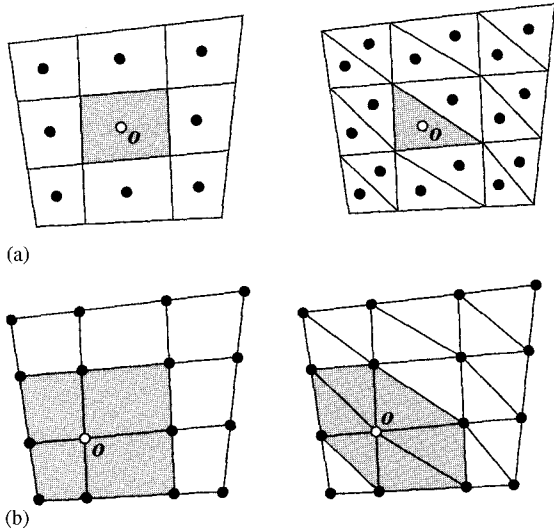


Fig. 3. Structured and unstructured discretizations. a: Cell-centered scheme, and b: Vertex Scheme.

a closed control volume. Finite difference schemes do not necessarily satisfy this constraint because of the discretization errors in evaluating  $\partial \xi_i / \partial x_j$  and the inversion of the transformation matrix. A cell-vertex finite volume scheme can be derived by taking the union of the cells surrounding a given vertex as the control volume for that vertex [65–67]. In Eq. (4),  $V$  is now the sum of the volumes of the surrounding cells, while the flux balance is evaluated over the outer faces of the polyhedral control volume. In the absence of upwind biasing the flux vector is evaluated by averaging over the corners of each face. This has the advantage of remaining accurate on an irregular or unstructured mesh.

An alternative route to the discrete equations is provided by the finite element method. Whereas the finite difference and finite volume methods approximate the differential and integral operators, the finite element method proceeds by inserting an approximate solution into the exact equations. On multiplying by a test function  $\phi$  and integrating by parts over space, one obtains the weak form

$$\frac{\partial}{\partial t} \iiint_{\Omega} \phi w \, d\Omega = \iiint_{\Omega} \mathbf{f} \cdot \nabla \phi \, d\Omega - \iint_{\partial\Omega} \phi \mathbf{f} \cdot \mathbf{dS} \quad (6)$$

which is also valid in the presence of discontinuities in the flow. In the Galerkin method the approximate solution is expanded in terms of the same family of functions as those from which the test functions are drawn. By choosing test functions with local support, separate equations are obtained for each node. For example, if a tetrahedral mesh is used, and  $\phi$  is piecewise linear, with a nonzero

value only at a single node, the equations at each node have a stencil which contains only the nearest neighbors. In this case the finite element approximation corresponds closely to a finite volume scheme. If a piecewise linear approximation to the flux  $\mathbf{f}$  is used in the evaluation of the integrals on the right hand side of Eq. (6), these integrals reduce to formulas which are identical to the flux balance of the finite volume scheme.

Thus, the finite difference and finite volume methods lead to essentially similar schemes on structured meshes, while the finite volume method is essentially equivalent to a finite element method with linear elements when a tetrahedral mesh is used. Provided that the flow equations are expressed in the conservation law form (1), all three methods lead to an exact cancellation of the fluxes through interior cell boundaries, so that the conservative property of the equations is preserved. The important role of this property in ensuring correct shock jump conditions was pointed out by Lax and Wendroff [68].

### 3.4. Nonoscillatory shock capturing schemes

#### 3.4.1. Local extremum diminishing (LED) schemes

The discretization procedures which have been described in the last section lead to nondissipative approximations to the Euler equations. Dissipative terms may be needed for two reasons. The first is the possibility of undamped oscillatory modes. The second reason is the need for the clean capture of shock waves and contact discontinuities without undesirable oscillations. An extreme overshoot could result in a negative value of an inherently positive quantity such as the pressure or density. The next sections summarize a unified approach to the construction of nonoscillatory schemes via the introduction of controlled diffusive and antidiffusive terms. This is the line adhered to in the author's own work.

The development of nonoscillatory schemes has been a prime focus of algorithm research for compressible flow. Consider a general semi-discrete scheme of the form

$$\frac{d}{dt} v_j = \sum_{k \neq j} c_{jk} (v_k - v_j). \quad (7)$$

A maximum cannot increase and a minimum cannot decrease if the coefficients  $c_{jk}$  are nonnegative, since at a maximum  $v_k - v_j \leq 0$ , and at a minimum  $v_k - v_j \geq 0$ . Thus the condition

$$c_{jk} \geq 0, \quad k \neq j \quad (8)$$

is sufficient to ensure stability in the maximum norm. Moreover, if the scheme has a compact stencil, so that  $c_{jk} = 0$  when  $j$  and  $k$  are not nearest neighbors, a local maximum cannot increase and local minimum cannot decrease. This local extremum diminishing (LED) property prevents the birth and growth of oscillations. The

one-dimensional conservation law

$$\frac{\partial u}{\partial t} + \frac{\partial}{\partial x} f(u) = 0$$

provides a useful model for analysis. In this case waves are propagated with a speed  $a(u) = \partial f / \partial u$ , and the solution is constant along the characteristics  $dx/dt = a(u)$ . Thus the LED property is satisfied. In fact, the total variation

$$TV(u) = \int_{-\infty}^{\infty} \left| \frac{\partial u}{\partial x} \right| dx$$

of a solution of this equation does not increase, provided that any discontinuity appearing in the solution satisfies an entropy condition [69]. Harten proposed that difference schemes ought to be designed so that the discrete total variation cannot increase [70]. If the end values are fixed, the total variation can be expressed as

$$TV(u) = 2(\sum \text{maxima} - \sum \text{minima}).$$

Thus a LED scheme is also total variation diminishing (TVD). The converse is not necessarily true, since it is possible for adjacent maxima and minima to be shifted an equal amount, say upwards, so that the total variation is unchanged, while the local maximum is increased. Positivity conditions of the type expressed in Eqs. (7) and (8) lead to diagonally dominant schemes, and are the key to the elimination of improper oscillations. The positivity conditions may be realized by the introduction of diffusive terms or by the use of upwind biasing in the discrete scheme. Unfortunately, they may also lead to severe restrictions on accuracy unless the coefficients have a complex nonlinear dependence on the solution.

#### 3.4.2. Artificial diffusion and upwinding

Following the pioneering work of Godunov [71], a variety of dissipative and upwind schemes designed to have good shock capturing properties have been developed during the past two decades [72–86,20,70]. If the one-dimensional scalar conservation law

$$\frac{\partial v}{\partial t} + \frac{\partial}{\partial x} f(v) = 0 \quad (9)$$

is represented by a three point semi-discrete scheme

$$\frac{dv_j}{dt} = c_{j+1/2}^+(v_{j+1} - v_j) + c_{j-1/2}^-(v_{j-1} - v_j),$$

the scheme is LED if

$$c_{j+1/2}^+ \geq 0, \quad c_{j-1/2}^- \geq 0. \quad (10)$$

A conservative semi-discrete approximation to the one-dimensional conservation law can be derived by subdividing the line into cells. Then the evolution of the

value  $v_j$  in the  $j$ th cell is given by

$$\Delta x \frac{dv_j}{dt} + h_{j+1/2} - h_{j-1/2} = 0, \quad (11)$$

where  $h_{j+1/2}$  is an estimate of the flux between cells  $j$  and  $j+1$ . The simplest estimate is the arithmetic average  $(f_{j+1} + f_j)/2$ , but this leads to a scheme that does not satisfy the positivity conditions. To correct this, one may add a dissipative term and set

$$h_{j+1/2} = \frac{1}{2}(f_{j+1} + f_j) - \alpha_{j+1/2}(v_{j+1} - v_j). \quad (12)$$

In order to estimate the required value of the coefficient  $\alpha_{j+1/2}$ , let  $a_{j+1/2}$  be a numerical estimate of the wave speed  $\partial f / \partial v$ ,

$$a_{j+1/2} = \begin{cases} \frac{f_{j+1} - f_j}{v_{j+1} - v_j} & \text{if } v_{j+1} \neq v_j, \\ \left. \frac{\partial f}{\partial v} \right|_{v=v_j} & \text{if } v_{j+1} = v_j. \end{cases} \quad (13)$$

Then

$$h_{j+1/2} - h_{j-1/2} = -(\alpha_{j+1/2} - \frac{1}{2}a_{j+1/2})\Delta v_{j+1/2} + (\alpha_{j-1/2} + \frac{1}{2}a_{j-1/2})\Delta v_{j-1/2},$$

where

$$\Delta v_{j+1/2} = v_{j+1} - v_j,$$

and the LED condition (10) is satisfied if

$$\alpha_{j+1/2} \geq \frac{1}{2}|a_{j+1/2}|. \quad (14)$$

If one takes

$$\alpha_{j+1/2} = \frac{1}{2}|a_{j+1/2}|,$$

one obtains the first order upwind scheme

$$h_{j+1/2} = \begin{cases} f_j & \text{if } a_{j+1/2} > 0, \\ f_{j+1} & \text{if } a_{j+1/2} < 0. \end{cases}$$

This is the least diffusive first order scheme which satisfies the LED condition. In this sense upwinding is a natural approach to the construction of nonoscillatory schemes. It may be noted that the successful treatment of transonic potential flow also involved the use of upwind biasing. This was first introduced by Murman and Cole to treat the transonic small disturbance equation [4].

Another important requirement of discrete schemes is that they should exclude nonphysical solutions which do not satisfy appropriate entropy conditions [87], which require the convergence of characteristics towards admissible discontinuities. This places more stringent bounds on the minimum level of numerical viscosity [88–91]. In the case that the numerical flux function is strictly convex, Aiso has recently proved [92] that it is sufficient that

$$\alpha_{j+1/2} > \max\{\frac{1}{2}|a_{j+1/2}|, \varepsilon \text{sign}(v_{j+1} - v_j)\}$$



for  $\varepsilon > 0$ . Thus the numerical viscosity should be rounded out and not allowed to reach zero at a point where the wave speed  $a(u) = \partial f / \partial u$  approaches zero. This justifies, for example, Harten's entropy fix [70].

Higher order schemes can be constructed by introducing higher order diffusive terms. Unfortunately, these have larger stencils and coefficients of varying sign which are not compatible with conditions (8) for a LED scheme, and it is known that schemes which satisfy these conditions are at best first order accurate in the neighborhood of an extremum. It proves useful in the following development to introduce the concept of essentially local extremum diminishing (ELED) schemes. These are defined to be schemes which satisfy the condition that in the limit as the mesh width  $\Delta x \rightarrow 0$ , local maxima are nonincreasing, and local minima are nondecreasing.

### 3.4.3. High resolution switched schemes:

#### Jameson–Schmidt–Turkel (JST) scheme

Higher order nonoscillatory schemes can be derived by introducing anti-diffusive terms in a controlled manner. An early attempt to produce a high resolution scheme by this approach is the Jameson–Schmidt–Turkel (JST) scheme [93]. Suppose that anti-diffusive terms are introduced by subtracting neighboring differences to produce a third order diffusive flux

$$d_{j+1/2} = \alpha_{j+1/2} \{ \Delta v_{j+1/2} - \frac{1}{2} (\Delta v_{j+3/2} + \Delta v_{j-1/2}) \}, \quad (15)$$

which is an approximation to  $\frac{1}{2} \alpha \Delta x^3 \partial^3 v / \partial x^3$ . The positivity condition (8) is violated by this scheme. It proves that it generates substantial oscillations in the vicinity of shock waves, which can be eliminated by switching locally to the first order scheme. The JST scheme therefore introduces blended diffusion of the form

$$d_{j+1/2} = \varepsilon_{j+1/2}^{(2)} \Delta v_{j+1/2} - \varepsilon_{j+1/2}^{(4)} (\Delta v_{j+3/2} - 2\Delta v_{j+1/2} + \Delta v_{j-1/2}). \quad (16)$$

The idea is to use variable coefficients  $\varepsilon_{j+1/2}^{(2)}$  and  $\varepsilon_{j+1/2}^{(4)}$  which produce a low level of diffusion in regions where the solution is smooth, but prevent oscillations near discontinuities. If  $\varepsilon_{j+1/2}^{(2)}$  is constructed so that it is of order  $\Delta x^2$  where the solution is smooth, while  $\varepsilon_{j+1/2}^{(4)}$  is of order unity, both terms in  $d_{j+1/2}$  will be of order  $\Delta x^3$ .

The JST scheme has proved very effective in practice in numerous calculations of complex steady flows, and conditions under which it could be a total variation diminishing (TVD) scheme have been examined by Swanson and Turkel [94]. An alternative statement of sufficient conditions on the coefficients  $\varepsilon_{j+1/2}^{(2)}$  and  $\varepsilon_{j+1/2}^{(4)}$  for the JST scheme to be LED is as follows:

**Theorem 1** (Positivity of the JST scheme). *Suppose that whenever either  $v_{j+1}$  or  $v_j$  is an extremum the coefficients*

*of the JST scheme satisfy*

$$\varepsilon_{j+1/2}^{(2)} \geq \frac{1}{2} |\alpha_{j+1/2}|, \quad \varepsilon_{j+1/2}^{(4)} = 0. \quad (17)$$

*Then the JST scheme is local extremum diminishing (LED).*

**Proof.** We need only consider the rate of change of  $v$  at extremal points. Suppose that  $v_j$  is an extremum. Then

$$\varepsilon_{j+1/2}^{(4)} = \varepsilon_{j-1/2}^{(4)} = 0$$

and the semi-discrete scheme (11) reduces to

$$\Delta x \frac{dv_j}{dt} = (\varepsilon_{j+1/2}^{(2)} - \frac{1}{2} \alpha_{j+1/2}) \Delta v_{j+1/2} - (\varepsilon_{j-1/2}^{(2)} + \frac{1}{2} \alpha_{j-1/2}) \Delta v_{j-1/2}$$

and each coefficient has the required sign.  $\square$

In order to construct  $\varepsilon_{j+1/2}^{(2)}$  and  $\varepsilon_{j+1/2}^{(4)}$  with the desired properties define

$$R(u, v) = \begin{cases} \left| \frac{u - v}{|u| + |v|} \right|^q & \text{if } u \neq 0 \text{ or } v \neq 0, \\ 0 & \text{if } u = v = 0, \end{cases} \quad (18)$$

where  $q$  is a positive integer. Then  $R(u, v) = 1$  if  $u$  and  $v$  have opposite signs. Otherwise  $R(u, v) < 1$ . Now set

$$Q_j = R(\Delta v_{j+1/2}, \Delta v_{j-1/2}), \quad Q_{j+1/2} = \max(Q_j, Q_{j+1})$$

and

$$\varepsilon_{j+1/2}^{(2)} = \alpha_{j+1/2} Q_{j+1/2}, \quad \varepsilon_{j+1/2}^{(4)} = \frac{1}{2} \alpha_{j+1/2} (1 - Q_{j+1/2}). \quad (19)$$

### 3.4.4. Symmetric limited positive (SLIP) scheme

An alternative route to high resolution without oscillation is to introduce flux limiters to guarantee the satisfaction of the positivity condition (8). The use of limiters dates back to the work of Boris and Book [73]. A particularly simple way to introduce limiters, proposed by the author in 1984 [81], is to use flux limited dissipation. In this scheme the third order diffusion defined by Eq. (15) is modified by the insertion of limiters which produce an equivalent three point scheme with positive coefficients. The original scheme [81] can be improved in the following manner so that less restrictive flux limiters are required. Let  $L(u, v)$  be a limited average of  $u$  and  $v$  with the following properties:

- (P1)  $L(u, v) = L(v, u)$ ,
- (P2)  $L(\alpha u, \alpha v) = \alpha L(u, v)$ ,
- (P3)  $L(u, u) = u$ ,
- (P4)  $L(u, v) = 0$  if  $u$  and  $v$  have opposite signs; otherwise  $L(u, v)$  has the same sign as  $u$  and  $v$ .

Properties (P1)–(P3) are natural properties of an average. Property (P4) is needed for the construction of a LED or TVD scheme.

It is convenient to introduce the notation

$$\phi(r) = L(1, r) = L(r, 1),$$

where according to (P4)  $\phi(r) \geq 0$ . It follows from (P2) on setting  $\alpha = 1/u$  or  $1/v$  that

$$L(u, v) = \phi\left(\frac{v}{u}\right)u = \phi\left(\frac{u}{v}\right)v.$$

Also it follows on setting  $v = 1$  and  $u = r$  that

$$\phi(r) = r\phi\left(\frac{1}{r}\right).$$

Thus, if there exists  $r < 0$  for which  $\phi(r) > 0$ , then  $\phi(1/r) < 0$ . The only way to ensure that  $\phi(r) \geq 0$  is to require  $\phi(r) = 0$  for all  $r < 0$ , corresponding to property (P4).

Now one defines the diffusive flux for a scalar conservation law as

$$d_{j+1/2} = \alpha_{j+1/2} \{ \Delta v_{j+1/2} - L(\Delta v_{j+3/2}, \Delta v_{j-1/2}) \}. \quad (20)$$

Set

$$r^+ = \frac{\Delta v_{j+3/2}}{\Delta v_{j-1/2}}, \quad r^- = \frac{\Delta v_{j-3/2}}{\Delta v_{j+1/2}}$$

and

$$L(\Delta v_{j+3/2}, \Delta v_{j-1/2}) = \phi(r^+) \Delta v_{j-1/2},$$

$$L(\Delta v_{j-3/2}, \Delta v_{j+1/2}) = \phi(r^-) \Delta v_{j+1/2}.$$

Then,

$$\begin{aligned} \Delta x \frac{dv_j}{dt} = & \{ \alpha_{j+1/2} - \frac{1}{2} a_{j+1/2} + \alpha_{j-1/2} \phi(r^-) \} \Delta v_{j+1/2} \\ & - \{ \alpha_{j-1/2} + \frac{1}{2} a_{j-1/2} + \alpha_{j+1/2} \phi(r^+) \} \Delta v_{j-1/2}. \end{aligned} \quad (21)$$

Thus the scheme satisfies the LED condition if  $\alpha_{j+1/2} \geq \frac{1}{2} |a_{j+1/2}|$  for all  $j$ , and  $\phi(r) \geq 0$ , which is assured by property (P4) on  $L$ . At the same time it follows from property (P3) that the first order diffusive flux is canceled when  $\Delta v$  is smoothly varying and of constant sign. Schemes constructed by this formulation will be referred to as symmetric limited positive (SLIP) schemes. This result may be summarized as

**Theorem 2** (Positivity of the SLIP scheme). *Suppose that the discrete conservation law (11) contains a limited diffusive flux as defined by Eq. (20). Then the positivity condition (14), together with properties (P1)–(P4) for limited averages, are sufficient to ensure satisfaction of the LED principle that a local maximum cannot increase and a local minimum cannot decrease.*

A variety of limiters which meet the requirements of properties (P1)–(P4). Define

$$S(u, v) = \frac{1}{2} \{ \text{sign}(u) + \text{sign}(v) \}$$

which vanishes if  $u$  and  $v$  have opposite signs.

Then two limiters which are appropriate are the following well-known schemes:

1. *Minmod*:

$$L(u, v) = S(u, v) \min(|u|, |v|).$$

2. *Van Leer*:

$$L(u, v) = S(u, v) \frac{2|u||v|}{|u| + |v|}.$$

In order to produce a family of limiters which contains these as special cases it is convenient to set

$$L(u, v) = \frac{1}{2} D(u, v) (u + v),$$

where  $D(u, v)$  is a factor which should deflate the arithmetic average, and become zero if  $u$  and  $v$  have opposite signs. Take

$$D(u, v) = 1 - R(u, v) = 1 - \left| \frac{u - v}{|u| + |v|} \right|^q, \quad (22)$$

where  $R(u, v)$  is the same function that was introduced in the JST scheme, and  $q$  is a positive integer. Then  $D(u, v) = 0$  if  $u$  and  $v$  have opposite signs. Also if  $q = 1$ ,  $L(u, v)$  reduces to minmod, while if  $q = 2$ ,  $L(u, v)$  is equivalent to Van Leer's limiter. By increasing  $q$  one can generate a sequence of limited averages which approach a limit defined by the arithmetic mean truncated to zero when  $u$  and  $v$  have opposite signs.

When the terms are regrouped, it can be seen that with this limiter the SLIP scheme is exactly equivalent to the JST scheme, with the switch is defined as

$$Q_{j+1/2} = R(\Delta v_{j+3/2}, \Delta v_{j+1/2}),$$

$$\varepsilon_{j+1/2}^{(2)} = \alpha_{j+1/2} Q_{j+1/2},$$

$$\varepsilon_{j+1/2}^{(4)} = \alpha_{j+1/2} (1 - Q_{j+1/2}).$$

This formulation thus unifies the JST and SLIP schemes. The SLIP construction, however, provides a convenient framework for the construction of LED schemes on unstructured meshes [95].

### 3.4.5. Essentially local extremum diminishing (ELED) scheme with soft limiter

The limiters defined by formula (22) have the disadvantage that they are active at a smooth extrema, reducing the local accuracy of the scheme to first order. In order to prevent this, the SLIP scheme can be relaxed to give an essentially local extremum diminishing (ELED) scheme which is second order accurate at smooth extrema by the introduction of a threshold in the limited average. Therefore, redefine  $D(u, v)$  as

$$D(u, v) = 1 - \left| \frac{u - v}{\max(|u| + |v|, \varepsilon \Delta x^r)} \right|^q, \quad (23)$$

where  $r = \frac{3}{2}$ ,  $q \geq 2$ . This reduces to the previous definition if  $|u| + |v| > \varepsilon \Delta x^r$ .

In any region where the solution is smooth,  $\Delta v_{j+3/2} - \Delta v_{j-1/2}$  is of order  $\Delta x^2$ . In fact if there is a smooth extremum in the neighborhood of  $v_j$  or  $v_{j+1}$ , a Taylor series expansion indicates that  $\Delta v_{j+3/2}$ ,  $\Delta v_{j+1/2}$  and  $\Delta v_{j-1/2}$  are each individually of order  $\Delta x^2$ , since  $dv/dx = 0$  at the extremum. It may be verified that second order accuracy is preserved at a smooth extremum if  $q \geq 2$ . On the other hand the limiter acts in the usual way if  $|\Delta v_{j+3/2}|$  or  $|\Delta v_{j-3/2}| > \varepsilon \Delta x^r$ , and it may also be verified that in the limit  $\Delta x \rightarrow 0$  local maxima are nonincreasing and local minima are nondecreasing [95]. Thus the scheme is essentially local extremum diminishing (ELED).

The effect of the “soft limiter” is not only to improve the accuracy: the introduction of a threshold below which extrema of small amplitude are accepted also usually results in a faster rate of convergence to a steady state, and decreases the likelihood of limit cycles in which the limiter interacts unfavorably with the corrections produced by the updating scheme. In a scheme recently proposed by Venkatakrishnan a threshold is introduced precisely for this purpose [96].

### 3.4.6. Upstream limited positive (USLIP) schemes

By adding the anti-diffusive correction purely from the upstream side one may derive a family of upstream limited positive (USLIP) schemes. Corresponding to the original SLIP scheme defined by Eq. (20), a USLIP scheme is obtained by setting

$$d_{j+1/2} = \alpha_{j+1/2} \{ \Delta v_{j+1/2} - L(\Delta v_{j+1/2}, \Delta v_{j-1/2}) \}$$

if  $a_{j+1/2} > 0$ , or

$$d_{j+1/2} = \alpha_{j+1/2} \{ \Delta v_{j+1/2} - L(\Delta v_{j+1/2}, \Delta v_{j+3/2}) \}$$

if  $a_{j+1/2} < 0$ . If  $\alpha_{j+1/2} = \frac{1}{2}|a_{j+1/2}|$  one recovers a standard high resolution upwind scheme in semi-discrete form. Consider the case that  $a_{j+1/2} > 0$  and  $a_{j-1/2} > 0$ . If one sets

$$r^+ = \frac{\Delta v_{j+1/2}}{\Delta v_{j-1/2}}, \quad r^- = \frac{\Delta v_{j-3/2}}{\Delta v_{j-1/2}},$$

the scheme reduces to

$$\Delta x \frac{dv_j}{dt} = -\frac{1}{2} \{ \phi(r^+) a_{j+1/2} + (2 - \phi(r^-)) a_{j-1/2} \} \Delta v_{j-1/2}.$$

To assure the correct sign to satisfy the LED criterion the flux limiter must now satisfy the additional constraint that  $\phi(r) \leq 2$ .

The USLIP formulation is essentially equivalent to standard upwind schemes [77,79]. Both the SLIP and USLIP constructions can be implemented on unstructured meshes [97,95]. The anti-diffusive terms are then calculated by taking the scalar product of the vectors

defining an edge with the gradient in the adjacent up-stream and downstream cells.

### 3.4.7. Systems of conservation laws: flux splitting and flux-difference splitting

Steger and Warming [72] first showed how to generalize the concept of upwinding to the system of conservation laws

$$\frac{\partial w}{\partial t} + \frac{\partial}{\partial x} f(w) = 0 \quad (24)$$

by the concept of flux splitting. Suppose that the flux is split as  $f = f^+ + f^-$  where  $\partial f^+ / \partial w$  and  $\partial f^- / \partial w$  have positive and negative eigenvalues. Then the first order upwind scheme is produced by taking the numerical flux to be

$$h_{j+1/2} = f_j^+ + f_{j+1}^-.$$

This can be expressed in viscosity form as

$$\begin{aligned} h_{j+1/2} &= \frac{1}{2}(f_{j+1}^+ + f_j^+) - \frac{1}{2}(f_{j+1}^+ - f_j^+) \\ &\quad + \frac{1}{2}(f_{j+1}^- + f_j^-) + \frac{1}{2}(f_{j+1}^- - f_j^-) \\ &= \frac{1}{2}(f_{j+1} + f_j) - d_{j+1/2}, \end{aligned}$$

where the diffusive flux is

$$d_{j+1/2} = \frac{1}{2} \Delta (f^+ - f^-)_{j+1/2}. \quad (25)$$

Roe derived the alternative formulation of flux difference splitting [76] by distributing the corrections due to the flux difference in each interval upwind and downwind to obtain

$$\Delta x \frac{dw_j}{dt} + (f_{j+1} - f_j)^- + (f_j - f_{j-1})^+ = 0,$$

where now the flux difference  $f_{j+1} - f_j$  is split. The corresponding diffusive flux is

$$d_{j+1/2} = \frac{1}{2} (\Delta f_{j+1/2}^+ - \Delta f_{j+1/2}^-).$$

Following Roe's derivation, let  $A_{j+1/2}$  be a mean value Jacobian matrix exactly satisfying the condition

$$f_{j+1} - f_j = A_{j+1/2} (w_{j+1} - w_j). \quad (26)$$

$A_{j+1/2}$  may be calculated by substituting the weighted averages

$$u = \frac{\sqrt{\rho_{j+1}} u_{j+1} + \sqrt{\rho_j} u_j}{\sqrt{\rho_{j+1}} + \sqrt{\rho_j}}, \quad H = \frac{\sqrt{\rho_{j+1}} H_{j+1} + \sqrt{\rho_j} H_j}{\sqrt{\rho_{j+1}} + \sqrt{\rho_j}} \quad (27)$$

into the standard formulas for the Jacobian matrix  $A = \partial f / \partial w$ . A splitting according to characteristic fields is now obtained by decomposing  $A_{j+1/2}$  as

$$A_{j+1/2} = T A T^{-1}, \quad (28)$$

where the columns of  $T$  are the eigenvectors of  $A_{j+1/2}$ , and  $A$  is a diagonal matrix of the eigenvalues. Now the corresponding diffusive flux is

$$\frac{1}{2}|A_{j+1/2}|(w_{j+1} - w_j),$$

where

$$|A_{j+1/2}| = T|A|T^{-1}$$

and  $|A|$  is the diagonal matrix containing the absolute values of the eigenvalues.

### 3.4.8. Alternative splittings

Characteristic splitting has the advantages that it introduces the minimum amount of diffusion to exclude the growth of local extrema of the characteristic variables, and that with the Roe linearization it allows a discrete shock structure with a single interior point. To reduce the computational complexity one may replace  $|A|$  by  $\alpha I$  where if  $\alpha$  is at least equal to the spectral radius  $\max|\lambda(A)|$ , then the positivity conditions will still be satisfied. Then the first order scheme simply has the scalar diffusive flux

$$d_{j+1/2} = \frac{1}{2}\alpha_{j+1/2}\Delta w_{j+1/2}. \quad (29)$$

The JST scheme with scalar diffusive flux captures shock waves with about 3 interior points, and it has been widely used for transonic flow calculations because it is both robust and computationally inexpensive.

An intermediate class of schemes can be formulated by defining the first order diffusive flux as a combination of differences of the state and flux vectors

$$d_{j+1/2} = \frac{1}{2}\alpha_{j+1/2}^* c(w_{j+1} - w_j) + \frac{1}{2}\beta_{j+1/2}(f_{j+1} - f_j), \quad (30)$$

where the factor  $c$  is included in the first term to make  $\alpha_{j+1/2}^*$  and  $\beta_{j+1/2}$  dimensionless. Schemes of this class are fully upwind in supersonic flow if one takes  $\alpha_{j+1/2}^* = 0$  and  $\beta_{j+1/2} = \text{sign}(M)$  when the absolute value of the Mach number  $M$  exceeds 1. The flux vector  $f$  can be decomposed as

$$f = uw + f_p, \quad (31)$$

where

$$f_p = \begin{pmatrix} 0 \\ p \\ up \end{pmatrix}. \quad (32)$$

Then

$$f_{j+1} - f_j = \bar{u}(w_{j+1} - w_j) + \bar{w}(u_{j+1} - u_j) + f_{p,j+1} - f_{p,j}, \quad (33)$$

where  $\bar{u}$  and  $\bar{w}$  are the arithmetic averages

$$\bar{u} = \frac{1}{2}(u_{j+1} + u_j), \quad \bar{w} = \frac{1}{2}(w_{j+1} + w_j).$$

Thus these schemes are closely related to schemes which introduce separate splittings of the convective and pressure terms, such as the wave-particle scheme [98,99], the advection upwind splitting method (AUSM) [100,101], and the convective upwind and split pressure (CUSP) schemes [97].

In order to examine the shock capturing properties of these various schemes, consider the general case of a first order diffusive flux of the form

$$d_{j+1/2} = \frac{1}{2}\alpha_{j+1/2}B_{j+1/2}(w_{j+1} - w_j), \quad (34)$$

where the matrix  $B_{j+1/2}$  determines the properties of the scheme and the scaling factor  $\alpha_{j+1/2}$  is included for convenience. All the previous schemes can be obtained by representing  $B_{j+1/2}$  as a polynomial in the matrix  $A_{j+1/2}$  defined by Eq. (26). Schemes of this class were considered by Van Leer [74]. According to the Cayley-Hamilton theorem, a matrix satisfies its own characteristic equation. Therefore, the third and higher powers of  $A$  can be eliminated, and there is no loss of generality in limiting  $B_{j+1/2}$  to a polynomial of degree 2,

$$B_{j+1/2} = \alpha_0 I + \alpha_1 A_{j+1/2} + \alpha_2 A_{j+1/2}^2. \quad (35)$$

The characteristic upwind scheme for which  $B_{j+1/2} = |A_{j+1/2}|$  is obtained by substituting  $A_{j+1/2} = TAT^{-1}$ ,  $A_{j+1/2}^2 = TA^2T^{-1}$ . Then  $\alpha_0$ ,  $\alpha_1$ , and  $\alpha_2$  are determined from the three equations

$$\alpha_0 + \alpha_1 \lambda_k + \alpha_2 \lambda_k^2 = |\lambda_k|, \quad k = 1, 2, 3.$$

The same representation remains valid for three dimensional flow because  $A_{j+1/2}$  still has only three distinct eigenvalues  $u$ ,  $u + c$ ,  $u - c$ .

### 3.4.9. Analysis of stationary discrete shocks

The ideal model of a discrete shock is illustrated in Fig. 4. Suppose that  $w_L$  and  $w_R$  are left and right states which satisfy the jump conditions for a stationary shock, and that the corresponding fluxes are  $f_L = f(w_L)$  and  $f_R = f(w_R)$ . Since the shock is stationary  $f_L = f_R$ . The ideal discrete shock has constant states  $w_L$  to the left and  $w_R$  to the right, and a single point with an intermediate value  $w_A$ . The intermediate value is needed to allow the discrete solution to correspond to a true solution in which the shock wave does not coincide with an interface between two mesh cells.

Schemes corresponding to one, two or three terms in Eq. (35) are examined in [102]. The analysis of these three cases shows that a discrete shock structure with a single interior point is supported by artificial diffusion that satisfies the two conditions that

1. it produces an upwind flux if the flow is determined to be supersonic through the interface,
2. it satisfies a generalized eigenvalue problem for the exit from the shock of the form

$$(A_{AR} - \alpha_{AR}B_{AR})(w_R - w_A) = 0, \quad (36)$$

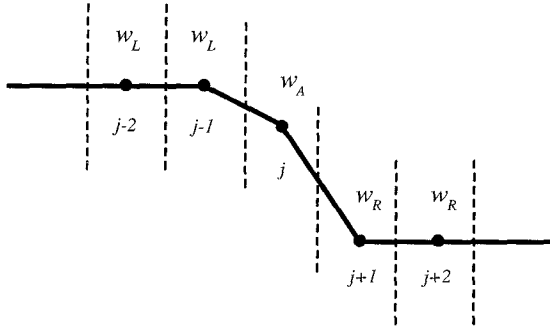


Fig. 4. Shock structure for single interior point.

where  $A_{AR}$  is the linearized Jacobian matrix and  $B_{AR}$  is the matrix defining the diffusion for the interface  $AR$ . This follows from the equilibrium condition  $h_{RA} = h_{RR}$  for the cell  $j+1$  in Fig. 4. These two conditions are satisfied by both the characteristic scheme and also the CUSP scheme, provided that the coefficients of convective diffusion and pressure differences are correctly balanced. Scalar diffusion does not satisfy the first condition. In the case of the CUSP scheme (30) Eq. (36) reduces to

$$\left( A_{RA} + \frac{\alpha^* c}{1 + \beta} \right) (w_R - w_A) = 0.$$

Thus  $w_R - w_A$  is an eigenvector of the Roe matrix  $A_{RA}$ , and  $-\alpha^* c / (1 + \beta)$  is the corresponding eigenvalue. Since the eigenvalues are  $u$ ,  $u + c$ , and  $u - c$ , the only choice which leads to positive diffusion when  $u > 0$  is  $u - c$ , yielding the relationship

$$\alpha^* c = (1 + \beta)(c - u), \quad 0 < u < c.$$

This leads to a one parameter family of schemes which support the ideal shock structure. The term  $\beta(f_R - f_A)$  contributes to the diffusion of the convective terms. Allowing for split (31), the total effective coefficient of convective diffusion is  $\alpha c = \alpha^* c + \beta \bar{u}$ . A CUSP scheme with low numerical diffusion is then obtained by taking  $\alpha = |M|$ , leading to the coefficients illustrated in Fig. 5.

#### 3.4.10. CUSP and characteristic schemes admitting constant total enthalpy in steady flow

In steady flow the stagnation enthalpy  $H$  is constant, corresponding to the fact that the energy and mass conservation equations are consistent when the constant factor  $H$  is removed from the energy equation. Discrete and semi-discrete schemes do not necessarily satisfy this property. In the case of a semi-discrete scheme expressed in viscosity form, Eqs. (11) and (12), a solution with constant  $H$  is admitted if the viscosity for the energy equation reduces to the viscosity for the continuity equation with  $\rho$  replaced by  $\rho H$ . When the standard characteristic decomposition (28) is used, the viscous fluxes for

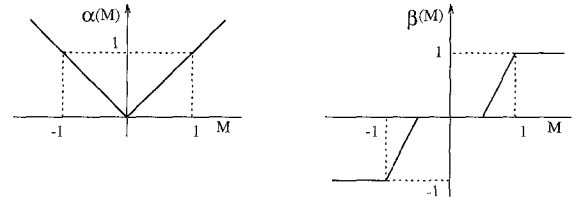


Fig. 5. Diffusion coefficients.

$\rho$  and  $\rho H$  which result from composition of the fluxes for the characteristic variables do not have this property, and  $H$  is not constant in the discrete solution. In practice, there is an excursion of  $H$  in the discrete shock structure which represents a local heat source. In very high speed flows the corresponding error in the temperature may lead to a wrong prediction of associated effects such as chemical reactions.

The source of the error in the stagnation enthalpy is the discrepancy between the convective terms

$$u \begin{pmatrix} \rho \\ \rho u \\ \rho H \end{pmatrix}$$

in the flux vector, which contain  $\rho H$ , and the state vector which contains  $\rho E$ . This may be remedied by introducing a modified state vector

$$w_h = \begin{pmatrix} \rho \\ \rho u \\ \rho H \end{pmatrix}.$$

Then one introduces the linearization

$$f_R - f_L = A_h (w_{hr} - w_{hl}).$$

Here  $A_h$  may be calculated in the same way as the standard Roe linearization. Introduce the weighted averages defined by Eq. (27). Then

$$A_h = \begin{pmatrix} 0 & 1 & 0 \\ -\frac{\gamma+1}{\gamma} \frac{u^2}{2} & \frac{\gamma+1}{\gamma} u & \frac{\gamma-1}{\gamma} \\ -uH & H & u \end{pmatrix}.$$

The eigenvalues of  $A_h$  are  $u$ ,  $\lambda^+$  and  $\lambda^-$  where

$$\lambda^\pm = \frac{\gamma+1}{2\gamma} u \pm \sqrt{\left( \frac{\gamma+1}{2\gamma} u \right)^2 + \frac{c^2 - u^2}{\gamma}}. \quad (37)$$

Now both CUSP and characteristic schemes which preserve constant stagnation enthalpy in steady flow can be constructed from the modified Jacobian matrix  $A_h$  [102]. These schemes also produce a discrete shock structure with one interior point in steady flow. Then one arrives at

four variations with this property, which can conveniently be distinguished as the E- and H-CUSP schemes, and the E- and H-characteristic schemes.

### 3.4.11. High order Godunov schemes, and kinetic flux splitting

Some of the most impressive simulations of time dependent flows with strong shock waves have been achieved with higher order Godunov schemes [84]. In these schemes the average value in each cell is updated by applying the integral conservation law using interface fluxes predicted from the exact or approximate solution of a Riemann problem between adjacent cells. A higher order estimate of the solution is then reconstructed from the cell averages, and slope limiters are applied to the reconstruction. An example is the class of essentially nonoscillatory (ENO) schemes, which can attain a very high order of accuracy at the cost of a substantial increase in computational complexity [103–106]. Methods based on reconstruction can also be implemented on unstructured meshes [85,86]. Recently, there has been an increasing interest in kinetic flux splitting schemes, which use solutions of the Boltzmann equation or the BGK equation to predict the interface fluxes [107–111].

### 3.5. Multidimensional schemes

The simplest approach to the treatment of multidimensional problems on structured meshes is to apply the one-dimensional construction separately in each mesh direction. On triangulated meshes in two or three dimensions the SLIP and USLIP constructions may also be implemented along the mesh edges [95]. A substantial body of current research is directed toward the implementation of truly multidimensional upwind schemes in which the upwind biasing is determined by properties of the flow rather than the mesh [112–116]. A thorough review is given by Pailliere and DeConinck [117].

Residual distribution schemes are an attractive approach for triangulated meshes. In these the residual defined by the space derivatives is evaluated for each cell, and then distributed to the vertices with weights which depend on the direction of convection. For a scalar conservation law the weights can be chosen to maintain positivity with minimum cross diffusion in the direction normal to the flow. For the Euler equations the residual can be linearized by assuming that the parameter vector with components  $\sqrt{\rho}$ ,  $\sqrt{\rho}u_i$ , and  $\sqrt{\rho}H$  varies linearly over the cell. Then

$$\frac{\partial f_j(w)}{\partial x_j} = A_j \frac{\partial w}{\partial x_j},$$

where the Jacobian matrices  $A_j = \partial f_j / \partial w$  are evaluated with Roe averaging of the values of  $w$  at the vertices. Waves in the direction  $\mathbf{n}$  can then be expressed in terms of

the eigenvectors of  $n_j A_j$ , and a positive distribution scheme is used for waves in preferred directions. The best choice of these directions is the subject of ongoing research, but preliminary results indicate the possibility of achieving high resolution of shocks and contact discontinuities which are not aligned with mesh lines [117].

Hirsch and Van Ransbeeck adopt an alternative approach in which they directly construct directional diffusive terms on structured meshes, with anti-diffusion controlled by limiters based on comparisons of slopes in different directions [118]. They also show promising results in calculations of nozzles with multiply reflected oblique shocks.

### 3.6. Discretization of the viscous terms

The discretization of the viscous terms of the Navier–Stokes equations requires an approximation to the velocity derivatives  $\partial u_i / \partial x_j$  in order to calculate the tensor  $\sigma_{ij}$ , Eq. (3). Then the viscous terms may be included in the flux balance (4). In order to evaluate the derivatives one may apply the Gauss formula to a control volume  $V$  with the boundary  $S$ ,

$$\int_V \frac{\partial u_i}{\partial x_j} dv = \int_S u_i n_j ds,$$

where  $n_j$  is the outward normal. For a tetrahedral or hexahedral cell this gives

$$\frac{\partial u_i}{\partial x_j} = \frac{1}{\text{vol}} \sum_{\text{faces}} \bar{u}_i n_j s, \quad (38)$$

where  $\bar{u}_i$  is an estimate of the average of  $u_i$  over the face. If  $u$  varies linearly over a tetrahedral cell this is exact. Alternatively, assuming a local transformation to computational coordinates  $\xi_j$ , one may apply the chain rule

$$\frac{\partial u}{\partial x} = \left[ \frac{\partial u}{\partial \xi} \right] \left[ \frac{\partial \xi}{\partial x} \right] = \frac{\partial u}{\partial \xi} \left[ \frac{\partial x}{\partial \xi} \right]^{-1}. \quad (39)$$

Here the transformation derivatives  $\partial x_i / \partial \xi_j$  can be evaluated by the same finite difference formulas as the velocity derivatives  $\partial u_i / \partial \xi_j$ . In this case  $\partial u / \partial \xi$  is exact if  $u$  is a linearly varying function.

For a cell-centered discretization (Fig. 6a)  $\partial u / \partial \xi$  is needed at each face. The simplest procedure is to evaluate  $\partial u / \partial \xi$  in each cell, and to average  $\partial u / \partial \xi$  between the two cells on either side of a face [119]. The resulting discretization does not have a compact stencil, and supports undamped oscillatory modes. In a one-dimensional calculation, for example,  $\partial^2 u / \partial x^2$  would be discretized as  $(u_{i+2} - 2u_i + u_{i-2}) / 4\Delta x^2$ . In order to produce a compact stencil  $\partial u / \partial x$  may be estimated from a control volume centered on each face, using formulas (38) or (39) [120]. This is computationally expensive because the number of faces is much larger than the number of cells. In a

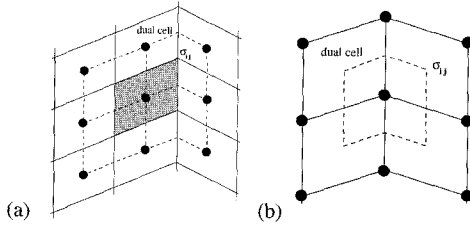


Fig. 6. Viscous discretizations for cell-centered and cell-vertex algorithms. a: Cell-centered scheme.  $\sigma_{ij}$  evaluated at vertices of the primary mesh and b: Cell-vertex scheme.  $\sigma_{ij}$  evaluated at cell centers of the primary mesh.

hexahedral mesh with a large number of vertices the number of faces approaches three times the number of cells.

This motivates the introduction of dual meshes for the evaluation of the velocity derivatives and the flux balance as sketched in Fig. 6. The figure shows both cell-centered and cell-vertex schemes. The dual mesh connects cell centers of the primary mesh. If there is a kink in the primary mesh, the dual cells should be formed by assembling contiguous fractions of the neighboring primary cells. On smooth meshes comparable results are obtained by either of these formulations [21,28,121]. If the mesh has a kink the cell-vertex scheme has the advantage that the derivatives  $\partial u_i / \partial x_j$  are calculated in the interior of a regular cell, with no loss of accuracy.

A desirable property is that a linearly varying velocity distribution, as in a Couette flow, should produce a constant stress and hence an exact stress balance. This property is not necessarily satisfied in general by finite difference or finite volume schemes on curvilinear meshes. The characterization  $k$ -exact has been proposed for schemes that are exact for polynomials of degree  $k$ . The cell-vertex finite volume scheme is linearly exact if the derivatives are evaluated by Eq. (39), since then  $\partial u_i / \partial x_j$  is exactly evaluated as a constant, leading to constant viscous stresses  $\sigma_{ij}$ , and an exact viscous stress balance. This remains true when there is a kink in the mesh, because the summation of constant stresses over the faces of the kinked control volume sketched in Fig. 6 still yields a perfect balance. The use of Eq. (39) to evaluate  $\partial u_i / \partial x_j$ , however, requires the additional calculation or storage of the nine metric quantities  $\partial u_i / \partial x_j$  in each cell, whereas Eq. (38) can be evaluated from the same face areas that are used for the flux balance.

In the case of an unstructured mesh, the weak form (6) leads to a natural discretization with linear elements, in which the piecewise linear approximation yields a constant stress in each cell. This method yields a representation which is globally correct when averaged over the cells, as is proved by energy estimates for elliptic problems [10]. It should be noted, however, that it yields

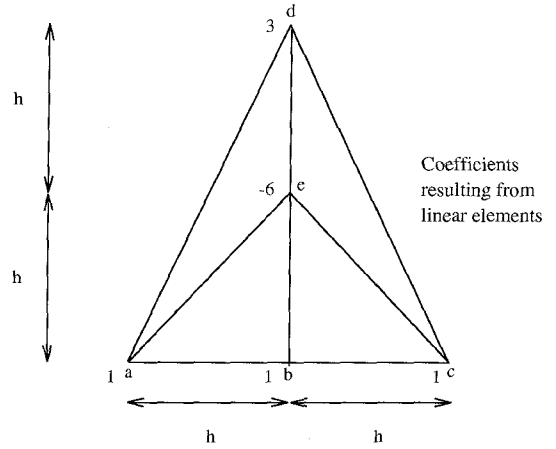


Fig. 7. Example of discretization  $u_{xx} + u_{yy}$  on a triangular mesh. The discretization is locally equivalent to the approximation  $u_{xx} = (u_a - 2u_b + u_c)/h^2$ ,  $3u_{yy} = (3u_d - 6u_e + 3u_b)/h^2$ .

formulas that are not necessarily locally consistent with the differential equations, if Taylor series expansions are substituted for the solution at the vertices appearing in the local stencil. Fig. 7 illustrates the discretization of the Laplacian  $u_{xx} + u_{yy}$  which is obtained with linear elements. It shows a particular triangulation such that the approximation is locally consistent with  $u_{xx} + 3u_{yy}$ . Thus the use of an irregular triangulation in the boundary layer may significantly degrade the accuracy.

Anisotropic grids are needed in order to resolve the thin boundary layers which appear in viscous flows at high Reynolds numbers. Otherwise an excessively large number of grid cells may be required. The use of flat tetrahedra can have an adverse effect on both the accuracy of the solution and the rate of convergence to a steady state. This has motivated the use of hybrid prismatic-tetrahedral grids in which prismatic cells are used in the wall regions [122]. A review of many of the key issues in the design of flow solvers for unstructured meshes is given by Venkatakrishnan [123].

### 3.7. Time-stepping schemes

If the space discretization procedure is implemented separately, it leads to a set of coupled ordinary differential equations, which can be written in the form

$$\frac{d\mathbf{w}}{dt} + \mathbf{R}(\mathbf{w}) = \mathbf{0}, \quad (40)$$

where  $\mathbf{w}$  is the vector of the flow variables at the mesh points, and  $\mathbf{R}(\mathbf{w})$  is the vector of the residuals, consisting of the flux balances defined by the space discretization scheme, together with the added dissipative terms. If the objective is simply to reach the steady state and details of

the transient solution are immaterial, the time-stepping scheme may be designed solely to maximize the rate of convergence. The first decision that must be made is whether to use an explicit scheme, in which the space derivatives are calculated from known values of the flow variables at the beginning of the time step, or an implicit scheme, in which the formulas for the space derivatives include as yet unknown values of the flow variables at the end of the time step, leading to the need to solve coupled equations for the new values. The permissible time step for an explicit scheme is limited by the Courant–Friedrichs–Lewy (CFL) condition, which states that a difference scheme cannot be a convergent and stable approximation unless its domain of dependence contains the domain of dependence of the corresponding differential equation. One can anticipate that implicit schemes will yield convergence in a smaller number of time steps, because the time step is no longer constrained by the CFL condition. Implicit schemes will be efficient, however, only if the decrease in the number of time steps outweighs the increase in the computational effort per time step consequent upon the need to solve coupled equations. The prototype implicit scheme can be formulated by estimating  $\partial \mathbf{w} / \partial t$  at  $t + \mu \Delta t$  as a linear combination of  $\mathbf{R}(\mathbf{w}^n)$  and  $\mathbf{R}(\mathbf{w}^{n+1})$ . The resulting equation

$$\mathbf{w}^{n+1} = \mathbf{w}^n - \Delta t \{ (1 - \mu) \mathbf{R}(\mathbf{w}^n) + \mu \mathbf{R}(\mathbf{w}^{n+1}) \}$$

can be linearized as

$$\left( \mathbf{I} + \mu \Delta t \frac{\partial \mathbf{R}}{\partial \mathbf{w}} \right) \delta \mathbf{w} + \Delta t \mathbf{R}(\mathbf{w}^n) = 0.$$

If one sets  $\mu = 1$  and lets  $\Delta t \rightarrow \infty$  this reduces to the Newton iteration, which has been successfully used in two-dimensional calculations [124,125]. In the three-dimensional case with, say, an  $N \times N \times N$  mesh, the bandwidth of the matrix that must be inverted is of order  $N^2$ . Direct inversion requires a number of operations proportional to the number of unknowns multiplied by the square of the bandwidth, and hence of the order of  $N^7$ . This is prohibitive, and forces recourse to either an approximate factorization method or an iterative solution method.

Alternating direction methods, which introduce factors corresponding to each coordinate, are widely used for structured meshes [126,127]. They cannot be implemented on unstructured tetrahedral meshes that do not contain identifiable mesh directions, although other decompositions are possible [128,129]. If one chooses to adopt the iterative solution technique, the principal alternatives are variants of the Gauss–Seidel and Jacobi methods. A symmetric Gauss–Seidel method with one iteration per time step is essentially equivalent to an approximate lower-upper (LU) factorization of the implicit scheme [130–133]. On the other hand, the Jacobi

method with a fixed number of iterations per time step reduces to a multistage explicit scheme, belonging to the general class of Runge–Kutta schemes [134]. Schemes of this type have proved very effective for wide variety of problems, and they have the advantage that they can be applied equally easily on both structured and unstructured meshes [93,135–137].

If one reduces the linear model problem corresponding to (40) to an ordinary differential equation by substituting a Fourier mode  $\hat{w} = e^{ipx}$ , the resulting Fourier symbol has an imaginary part proportional to the wave speed, and a negative real part proportional to the diffusion. Thus, the time stepping scheme should have a stability region which contains a substantial interval of the negative real axis, as well as an interval along the imaginary axis. To achieve this it pays to treat the convective and dissipative terms in a distinct fashion. Thus the residual is split as

$$R(w) = Q(w) + D(w),$$

where  $Q(w)$  is the convective part and  $D(w)$  the dissipative part. Denote the time level  $n\Delta t$  by a superscript  $n$ . Then the multistage time stepping scheme is formulated as

$$w^{(n+1,0)} = w^n,$$

...

$$w^{(n+1,k)} = w^n - \alpha_k \Delta t (Q^{(k-1)} + D^{(k-1)}),$$

...

$$w^{n+1} = w^{(n+1,m)},$$

where the superscript  $k$  denotes the  $k$ -th stage,  $\alpha_m = 1$ , and

$$Q^{(0)} = Q(w^n), \quad D^{(0)} = D(w^n),$$

...

$$Q^{(k)} = Q(w^{(n+1,k)}),$$

$$D^{(k)} = \beta_{k+1} D(w^{(n+1,k)}) + (1 - \beta_{k+1}) D^{(k-1)}.$$

The coefficients  $\alpha_k$  are chosen to maximize the stability interval along the imaginary axis, and the coefficients  $\beta_k$  are chosen to increase the stability interval along the negative real axis.

These schemes do not fall within the standard framework of Runge–Kutta schemes, and they have much larger stability regions [136]. Two schemes which have been found to be particularly effective are tabulated below. The first is a four-stage scheme with two evaluations of dissipation. Its coefficients are

$$\alpha_1 = \frac{1}{3}, \quad \beta_1 = 1,$$

$$\alpha_2 = \frac{4}{15}, \quad \beta_2 = \frac{1}{2},$$

$$\alpha_3 = \frac{5}{9}, \quad \beta_3 = 0,$$

$$\alpha_4 = 1, \quad \beta_4 = 0.$$

(41)



The second is a five-stage scheme with three evaluations of dissipation. Its coefficients are

$$\begin{aligned}\alpha_1 &= \frac{1}{4}, & \beta_1 &= 1, \\ \alpha_2 &= \frac{1}{6}, & \beta_2 &= 0, \\ \alpha_3 &= \frac{3}{8}, & \beta_3 &= 0.56, \\ \alpha_4 &= \frac{1}{2}, & \beta_4 &= 0, \\ \alpha_5 &= 1, & \beta_5 &= 0.44.\end{aligned}\quad (42)$$

### 3.8. Multigrid methods

#### 3.8.1. Acceleration of steady flow calculations

Radical improvements in the rate of convergence to a steady state can be realized by the multigrid time-stepping technique. The concept of acceleration by the introduction of multiple grids was first proposed by Fedorenko [138]. There is by now a fairly well-developed theory of multigrid methods for elliptic equations based on the concept that the updating scheme acts as a smoothing operator on each grid [139,140]. This theory does not hold for hyperbolic systems. Nevertheless, it seems that it ought to be possible to accelerate the evolution of a hyperbolic system to a steady state by using large time steps on coarse grids so that disturbances will be more rapidly expelled through the outer boundary. Various multigrid time-stepping schemes designed to take advantage of this effect have been proposed [65,66,141–145].

One can devise a multigrid scheme using a sequence of independently generated coarser meshes by eliminating alternate points in each coordinate direction. In order to give a precise description of the multigrid scheme, subscripts may be used to indicate the grid. Several transfer operations need to be defined. First the solution vector on grid  $k$  must be initialized as

$$w_k^{(0)} = T_{k,k-1} w_{k-1},$$

where  $w_{k-1}$  is the current value on grid  $k-1$ , and  $T_{k,k-1}$  is a transfer operator. Next, it is necessary to transfer a residual forcing function such that the solution grid  $k$  is driven by the residuals calculated on grid  $k-1$ . This can be accomplished by setting

$$P_k = Q_{k,k-1} R_{k-1}(w_{k-1}) - R_k[w_k^{(0)}],$$

where  $Q_{k,k-1}$  is another transfer operator. Then  $R_k(w_k)$  is replaced by  $R_k(w_k) + P_k$  in the time-stepping scheme. Thus, the multistage scheme is reformulated as

$$w_k^{(1)} = w_k^{(0)} - \alpha_1 \Delta t_k [R_k^{(0)} + P_k],$$

...

$$w_k^{(q+1)} = w_k^{(0)} - \alpha_{q+1} \Delta t_k [R_k^{(q)} + P_k].$$

The result  $w_k^{(m)}$  then provides the initial data for grid  $k+1$ . Finally, the accumulated correction on grid  $k$  has to be transferred back to grid  $k-1$  with the aid of an interpolation operator  $I_{k-1,k}$ . With properly optimized coefficients multistage time-stepping schemes can be very efficient drivers of the multigrid process. A  $W$ -cycle of the type illustrated in Fig. 8 proves to be a particularly effective strategy for managing the work split between the meshes. In a three-dimensional case the number of cells is reduced by a factor of eight on each coarser grid. On examination of the figure, it can therefore be seen that the work measured in units corresponding to a step on the fine grid is of the order of

$$1 + 2/8 + 4/64 + \dots < 4/3$$

and consequently the very large effective time step of the complete cycle costs only slightly more than a single time step in the fine grid.

This procedure has proved extremely successful for the solution of the inviscid Euler equations, but less effective in calculations of turbulent viscous flows at high Reynolds numbers using the Reynolds averaged

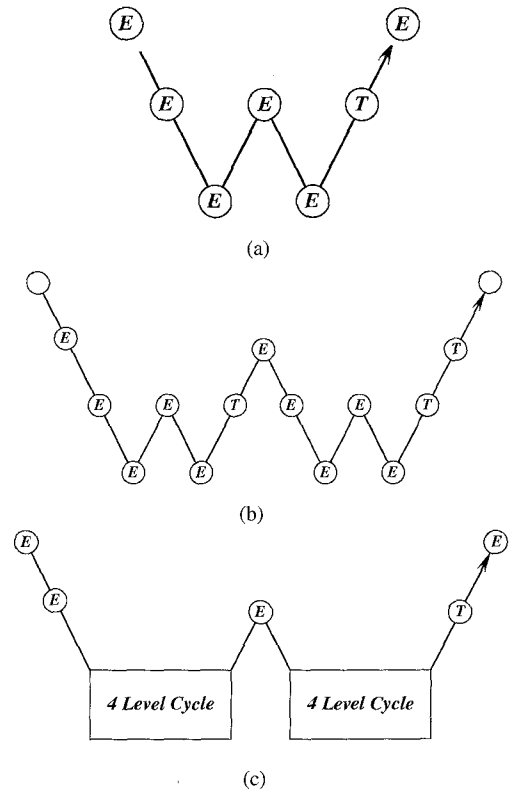


Fig. 8. Multigrid  $W$ -cycle for managing the grid calculation.  $E$ , evaluate the change in the flow for one step;  $T$ , transfer the data without updating the solution. a: 3 Levels. b: 4 Levels. c: 5 Levels.

Navier–Stokes equations. These require highly anisotropic grids with very fine mesh intervals normal to the wall to resolve the boundary layers. While simple multigrid methods still yield fast initial convergence, they tend to slow down as the calculation proceeds to a low asymptotic rate. This has motivated the introduction of semi-coarsening and directional coarsening methods [146–152].

The multigrid method can be applied on unstructured meshes by interpolating between a sequence of separately generated meshes with progressively increasing cell sizes [18,19,153,154]. It is not easy to generate very coarse meshes for complex configurations. An alternative approach, which removes this difficulty, is to automatically generate successively coarser meshes by agglomerating control volumes or by collapsing edges. This approach yields comparable rates of convergence and has proved to be quite robust [155–158].

### 3.8.2. Multigrid implicit schemes for unsteady flow

Time dependent calculations are needed for a number of important applications, such as flutter analysis, or the analysis of the flow past a helicopter rotor, in which the stability limit of an explicit scheme forces the use of much smaller time steps than would be needed for an accurate simulation. In this situation a multigrid explicit scheme can be used in an inner iteration to solve the equations of a fully implicit time stepping scheme [159].

Suppose that (40) is approximated as

$$D_t w^{n+1} + R(w^{n+1}) = 0.$$

Here  $D_t$  is a  $k$ th order accurate backward difference operator of the form

$$D_t = \frac{1}{\Delta t} \sum_{q=1}^k \frac{1}{q} (\Delta^-)^q,$$

where

$$\Delta^- w^{n+1} = w^{n+1} - w^n.$$

Applied to the linear differential equation

$$\frac{dw}{dt} = \alpha w$$

the schemes with  $k = 1, 2$  are stable for all  $\alpha \Delta t$  in the left half-plane (A-stable). Dahlquist has shown that A-stable linear multi-step schemes are at best second order accurate [160]. Gear however, has shown that the schemes with  $k \leq 6$  are stiffly stable [161], and one of the higher order schemes may offer a better compromise between accuracy and stability, depending on the application.

Eq. (40) is now treated as a modified steady state problem to be solved by a multigrid scheme using vari-

able local time steps in a fictitious time  $t^*$ . For example, in the case  $k = 2$  one solves

$$\frac{\partial w}{\partial t^*} + R^*(w) = 0,$$

where

$$R^*(w) = \frac{3}{2\Delta t} w + R(w) - \frac{2}{\Delta t} w^n + \frac{1}{2\Delta t} w^{n-1}$$

and the last two terms are treated as fixed source terms. The first term shifts the Fourier symbol of the equivalent model problem to the left in the complex plane. While this promotes stability, it may also require a limit to be imposed on the magnitude of the local time step  $\Delta t^*$  relative to that of the implicit time step  $\Delta t$ . This may be relieved by a point-implicit modification of the multi-stage scheme [162]. In the case of problems with moving boundaries the equations must be modified to allow for movement and deformation of the mesh.

This method has proved effective for the calculation of unsteady flows that might be associated with wing flutter [163,164] and also in the calculation of unsteady incompressible flows [165]. It has the advantage that it can be added as an option to a computer program which uses an explicit multigrid scheme, allowing it to be used for the efficient calculation of both steady and unsteady flows. A similar approach has been successfully adopted for unsteady flow simulations on unstructured grids by Venkatakrishnan and Mavriplis [166].

### 3.9. Preconditioning

Another way to improve the rate of convergence to a steady state is to multiply the space derivatives in Eq. (1) by a preconditioning matrix  $P$  which is designed to equalize the eigenvalues, so that all the waves can be advanced with optimal time steps. A symmetric preconditioner which equalizes the eigenvalues has been proposed by Van Leer [167]. When the equations are written in stream-aligned coordinates this has the form

$$P = \begin{bmatrix} \frac{\tau}{\beta^2} M^2 & -\frac{\tau}{\beta} M & 0 & 0 & 0 \\ -\frac{\tau}{\beta} M & \frac{\tau}{\beta^2} + 1 & 0 & 0 & 0 \\ 0 & 0 & \tau & 0 & 0 \\ 0 & 0 & 0 & \tau & 0 \\ 0 & 0 & 0 & 0 & 1 \end{bmatrix},$$

where

$$\beta = \begin{cases} \tau = \sqrt{1 - M^2} & \text{if } M < 1, \\ \sqrt{1 - M^2}, \tau = \sqrt{1 - \frac{1}{M^2}} & \text{if } M \geq 1. \end{cases}$$

Turkel has proposed an asymmetric preconditioner which has also proved effective, particularly for flow at low Mach numbers [168]. The use of these preconditioners can lead to instability at stagnation points where there is a zero eigenvalue which cannot be equalized with the eigenvalues  $\pm c$ .

The preconditioners of Van Leer and Turkel do not take account of the effect of differences in the mesh intervals in the different coordinate directions. The need to resolve the boundary layer generally compels the introduction of mesh cells with very high aspect ratios near the boundary, and these can lead to a severe reduction in the rate of convergence to a steady state. Allmaras has analyzed explicit and implicit Jacobi-based preconditioners which include the influence of the mesh intervals [148–150]. Using a block-Jacobi preconditioner with coarsening only in the direction normal to the wall, Pierce has recently obtained impressive results on viscous flows with high aspect ratio grids [151,152]. Mavriplis has successfully combined block preconditioners with line solvers to accelerate the convergence of viscous flow solutions on highly stretched unstructured grids [169].

An alternative approach has recently been proposed by Ta'asan [170], in which the equations are written in a canonical form which separates the equations describing acoustic waves from those describing convection. In terms of the velocity components  $u, v$  and the vorticity  $\omega$ , temperature  $T$ , entropy  $s$  and total enthalpy  $H$ , the equations describing steady two-dimensional flow can be written as

$$\begin{bmatrix} D_1 & D_2 & 0 & 0 & 0 \\ -\frac{\partial}{\partial y} & \frac{\partial}{\partial x} & -1 & 0 & 0 \\ 0 & 0 & -q & -\frac{c^2}{\gamma(\gamma-1)}D_3 & \frac{1}{q}D_3 \\ 0 & 0 & 0 & T\rho Q & 0 \\ 0 & 0 & 0 & 0 & \rho Q \end{bmatrix} \begin{bmatrix} u \\ v \\ \omega \\ s \\ H \end{bmatrix} = 0,$$

where

$$D_1 = \frac{\rho}{c^2} \left( (c^2 - u^2) \frac{\partial}{\partial x} - uv \frac{\partial}{\partial y} \right),$$

$$D_2 = \frac{\rho}{c^2} \left( (c^2 - u^2) \frac{\partial}{\partial y} - uv \frac{\partial}{\partial x} \right),$$

$$D_3 = v \frac{\partial}{\partial x} - u \frac{\partial}{\partial y},$$

$$Q = u \frac{\partial}{\partial x} + v \frac{\partial}{\partial y}$$

and

$$q^2 = u^2 + v^2.$$

Here the first three equations describe an elliptic system if the flow is subsonic, while the remaining equations are convective. Now separately optimized multigrid procedures are used to solve the two sets of equations, which are essentially decoupled. An alternative approach to the optimal splitting of the flow equations into convective and acoustic parts has been developed by Sidilkover [171,172].

### 3.10. High order schemes and mesh refinement

The need both to improve the accuracy of computational simulations, and to assure known levels of accuracy is the focus of ongoing research. The main routes to improving the accuracy are to increase the order of the discrete scheme, and reduce the mesh interval. High order difference methods are most easily implemented on Cartesian, or at least extremely smooth grids. The expansion of the stencil as the order is increased leads to the need for complex boundary conditions. Compact schemes keep the stencil as small as possible [173–175]. On simple domains, spectral methods are particularly effective, especially in the case of periodic boundary conditions, and can be used to produce exponentially fast convergence of the error as the mesh interval is decreased [176,177]. A compromise is to divide the field into subdomains and introduce high order elements. This approach is used in the spectral element method [178].

High order difference schemes and spectral methods have proven particularly useful in direct Navier–Stokes simulations of transient and turbulent flows. High order methods are also beneficial in computational aero-acoustics, where it is desired to track waves over long distances with minimum error. If the flow contains shock waves or contact discontinuities, the ENO method may be used to construct high order nonoscillatory schemes.

In multidimensional flow simulations, global reduction of the mesh interval can be prohibitively expensive, motivating the use of adaptive mesh refinement procedures which reduce the local mesh width  $h$  if there is an indication that the error is too large [179–185]. In such  $h$ -refinement methods, simple error indicators such as local solution gradients may be used. Alternatively, the discretization error may be estimated by comparing quantities calculated with two mesh widths, say on the current mesh and a coarser mesh with double the mesh interval. Procedures of this kind may also be used to provide a posteriori estimates of the error once the calculation is completed.

This kind of local adaptive control can also be applied to the local order of a finite element method to produce a  $p$ -refinement method, where  $p$  represents the order of the polynomial basis functions. Finally, both  $h$ - and  $p$ -refinement can be combined to produce an  $h$ - $p$  method in which  $h$  and  $p$  are locally optimized to yield a solution with minimum error [11]. Such methods can achieve

exponentially fast convergence, and are well established in computational solid mechanics.

#### 4. Current status of numerical simulation

This section presents some representative numerical results which confirm the properties of the algorithms which have been reviewed in the last section. These have been drawn from the work of the author and his associates. They also illustrate the kind of calculation which can be performed in an industrial environment, where rapid turn around is important to allow the quick assessment of design changes, and computational costs must be limited.

##### 4.1. One-dimensional shock

In order to verify the discrete structure of stationary shocks, calculations were performed for a one-dimensional problem with initial data containing left and right states compatible with the Rankine Hugoniot conditions. An intermediate state consisting of the arithmetic average of the left and right states was introduced at a single cell in the center of the domain. With this intermediate state the system is not in equilibrium, and the time dependent equations were solved to find an equilibrium solution with a stationary shock wave separating the left and right states. Table 1 shows the result for a shock wave at Mach 20. This calculation used the H-CUSP scheme, which allows a solution with constant stagnation enthalpy. The SLIP-JST construction was used with the limiter defined by Eq. (23), and  $q = 3$ . The table shows the values of  $\rho$ ,  $u$ ,  $H$ ,  $p$ ,  $M$  and the entropy  $S = \log p/\rho\gamma - \log(p_L/\rho_L^\gamma)$ . A perfect one point shock structure is displayed. The entropy is zero to 4 decimal places upstream of the shock, exhibits a slight excursion at the interior point, and is constant to 4 decimal places downstream of the shock. It may be noted that the mass, momentum and energy of the initial data are not compatible with the final equilibrium state. According to conservation arguments the total mass, momentum and energy

must remain constant if the outflow flux  $f_R$  remains equal to the inflow flux  $f_L$ . Therefore  $f_R$  must be allowed to vary according to an appropriate outflow boundary condition to allow the total mass, momentum and energy to be adjusted to values compatible with equilibrium.

##### 4.2. Euler calculations for airfoils and wings

The results of transonic flow calculations for two well-known airfoils, the RAE 2822 and the NACA 0012, are presented in Figs. 21–23. The H-CUSP scheme was again used with the SLIP-JST construction. The limiter defined by Eq. (23) was used with  $q = 3$ . The 5 stage time-stepping scheme (42) was augmented by the multigrid scheme described in Section 4.2 to accelerate convergence to a steady state. The equations were discretized on meshes with O-topology extending out to a radius of about 100 chords. In each case the calculations were performed on a sequence of successively finer meshes from  $40 \times 8$  to  $320 \times 64$  cells, while the multigrid cycles on each of these meshes descended to a coarsest mesh of  $10 \times 2$  cells. Figs. 21–23 show the final results on  $320 \times 64$  meshes for the RAE 2822 airfoil at Mach 0.75 and  $3^\circ$  angle of attack, and for the NACA 0012 airfoil at Mach 0.8 and  $1.25^\circ$  angle of attack, and also at Mach 0.85 and  $1^\circ$  angle of attack. In the pressure distributions the pressure coefficient  $C_p = (p - p_\infty)/\frac{1}{2}\rho_\infty q_\infty^2$  is plotted with the negative (suction) pressures upward, so that the upper curve represents the flow over the upper side of a lifting airfoil. The convergence histories show the mean rate of change of the density, and also the total number of supersonic points in the flow field, which provides a useful measure of the global convergence of transonic flow calculations such as these. In each case the convergence history is shown for 100 cycles, while the pressure distribution is displayed after a sufficient number of cycles for its convergence. The pressure distribution of the RAE 2822 airfoil converged in only 25 cycles. Convergence was slower for the NACA 0012 airfoil. In the case of flow at Mach 0.8 and  $1.25^\circ$  angle of attack, additional cycles were needed to damp out a wave downstream of the weak shock wave on the lower surface.

As a further check on accuracy the drag coefficient should be zero in subsonic flow, or in shock free transonic flow. Table 2 shows the computed drag coefficient on a sequence of three meshes for three examples. The first two are subsonic flows over the RAE 2822 and NACA 0012 airfoils at Mach 0.5 and  $3^\circ$  angle of attack. The third is the flow over the shock free Korn airfoil at its design point of Mach 0.75 and  $0^\circ$  angle of attack. In all three cases the drag coefficient is calculated to be zero to four digits on a  $160 \times 32$  mesh.

As a further test of the performance of the H-CUSP scheme, the flow past the ONERA M6 wing was calculated on a mesh with C-H topology and  $192 \times 32 \times 48 = 294,912$  cells. Fig. 24 shows the result at

Table 1  
Shock wave at Mach 20

$I$	$\rho$	$H$	$p$	$M$
19	1.0000	283.5000	1.0000	20.0000
20	1.0000	283.5000	1.0000	20.0000
21	1.0000	283.5000	1.0000	20.0000
22	4.1924	283.4960	307.4467	0.7229
23	5.9259	283.4960	466.4889	0.3804
24	5.9259	283.4960	466.4889	0.3804
25	5.9259	283.4960	466.4889	0.3804

Table 2  
Drag coefficient on a sequence of meshes

Mesh	RAE 2822 Mach 0.50 $\alpha$ 3°	NACA 0012 Mach 0.50 $\alpha$ 3°	Korn Airfoil Mach 0.75 $\alpha$ 0°
40 × 8	0.0062	0.0047	0.0098
80 × 16	0.0013	0.0008	0.0017
160 × 32	0.0000	0.0000	0.0000

Mach 0.84 and 3.06° angle of attack. This again verifies the nonoscillatory character of the solution, and the sharp resolution of shock waves. In this case 50 cycles were sufficient for convergence of the pressure distributions.

Fig. 9 shows a calculation of the Northrop YF23 by R.J. Busch Jr., who used the author's FLO57 code to solve the Euler equations [186]. Although an inviscid model of the flow was used, it can be seen that the simulations are in good agreement with wind tunnel measurements both at Mach 0.90, with angles of attack of 0°, 8° and 16°, and at Mach 1.5 with angles of attack of 0°, 4° and 8°. At a high angle of attack the flow separates from the leading edge, and this example shows that in situations where the point of separation is fixed, an inviscid model may still produce a useful prediction. Thus valuable information for the aerodynamic design could be obtained with a relatively inexpensive computational model.

The next figures show the results of calculations using the AIRPLANE code developed by T.J. Baker and the author, to solve the Euler equations on an unstructured mesh. This provides the flexibility to treat arbitrarily complex configurations without the need to spend months developing an acceptable mesh. Figs. 10 and 11 show calculations for supersonic transport configurations which were performed by Susan Cliff. The agreement with experimental data is quite good, and it has also been possible to predict the sonic boom signature [187]. Fig. 12 shows an Euler calculation for the McDonnell Douglas MD11 with flow through the engine nacelles, using 348,407 mesh points of 2,100,466 tetrahedra. This calculation takes 4 h on an IBM 590 workstation. A parallel version of the code has been developed in collaboration with W.S. Chen, and the same calculation can be performed in 16 min using 16 processors of an IBM SP2. The parallel speed-up for the MD11 is shown in Table 3.

#### 4.3. Viscous flow calculations

The next figures show viscous simulations based on the solution of the Reynolds averaged Navier–Stokes equations with turbulence models. Fig. 13 shows a two-dimensional calculation for the RAE 2822 airfoil by

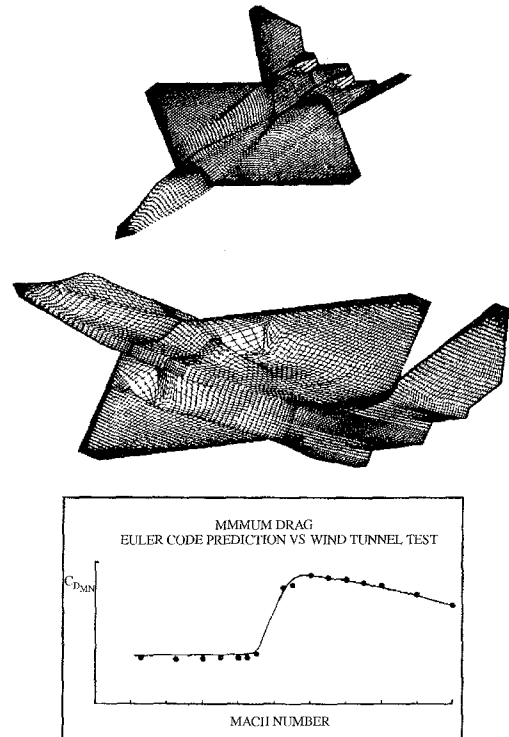


Fig. 9. Comparison of experimental and computed drag rise curve for the YF-23 (Supplied by R.J. Bush Jr.).

Martinelli. The vertical axis represents the negative pressure coefficient, and there is a shock wave half way along the upper surface. This example confirms that in the absence of significant shock induced separation, simulations performed on a sufficiently fine mesh ( $512 \times 64$ ) can produce excellent agreement with experimental data. Fig. 20 shows a simulation of the McDonnell-Douglas F18 performed by R.M. Cummings, Y.M. Rizk, L.B. Schiff and N.M. Chaderjian at NASA Ames [188]. They used a multiblock mesh with about 900,000 mesh points. While this is probably not enough for an accurate quantitative prediction, the agreement with both the experimental data and the visualization are quite good.

Fig. 14 shows an unsteady flow calculation for a pitching airfoil performed by J.J. Alonso using the code UFLO82, which he jointly developed with L. Martinelli and the author [164]. This uses the multigrid implicit scheme described in Section 3.7.2 which allows the number of time steps to be reduced from several thousand to 36 per pitching cycle. The agreement with experimental data is quite good.

#### 4.4. Ship wave resistance calculations

Figs. 15–17 show the results of an application of the same multigrid finite volume techniques to the

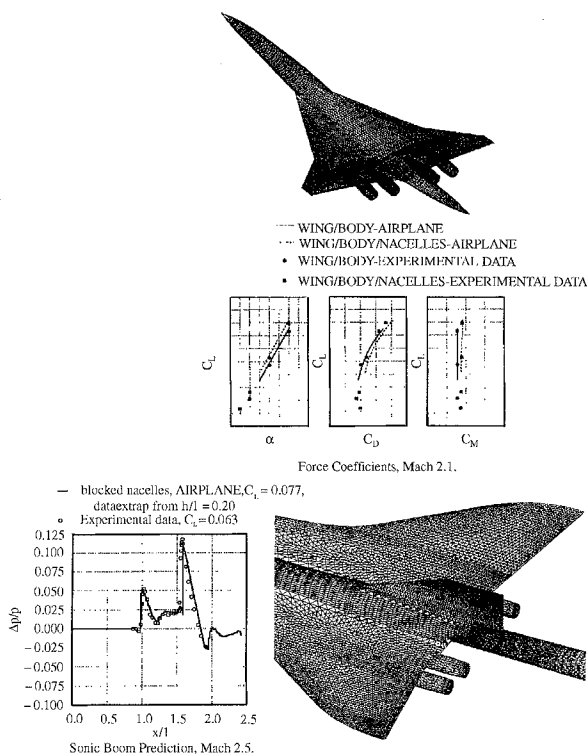


Fig. 10. Comparison of experimental and calculated results for a HSCT configuration.

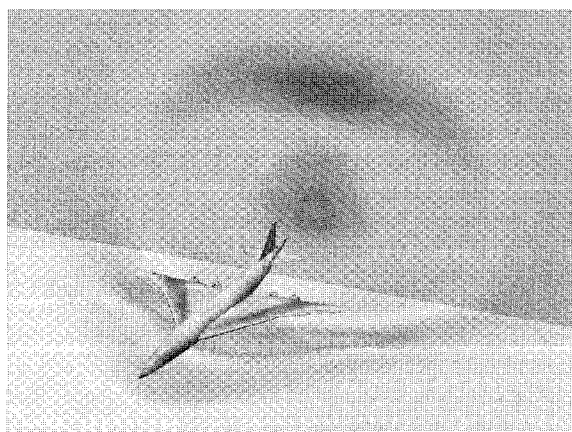


Fig. 11. Pressure contours and sonic boom on a representative HSCT configuration.

calculation of the flow past a naval frigate, using a code which was developed by Farmer, Martinelli and the author [189]. The mesh was adjusted during the course of the calculation to conform to the free surface in order to satisfy the exact nonlinear boundary condition, while artificial compressibility was used to treat the incompressible flow equations.

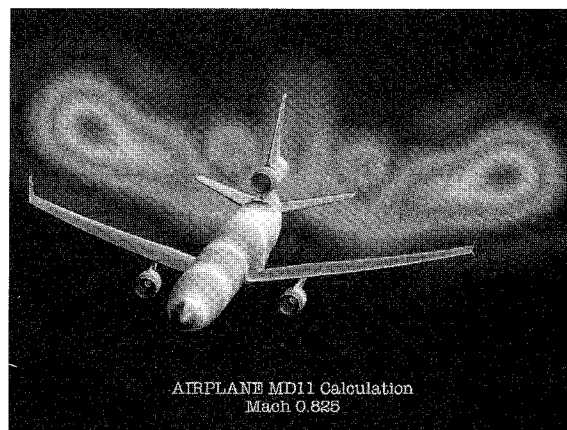


Fig. 12. Computed pressure field for a McDonnell Douglas MD11.

Table 3  
AIRPLANE parallel performance on the SP2, MD-11 model

No. of nodes	Seconds/cycle	Speed up
1	36.03	1.00
2	18.11	1.99
4	9.11	3.96
8	4.66	7.73
16	2.39	15.08

## 5. Aerodynamic shape optimization

### 5.1. Optimization and design

Traditionally, the process of selecting design variations has been carried out by trial and error, relying on the intuition and experience of the designer. With currently available equipment the turn around for numerical simulations is becoming so rapid that it is feasible to examine an extremely large number of variations. It is not at all likely that repeated trials in an interactive design and analysis procedure can lead to a truly optimum design. In order to take full advantage of the possibility of examining a large design space the numerical simulations need to be combined with automatic search and optimization procedures. This can lead to automatic design methods which will fully realize the potential improvements in aerodynamic efficiency.

The simplest approach to optimization is to define the geometry through a set of design parameters, which may, for example, be the weights  $\alpha_i$  applied to a set of shape functions  $b_i(x)$  so that the shape is represented as

$$f(x) = \sum \alpha_i b_i(x).$$

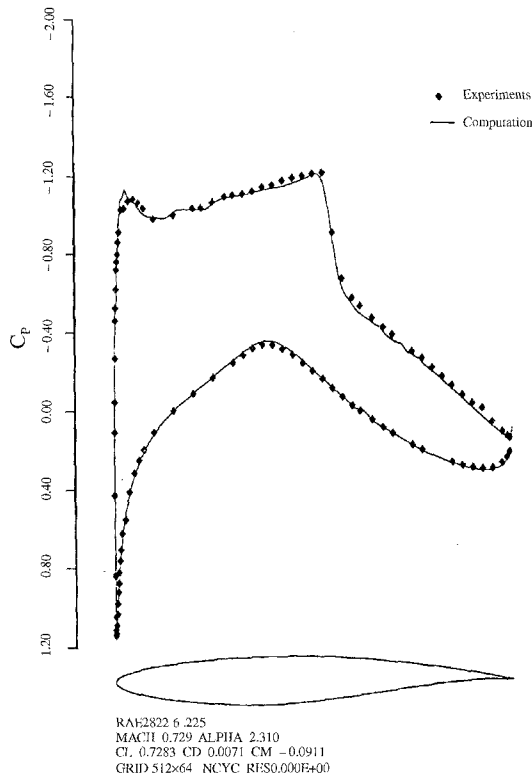


Fig. 13. Two-dimensional turbulent viscous calculation (by Luigi Martinelli).

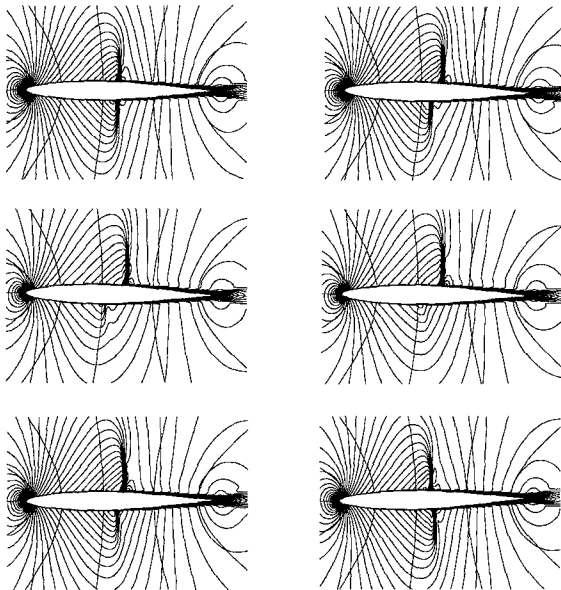


Fig. 14. Mach number contours. Pitching airfoil case.  $Re = 1.0 \times 10^6$ ,  $M_\infty = 0.796$ ,  $K_c = 0.202$ .

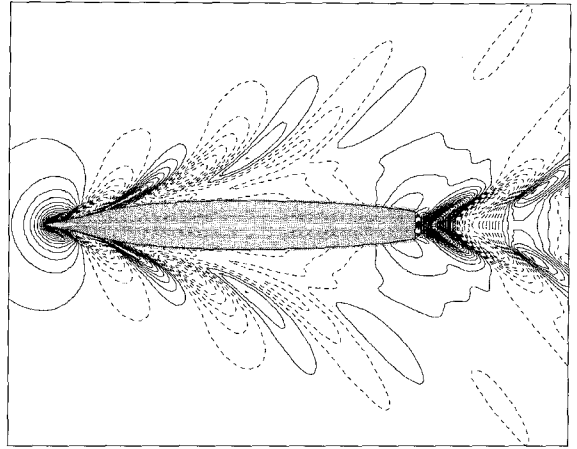


Fig. 15. Contours of surface wave elevation for a combatant ship.

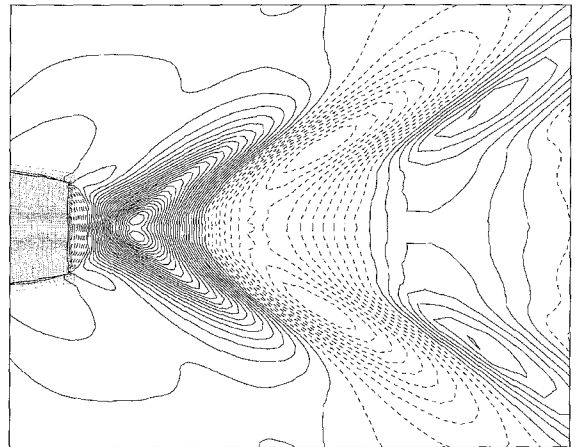


Fig. 16. Contours of surface wave elevation near the transom stern.

Then a cost function  $I$  is selected which might, for example, be the drag coefficient at a final lift coefficient, and  $I$  is regarded as a function of the parameters  $\alpha_i$ . The sensitivities  $\partial I / \partial \alpha_i$  may now be estimated by making a small variation  $\delta \alpha_i$  in each design parameter in turn and recalculating the flow to obtain the change in  $I$ . Then

$$\frac{\partial I}{\partial \alpha_i} \approx \frac{I(\alpha_i + \delta \alpha_i) - I(\alpha_i)}{\delta \alpha_i}.$$

The gradient vector  $\partial I / \partial \alpha$  may now be used to determine a direction of improvement. The simplest procedure is to make a step in the negative gradient direction by setting

$$\alpha^{n+1} = \alpha^n - \lambda \frac{\partial I}{\partial \alpha},$$

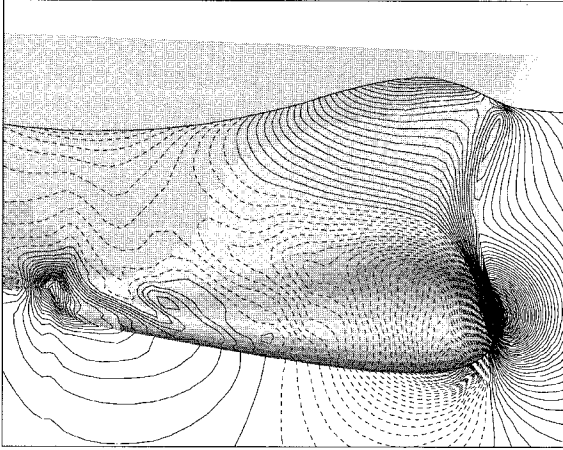


Fig. 17. Pressure contours in the bow region.

so that to first order

$$I + \delta I = I - \frac{\partial I^T}{\partial \alpha} \delta \alpha = I - \lambda \frac{\partial I^T}{\partial \alpha} \frac{\partial I}{\partial \alpha}.$$

More sophisticated search procedures may be used such as quasi-Newton methods, which attempt to estimate the second derivative  $\partial^2 I / \partial \alpha_i \partial \alpha_j$  of the cost function from changes in the gradient  $\partial I / \partial \alpha$  in successive optimization steps. These methods also generally introduce line searches to find the minimum in the search direction which is defined at each step. The main disadvantage of this approach is the need for a number of flow calculations proportional to the number of design variables to estimate the gradient. The computational costs can thus become prohibitive as the number of design variables is increased.

An alternative approach is to cast the design problem as a search for the shape that will generate the desired pressure distribution. This approach recognizes that the designer usually has an idea of the kind of pressure distribution that will lead to the desired performance. Thus, it is useful to consider the inverse problem of calculating the shape that will lead to a given pressure distribution. The method has the advantage that only one flow solution is required to obtain the desired design. Unfortunately, a physically realizable shape may not necessarily exist, unless the pressure distribution satisfies certain constraints. Thus the problem must be very carefully formulated; otherwise it may be ill posed.

The difficulty that the target pressure may be unattainable may be circumvented by treating the inverse problem as a special case of the optimization problem, with a cost function which measures the error in the solution of the inverse problem. For example, if  $p_d$  is the desired surface pressure, one may take the cost function to be an

integral over the body surface of the square of the pressure error,

$$I = \frac{1}{2} \int_{\mathcal{B}} (p - p_d)^2 d\mathcal{B}$$

or possibly a more general Sobolev norm of the pressure error. This has the advantage of converting a possibly ill posed problem into a well posed one. It has the disadvantage that it incurs the computational costs associated with optimization procedures.

## 5.2. Application of control theory

In order to reduce the computational costs, it turns out that there are advantages in formulating both the inverse problem and more general aerodynamic problems within the framework of the mathematical theory for the control of systems governed by partial differential equations [190]. A wing, for example, is a device to produce lift by controlling the flow, and its design can be regarded as a problem in the optimal control of the flow equations by variation of the shape of the boundary. If the boundary shape is regarded as arbitrary within some requirements of smoothness, then the full generality of shapes cannot be defined with a finite number of parameters, and one must use the concept of the Frechet derivative of the cost with respect to a function. Clearly, such a derivative cannot be determined directly by finite differences of the design parameters because there are now an infinite number of these. Using techniques of control theory, however, the gradient can be determined indirectly by solving an adjoint equation which has coefficients defined by the solution of the flow equations. The cost of solving the adjoint equation is comparable to that of solving the flow equations. Thus, the gradient can be determined with roughly the computational costs of two flow solutions, independently of the number of design variables, which may be infinite if the boundary is regarded as a free surface. The underlying concepts are clarified by the following abstract description of the adjoint method. For flow about an airfoil or wing (see Figs. 18 and 19), the aerodynamic properties which define the cost function are functions of the flow-field variables ( $w$ ) and the physical location of the boundary, which may be represented by the function  $\mathcal{F}$ , say. Then

$$I = I(w, \mathcal{F})$$

and a change in  $\mathcal{F}$  results in a change

$$\delta I = \left[ \frac{\partial I^T}{\partial w} \right]_I \delta w + \left[ \frac{\partial I^T}{\partial \mathcal{F}} \right]_{II} \delta \mathcal{F} \quad (43)$$

in the cost function. Here, subscripts I and II are used to distinguish the contributions due to the variation  $\delta w$  in the flow solution from the change associated directly with the modification  $\delta \mathcal{F}$  in the shape. This notation



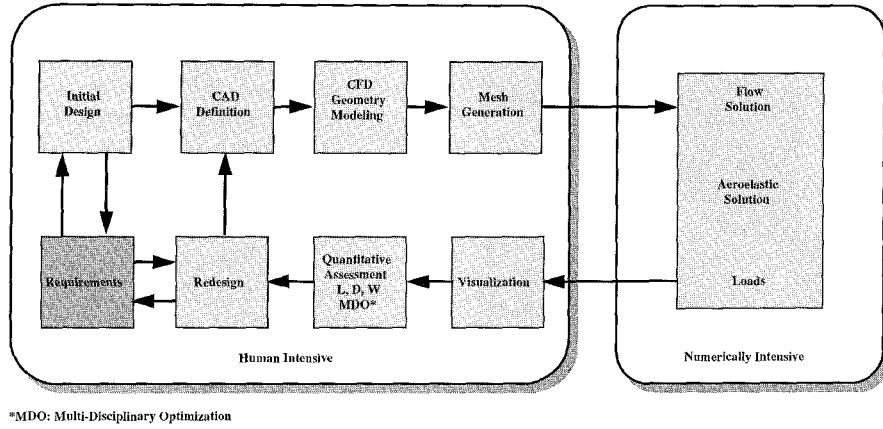


Fig. 18. Concept for a numerical wind tunnel.

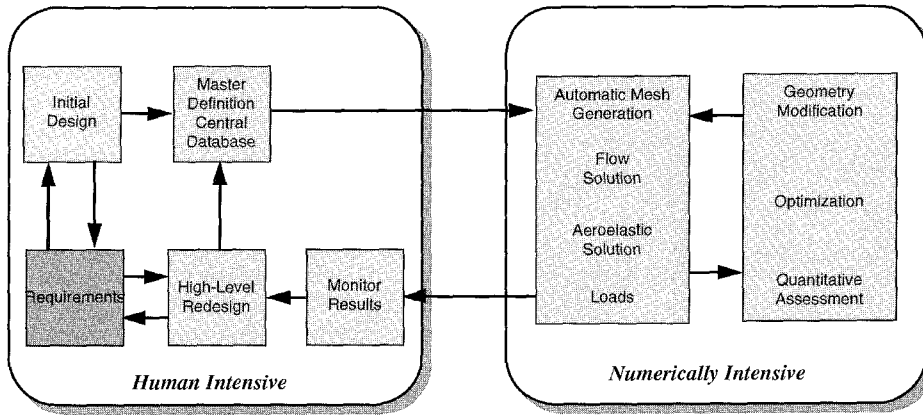


Fig. 19. Advanced numerical wind tunnel.

assists in grouping the numerous terms that arise during the derivation of the full Navier–Stokes adjoint operator, outlined in the next section, so that the basic structure of the approach as it is sketched in the present section can easily be recognized (Fig. 20).

Suppose that the governing equation  $R$  which expresses the dependence of  $w$  and  $\mathcal{F}$  within the flowfield domain  $D$  can be written as

$$R(w, \mathcal{F}) = 0. \quad (44)$$

Then  $\delta w$  is determined from the equation

$$\delta R = \left[ \frac{\partial R}{\partial w} \right]_I \delta w + \left[ \frac{\partial R}{\partial \mathcal{F}} \right]_{II} \delta \mathcal{F} = 0. \quad (45)$$

Since the variation  $\delta R$  is zero, it can be multiplied by a Lagrange multiplier  $\psi$  and subtracted from the variation  $\delta I$  without changing the result. Thus Eq. (43) can be

replaced by

$$\begin{aligned} \delta I &= \frac{\partial I^T}{\partial w} \delta w + \frac{\partial I^T}{\partial \mathcal{F}} \delta \mathcal{F} - \psi^T \left( \left[ \frac{\partial R}{\partial w} \right] \delta w + \left[ \frac{\partial R}{\partial \mathcal{F}} \right] \delta \mathcal{F} \right) \\ &= \left\{ \frac{\partial I^T}{\partial w} - \psi^T \left[ \frac{\partial R}{\partial w} \right] \right\}_I \delta w + \left\{ \frac{\partial I^T}{\partial \mathcal{F}} - \psi^T \left[ \frac{\partial R}{\partial \mathcal{F}} \right] \right\}_{II} \delta \mathcal{F}. \end{aligned} \quad (46)$$

Choosing  $\psi$  to satisfy the adjoint equation

$$\left[ \frac{\partial R}{\partial w} \right]^T \psi = \frac{\partial I}{\partial w}, \quad (47)$$

the first term is eliminated, and we find that

$$\delta I = \mathcal{G} \delta \mathcal{F}, \quad (48)$$

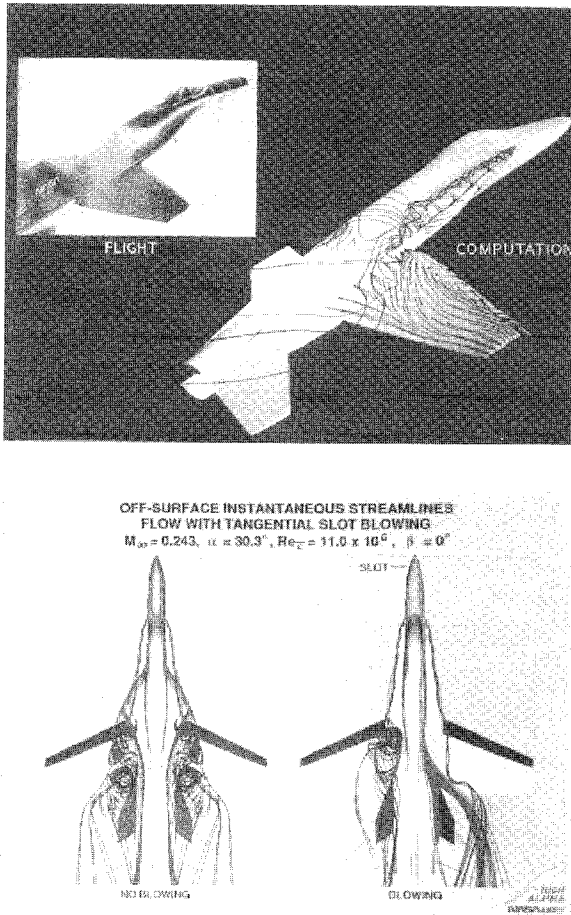


Fig. 20. Navier-Stokes predictions for the F-18 Wing-Fuselage at large incidence.

where

$$\mathcal{G} = \frac{\partial I^T}{\partial \mathcal{F}} - \psi^T = \left[ \frac{\partial R}{\partial \mathcal{F}} \right].$$

The advantage is that (48) is independent of  $\delta w$ , with the result that the gradient of  $I$  with respect to an arbitrary number of design variables can be determined without the need for additional flow-field evaluations. In the case that (44) is a partial differential equation, the adjoint equation (47) is also a partial differential equation and determination of the appropriate boundary conditions requires careful mathematical treatment.

In Ref. [191] the author derived the adjoint equations for transonic flows modeled by both the potential flow equation and the Euler equations. The theory was developed in terms of partial differential equations, leading to an adjoint partial differential equation. In order to obtain numerical solutions both the flow and the adjoint equations must be discretized. The control theory might

be applied directly to the discrete flow equations which result from the numerical approximation of the flow equations by finite element, finite volume or finite difference procedures. This leads directly to a set of discrete adjoint equations with a matrix which is the transpose of the Jacobian matrix of the full set of discrete nonlinear flow equations. On a three-dimensional mesh with indices  $i, j, k$  the individual adjoint equations may be derived by collecting together all the terms multiplied by the variation  $\delta w_{i,j,k}$  of the discrete flow variable  $w_{i,j,k}$ . The resulting discrete adjoint equations represent a possible discretization of the adjoint partial differential equation. If these equations are solved exactly they can provide an exact gradient of the inexact cost function which results from the discretization of the flow equations. The discrete adjoint equations derived directly from the discrete flow equations become very complicated when the flow equations are discretized with higher order upwind biased schemes using flux limiters. On the other hand any consistent discretization of the adjoint partial differential equation will yield the exact gradient in the limit as the mesh is refined. The trade-off between the complexity of the adjoint discretization, the accuracy of the resulting estimate of the gradient, and its impact on the computational cost to approach an optimum solution is a subject of ongoing research.

The true optimum shape belongs to an infinitely dimensional space of design parameters. One motivation for developing the theory for the partial differential equations of the flow is to provide an indication in principle of how such a solution could be approached if sufficient computational resources were available. Another motivation is that it highlights the possibility of generating ill posed formulations of the problem. For example, if one attempts to calculate the sensitivity of the pressure at a particular location to changes in the boundary shape, there is the possibility that a shape modification could cause a shock wave to pass over that location. Then the sensitivity could become unbounded. The movement of the shock, however, is continuous as the shape changes. Therefore a quantity such as the drag coefficient, which is determined by integrating the pressure over the surface, also depends continuously on the shape. The adjoint equation allows the sensitivity of the drag coefficient to be determined without the explicit evaluation of pressure sensitivities which would be ill posed.

The discrete adjoint equations, whether they are derived directly or by discretization of the adjoint partial differential equation, are linear. Therefore they could be solved by direct numerical inversion. In three-dimensional problems on a mesh with, say,  $n$  intervals in each coordinate direction, the number of unknowns is proportional to  $n^3$  and the bandwidth to  $n^2$ . The complexity of direct inversion is proportional to the number of unknowns multiplied by the square of the bandwidth, resulting in a complexity proportional to  $n^7$ . The cost of

direct inversion can thus become prohibitive as the mesh is refined, and it becomes more efficient to use iterative solution methods. Moreover, because of the similarity of the adjoint equations to the flow equations, the same iterative methods which have been proved to be efficient for the solution of the flow equations are efficient for the solution of the adjoint equations.

The control theory formulation for optimal aerodynamic design has proved effective in a variety of applications [137,192,193]. Pironneau has studied the use of control theory for optimal shape design of systems governed by elliptic equations [194], and more recently the Navier–Stokes equations, and also wave reflection problems [195]. The adjoint equations have also been used by Baysal and Eleshaky [196], and by Ta’asan, Kuruvila and Salas [197], who have implemented a one shot approach in which the constraint represented by the flow equations is only required to be satisfied by the final converged solution. In their work, computational costs are also reduced by applying multigrid techniques to the geometry modifications as well as the solution of the flow and adjoint equations. Adjoint methods have been applied to incompressible viscous flow problems by Cabuk and Modi [198,199] and by Desai and Ito [200]. Recent applications of adjoint methods on unstructured meshes include the work of Anderson and Venkatakrishnan [201], and Elliot and Peraire [202].

### 5.3. Three-dimensional design using the compressible Euler and Navier–Stokes equations

In order to illustrate the application of control theory to aerodynamic design problems, this section treats three-dimensional wing design using the compressible Euler and Navier–Stokes equations to model the flow. In comparison with incompressible viscous flow, the adjoint equations contain numerous extra terms which arise from the variation of the energy equation. In order to simplify the calculation of the effect of shape changes it is convenient to introduce a body-fitted coordinate system, so that the flow and adjoint equations are solved in a fixed computational domain. Suppose that the transformation to computational coordinates  $(\xi_1, \xi_2, \xi_3)$  is defined by the metrics

$$K_{ij} = (K), \quad K_{ij}^{-1} = \left[ \frac{\partial \xi_i}{\partial x_j} \right].$$

The Navier–Stokes equations (1–3) can then be written in the computational domain as

$$\frac{\partial(jw)}{\partial t} + R(w) = 0 \quad \text{in } \mathcal{D}, \quad (49)$$

where

$$R(w) = \frac{\partial}{\partial \xi_i} (F_i - F_{vi}), \quad (50)$$

where the inviscid and viscous flux contributions are now defined with respect to the computational cell faces by  $F_i = S_{ij}f_j$  and  $F_{vi} = S_{ij}f_{vj}$ , and the quantity  $S_{ij} = JK_{ij}^{-1}$  is used to represent the projection of the  $\xi_i$  cell face along the  $x_j$ -axis. For convenience, the coordinates  $\xi_i$  describing the fixed computational domain are chosen so that each boundary conforms to a constant value of one of these coordinates. Variations in the shape then result in corresponding variations in the mapping derivatives defined by  $K_{ij}$ .

Suppose that the performance is measured by a cost function

$$I = \int_{\mathcal{B}} \mathcal{M}(w, S) dB_{\xi} + \int_{\mathcal{D}} \mathcal{P}(w, S) dD_{\xi},$$

containing both boundary and field contributions where  $dB_{\xi}$  and  $dD_{\xi}$  are the surface and volume elements in the computational domain. In general,  $\mathcal{M}$  and  $\mathcal{P}$  will depend on both the flow variables  $w$  and the metrics  $S$  defining the computational space. The design problem is now treated as a control problem where the boundary shape represents the control function, which is chosen to minimize  $I$  subject to the constraints defined by the flow equations (49). A shape change produces a variation in the flow solution  $\delta w$  and the metrics  $\delta S$  which in turn produce a variation in the cost function

$$\delta I = \int_{\mathcal{B}} \delta \mathcal{M}(w, S) dB_{\xi} + \int_{\mathcal{D}} \delta \mathcal{P}(w, S) dD_{\xi}. \quad (51)$$

This can be split as

$$\delta I = \delta I_I + \delta I_{II} \quad (52)$$

with

$$\delta \mathcal{M} = [\mathcal{M}_w]_I \delta w + \delta \mathcal{M}_{II},$$

$$\delta \mathcal{P} = [\mathcal{P}_w]_I \delta w + \delta \mathcal{P}_{II}, \quad (53)$$

where we continue to use subscripts I and II to distinguish between the contributions associated with the variation of the flow solution  $\delta w$  and those associated with the metric variations  $\delta S$ . Thus  $[\mathcal{M}_w]_I$  and  $[\mathcal{P}_w]_I$  represent  $\partial \mathcal{M} / \partial w$  and  $\partial \mathcal{P} / \partial w$  with the metrics fixed, while  $\delta \mathcal{M}_{II}$  and  $\delta \mathcal{P}_{II}$  represent the contribution of the metric variations  $\delta S$  to  $\delta \mathcal{M}$  and  $\delta \mathcal{P}$ .

In the steady state, the constraint equation (53) specifies the variation of the state vector  $\delta w$  by

$$\delta R = \frac{\partial}{\partial \xi_i} \delta (F_i - F_{vi}) = 0. \quad (54)$$

Here, also,  $\delta R$ ,  $\delta F_i$  and  $\delta F_{vi}$  can be split into contributions associated with  $\delta w$  and  $\delta S$  using the notation

$$\delta R = \delta R_I + \delta R_{II},$$

$$\delta F_i = [F_{iw}]_I \delta w + \delta F_{iII},$$

$$\delta F_{vi} = [F_{v iw}]_I \delta w + \delta F_{vi II}. \quad (55)$$

The inviscid contributions are easily evaluated as

$$[F_{iw}]_I = S_{ij} \frac{\partial f_i}{\partial w}, \quad \delta F_{vii} = \delta S_{ij} f_j.$$

The details of the viscous contributions are complicated by the additional level of derivatives in the stress and heat flux terms.

Multiplying by a costate vector  $\psi$ , which will play an analogous role to the Lagrange multiplier introduced in Eq. (46), and integrating over the domain produces

$$\int_{\mathcal{D}} \psi^T \frac{\partial}{\partial \xi_i} \delta(F_i - F_{vi}) d\mathcal{D}_\xi = 0. \quad (56)$$

Assuming that  $\psi$  is differentiable the terms with subscript I may be integrated by parts to give

$$\begin{aligned} & \int_{\mathcal{B}} n_i \psi^T \delta(F_i - F_{vi})_I d\mathcal{B}_\xi \\ & - \int_{\mathcal{D}} \frac{\partial \psi^T}{\partial \xi_i} \delta(F_i - F_{vi})_I d\mathcal{D}_\xi + \int_{\mathcal{D}} \psi^T \delta R_{II} d\mathcal{D}_\xi = 0. \end{aligned} \quad (57)$$

This equation results directly from taking the variation of the weak form of the flow equations, where  $\psi$  is taken to be an arbitrary differentiable test function. Since the left hand expression equals zero, it may be subtracted from the variation in the cost function (51) to give

$$\begin{aligned} \delta I &= \delta I_{II} - \int_{\mathcal{D}} \psi^T \delta R_{II} d\mathcal{D}_\xi \\ & - \int_{\mathcal{B}} [\delta \mathcal{M}_I - n_i \psi^T \delta(F_i - F_{vi})_I] d\mathcal{B}_\xi \\ & + \int_{\mathcal{D}} \left[ \delta \mathcal{P}_I + \frac{\partial \psi^T}{\partial \xi_i} \delta(F_i - F_{vi})_I \right] d\mathcal{D}_\xi. \end{aligned} \quad (58)$$

Now, since  $\psi$  is an arbitrary differentiable function, it may be chosen in such a way that  $\delta I$  no longer depends explicitly on the variation of the state vector  $\delta w$ . The gradient of the cost function can then be evaluated directly from the metric variations without having to recompute the variation  $\delta w$  resulting from the perturbation of each design variable.

Comparing Eqs. (53) and (55), the variation  $\delta w$  may be eliminated from (58) by equating all field terms with subscript “I” to produce a differential adjoint system governing  $\psi$

$$\frac{\partial \psi^T}{\partial \xi_i} [F_{iw} - F_{vii}]_I + [\mathcal{P}_w]_I = 0 \quad \text{in } \mathcal{D}. \quad (59)$$

The corresponding adjoint boundary condition is produced by equating the subscript “I” boundary terms in Eq. (58) to produce

$$n_i \psi^T [F_{iw} - F_{vii}]_I = [\mathcal{M}_w]_I \quad \text{on } \mathcal{B}. \quad (60)$$

The remaining terms from Eq. (58) then yield a simplified expression for the variation of the cost function which defines the gradient

$$\delta I = \delta I_{II} + \int_{\mathcal{D}} \psi^T \delta R_{II} d\mathcal{D}_\xi, \quad (61)$$

which consists purely of the terms containing variations in the metrics with the flow solution fixed. Hence, an explicit formula for the gradient can be derived once the relationship between mesh perturbations and shape variations is defined.

The details of the derivation of the adjoint equation are quite complicated, and have been presented in [191,203,204]. Taking the transpose of Eq. (59), the inviscid adjoint equation may be written as

$$C_i^T \frac{\partial \psi}{\partial \xi_i} = 0 \quad \text{in } \mathcal{D}, \quad (62)$$

where the inviscid Jacobian matrices in the transformed space are given by

$$C_i = S_{ij} \frac{\partial f_j}{\partial w}.$$

The derivation of the viscous adjoint terms is simplified by transforming to the primitive variables

$$\tilde{w}^T = (\rho, u_1, u_2, u_3, p)^T,$$

because the viscous stresses depend on the velocity derivatives  $\partial u_i / \partial x_j$ , while the heat fluxes can be expressed as

$$\kappa \frac{\partial}{\partial x_i} \left( \frac{p}{\rho} \right).$$

Here

$$\kappa = \frac{k}{R} = \frac{\gamma}{\gamma - 1} \frac{\mu}{\text{Pr}}$$

where  $k$  is the conductivity,  $R$  is the gas constant, and  $\text{Pr}$  is the Prandtl number. The relationship between the conservative and primitive variations are defined by the expressions

$$\delta w = M \delta \tilde{w}, \quad \delta \tilde{w} = M^{-1} \delta w,$$

which make use of the transformation matrices  $M = \partial w / \partial \tilde{w}$  and  $M^{-1} = \partial \tilde{w} / \partial w$ . The conservative and primitive adjoint operators  $L$  and  $\tilde{L}$  corresponding to the variations  $\delta w$  and  $\delta \tilde{w}$  are then related by

$$\int_{\mathcal{D}} \delta w^T L \psi d\mathcal{D}_\xi = \int_{\mathcal{D}} \delta \tilde{w}^T \tilde{L} \psi d\mathcal{D}_\xi$$

with

$$\tilde{L} = M^T L,$$

where

$$M^T = \begin{bmatrix} 1 & u_1 & u_2 & u_3 & \frac{u_i u_i}{2} \\ 0 & \rho & 0 & 0 & \rho u_1 \\ 0 & 0 & \rho & 0 & \rho u_2 \\ 0 & 0 & 0 & \rho & \rho u_3 \\ 0 & 0 & 0 & 0 & \frac{1}{\gamma - 1} \end{bmatrix}.$$

The derivation of the viscous adjoint operator is provided in [204] with the simplification that variations in the transport coefficients are ignored. It is convenient to introduce the notation

$$\psi_{i+1} = \phi_i, \quad i = 1, 2, 3, \quad \psi_5 = \theta$$

in order to allow the use of the summation convention for repeated indices over the range 1–3. Then, collecting together the contributions from the momentum and energy equations, the viscous adjoint operator in primitive variables can finally be expressed as

$$\begin{aligned} (\tilde{L}\psi)_1 &= -\frac{p}{(\gamma - 1)\rho^2} \frac{\partial}{\partial \xi_i} \left( S_{ij} k \frac{\partial \theta}{\partial x_j} \right), \\ (\tilde{L}\psi)_{i+1} &= \frac{\partial}{\partial \xi_i} \left\{ S_{ij} \left[ \mu \left( \frac{\partial \phi_i}{\partial x_j} + \frac{\partial \phi_j}{\partial x_i} \right) + \lambda \delta_{ij} \frac{\partial \phi_k}{\partial x_k} \right] \right\} \\ &\quad + \frac{\partial}{\partial \xi_i} \left\{ S_{ij} \left[ \mu \left( u_i \frac{\partial \theta}{\partial x_j} + u_j \frac{\partial \theta}{\partial x_i} \right) + \lambda \delta_{ij} u_k \frac{\partial \theta}{\partial x_k} \right] \right\} \\ &\quad - \sigma_{ij} S_{ij} \frac{\partial \theta}{\partial x_i} \quad \text{for } i = 1, 2, 3, \\ (\tilde{L}\psi)_5 &= \frac{\rho}{(\gamma - 1)} \frac{\partial}{\partial \xi_i} \left( S_{ij} k \frac{\partial \theta}{\partial x_j} \right). \end{aligned}$$

The conservative viscous adjoint operator may then be obtained by the transformation

$$L = M^{-1T} \tilde{L}.$$

The final formula for the gradient depends on the way in which the boundary shape is parameterized as a function of the design variables, and the way in which the mesh is deformed as the boundary is modified. Using the relationship between the mesh deformation and the surface modification, the field integral is reduced to a surface integral by integrating along the coordinate lines emanating from the surface. Thus, expression (26) for  $\delta I$  is finally reduced to the form of Eq. (48)

$$\delta I = \int_{\mathcal{B}} \mathcal{G} \delta \mathcal{F} d\mathcal{B}_{\xi},$$

where  $\mathcal{F}$  represents the design variables, and  $\mathcal{G}$  is the gradient, which is a function defined over the boundary surface.

The boundary conditions satisfied by the flow equations restrict the form of the left hand side of the adjoint

boundary condition (60). Consequently, the boundary contribution to the cost function  $\mathcal{M}$  cannot be specified arbitrarily. Instead, it must be chosen from the class of functions which allow cancellation of all terms containing  $\delta w$  in the boundary integral of Eq. (58). On the other hand, there is no such restriction on the specification of the field contribution to the cost function  $\mathcal{P}$ , since these terms may always be absorbed into the adjoint field Eq. (59) as source terms.

The costate solution  $\psi$  is a legitimate test function for the weak form of the flow equations only if it is differentiable. In order to avoid discontinuities in the adjoint boundary condition which would be caused by the appearance of shock waves, the cost function for the target pressure  $p_d$  may be modified to the form

$$I = \frac{1}{2} \iint \left( \lambda_1 \mathcal{Z} + \lambda_2 \left( \frac{\partial \mathcal{Z}}{\partial \xi} \right)^2 \right) d\xi d\eta,$$

$$\lambda_1 \mathcal{Z} - \frac{\partial}{\partial \xi} \lambda_2 \frac{\partial \mathcal{Z}}{\partial \xi} = p - p_d.$$

Then

$$\begin{aligned} \delta I &= \iint \left( \lambda_1 \mathcal{Z} \delta \mathcal{Z} + \lambda_2 \frac{\partial \mathcal{Z}}{\partial \xi} \frac{\partial}{\partial \xi} \delta \mathcal{Z} \right) d\xi d\eta \\ &= \iint \mathcal{Z} \left( \lambda_1 - \frac{\partial}{\partial \xi} \lambda_2 \frac{\partial}{\partial \xi} \right) \delta \mathcal{Z} d\xi d\eta \\ &= \iint \mathcal{Z} \delta p d\xi d\eta \end{aligned}$$

and the smooth quantity  $\mathcal{Z}$  replaces  $p - p_d$  in the adjoint boundary condition. Smoothness should also be preserved in the redesigned shape. It is therefore crucially important to limit the shape modifications to smooth changes either by restricting the shape changes to combinations of smooth functions or by directly smoothing the changes.

#### 5.4. Optimization procedures

Two main search procedures have been used in our applications to date. The first is a simple descent method in which small steps are taken in the negative gradient direction. Let  $\mathcal{F}$  represent the design variable, and  $\mathcal{G}$  the gradient. Then the iteration

$$\delta \mathcal{F} = -\lambda \mathcal{G}$$

can be regarded as simulating the time dependent process

$$\frac{d\mathcal{F}}{dt} = -\mathcal{G},$$

where  $\lambda$  is the time step  $\Delta t$ . Let  $A$  be the Hessian matrix with elements

$$A_{ij} = \frac{\partial \mathcal{G}_i}{\partial \mathcal{F}_j} = \frac{\partial^2 I}{\partial \mathcal{F}_i \partial \mathcal{F}_j}.$$

Suppose that a locally minimum value of the cost function  $I^* = I(\mathcal{F}^*)$  is attained when  $\mathcal{F} = \mathcal{F}^*$ . Then the gradient  $\mathcal{G}^* = \mathcal{G}(\mathcal{F}^*)$  must be zero, while the Hessian matrix  $A^* = A(\mathcal{F}^*)$  must be positive definite. Since  $\mathcal{G}^*$  is zero, the cost function can be expanded as a Taylor series in the neighborhood of  $\mathcal{F}^*$  with the form

$$I(\mathcal{F}) = I^* + \frac{1}{2}(\mathcal{F} - \mathcal{F}^*)A(\mathcal{F} - \mathcal{F}^*) + \dots$$

Correspondingly,

$$\mathcal{G}(\mathcal{F}) = A(\mathcal{F} - \mathcal{F}^*) + \dots$$

As  $\mathcal{F}$  approaches  $\mathcal{F}^*$ , the leading terms become dominant. Then, setting  $\hat{\mathcal{F}} = (\mathcal{F} - \mathcal{F}^*)$ , the search process approximates

$$\frac{d\hat{\mathcal{F}}}{dt} = -A^*\hat{\mathcal{F}}.$$

Also, since  $A^*$  is positive definite it can be expanded as

$$A^* = RMR^T,$$

where  $M$  is a diagonal matrix containing the eigenvalues of  $A^*$ , and

$$RR^T = R^T R = I.$$

Setting

$$v = R^T \hat{\mathcal{F}},$$

the search process can be represented as

$$\frac{dv}{dt} = -Mv.$$

The stability region for the simple forward Euler stepping scheme is a unit circle centered at  $-1$  on the negative real axis. Thus for stability we must choose

$$\mu_{\max} \Delta t = \mu_{\max} \lambda < 2,$$

while the asymptotic decay rate, given by the smallest eigenvalue, is proportional to

$$e^{-\mu \min^t}.$$

In order to make sure that each new shape in the optimization sequence remains smooth, it proves essential to smooth the gradient and to replace  $\mathcal{G}$  by its smoothed value  $\bar{\mathcal{G}}$  in the descent process. This also acts as a preconditioner which allows the use of much larger steps. To apply smoothing in the  $\xi_1$  direction, for example, the smoothed gradient  $\bar{\mathcal{G}}$  may be calculated from a discrete approximation to

$$\bar{\mathcal{G}} - \frac{\partial}{\partial \xi_1} \varepsilon \frac{\partial}{\partial \xi_1} \bar{\mathcal{G}} = \mathcal{G},$$

where  $\varepsilon$  is the smoothing parameter. If one sets  $\delta \mathcal{F} = -\lambda \bar{\mathcal{G}}$ , then, assuming the modification is applied

on the surface  $\xi_2 = \text{constant}$ , the first order change in the cost function is

$$\begin{aligned} \delta I &= - \iint \mathcal{G} \delta \mathcal{F} d\xi_1 d\xi_3 \\ &= - \lambda \iint \left( \bar{\mathcal{G}} - \frac{\partial}{\partial \xi_1} \varepsilon \frac{\partial \bar{\mathcal{G}}}{\partial \xi_1} \right) \bar{\mathcal{G}} d\xi_1 d\xi_3 \\ &= - \lambda \iint \left( \bar{\mathcal{G}}^2 + \varepsilon \left( \frac{\partial \bar{\mathcal{G}}}{\partial \xi_1} \right)^2 \right) d\xi_1 d\xi_3 \\ &< 0, \end{aligned}$$

assuring an improvement if  $\lambda$  is sufficiently small and positive, unless the process has already reached a stationary point at which  $\mathcal{G} = 0$ .

It turns out that this approach is tolerant to the use of approximate values of the gradient, so that neither the flow solution nor the adjoint solution need be fully converged before making a shape change. This results in very large savings in the computational cost. For inviscid optimization it is necessary to use only 15 multigrid cycles for the flow solution and the adjoint solution in each design iteration. For viscous optimization, about 100 multigrid cycles are needed. This is partly because convergence of the lift coefficient is much slower, so about 20 iterations must be made before each adjustment of the angle of attack to force the target lift coefficient.

Our second main search procedure incorporates a quasi-Newton method for general constrained optimization. In this class of methods the step is defined as

$$\delta \mathcal{F} = -\lambda P \mathcal{G},$$

here  $P$  is a preconditioner for the search. An ideal choice is  $P = A^{*-1}$ , so that the corresponding time dependent process reduces to

$$\frac{d\hat{\mathcal{F}}}{dt} = -\hat{\mathcal{F}},$$

for which all the eigenvalues are equal to unity, and  $\hat{\mathcal{F}}$  is reduced to zero in one time step by the choice  $\Delta t = 1$  if the Hessian,  $A$ , is constant. The full Newton method takes  $P = A^{-1}$ , requiring the evaluation of the Hessian matrix,  $A$ , at each step. It corresponds to the use of the Newton–Raphson method to solve the non-linear equation  $\mathcal{G} = 0$ . Quasi-Newton methods estimate  $A^*$  from the change in the gradient during the search process. This requires accurate estimates of the gradient at each time step. In order to obtain these, both the flow solution and the adjoint equation must be fully converged. Most quasi-Newton methods also require a line search in each search direction, for which the flow equations and cost function must be accurately evaluated several times. Since the Hessian can only be completely estimated after as many steps as there are design variables, it pays to reduce the number of design variables with this approach

by representing the geometry as a superposition of appropriately chosen shape functions. The Hicks–Henne bump functions [205] have proved effective in many applications. Because those functions are smooth they also serve the purpose of preserving the smoothness of the shape modifications, which is essential for any acceptable design.

In the applications to complex configurations presented below the optimization was carried out using the existing, well validated software NPSOL. This software, which implements a quasi-Newton method for optimization with both linear and nonlinear constraints, has proved very reliable but is generally more expensive than the simple search method with smoothing.

### 5.5. Industrial experience and results of optimization

The methods described in this paper have been quite thoroughly tested in industrial applications in which they were used as a tool for aerodynamic design. They have proved useful both in inverse mode to find shapes that would produce desired pressure distributions, and for direct minimization of the drag. They have been applied both to well understood configurations that have gradually evolved through incremental improvements guided by wind tunnel tests and computational simulation, and to new concepts for which there is a limited knowledge base. In either case they have enabled engineers to produce improved designs.

Substantial improvements are usually obtained with 20–200 design cycles, depending on the difficulty of the case. One concern is the possibility of getting trapped in a local minimum. In practice, this has not proved to be a source of difficulty. In inverse mode, it often proves possible to come very close to realizing the target pressure distribution, thus effectively demonstrating convergence. In drag minimization, the result of the optimization is usually a shock-free wing. If one considers drag minimization of airfoils in two-dimensional inviscid transonic flow, it can be seen that every shock-free airfoil produces zero drag, and thus optimization based solely on drag has a highly nonunique solution. Different shock-free airfoils can be obtained by starting from different initial profiles. One may also influence the character of the final design by blending a target pressure distribution with the drag in the definition of the cost function.

Similar considerations apply to three-dimensional wing design in viscous transonic flow. Since the vortex drag can be reduced simply by reducing the lift, the lift coefficient must be fixed for a meaningful drag minimization. A typical wing of a transport aircraft is designed for a lift coefficient in the range of 0.4 to 0.6. The total wing drag may be broken down into vortex drag, drag due to viscous effects, and shock drag. The vortex drag coefficient is typically in the range of 0.0100 (100 counts),

while the friction drag coefficient is in the range of 45 counts, and the shock drag at a Mach number just before the onset of severe drag rise is of the order of 15 counts. With a fixed span, typically dictated by structural limits or a constraint imposed by airport gates, the vortex drag is entirely a function of span loading, and is minimized by an elliptic loading unless winglets are added. Transport aircraft usually have highly tapered wings with very large root chords to accommodate retraction of the undercarriage. An elliptic loading may lead to excessively large section lift coefficients on the outboard wing, leading to premature shock stall or buffet when the load is increased. The structure weight is also reduced by a more inboard loading which reduces the root bending moment. Thus the choice of span loading is influenced by other considerations. The skin friction of transport aircraft is typically very close to flat plate skin friction in turbulent flow, and is very insensitive to section variations. An exception to this is the case of smaller executive jet aircraft, for which the Reynolds number may be small enough to allow a significant run of laminar flow if the suction peak of the pressure distribution is moved back on the section. This leaves the shock drag as the primary target for wing section optimization. This is reduced to zero if the wing is shock-free, leaving no room for further improvement. Thus the attainment of a shock-free flow is a demonstration of a successful drag minimization. In practice range is maximized by maximizing  $ML/D$ , and this is likely to be increased by increasing the lift coefficient to the point where a weak shock appears. One may also use optimization to find the maximum Mach number at which the shock drag can be eliminated or significantly reduced for a wing with a given sweepback angle and thickness. Alternatively, one may try to find the largest wing thickness or the minimum sweepback angle for which the shock drag can be eliminated at a given Mach number. This can yield both savings in structure weight and increased fuel volume. If there is no fixed limit for the wing span, such as a gate constraint, increased thickness can be used to allow an increase in aspect ratio for a wing of equal weight, in turn leading to a reduction in vortex drag. Since the vortex drag is usually the largest component of the total wing drag, this is probably the most effective design strategy, and it may pay to increase the wing thickness to the point where the optimized section produces a weak shock wave rather than a shock-free flow [206].

The first major industrial application of an adjoint based aerodynamic optimization method was the wing design of the Beech Premier [207] in 1995. The method was successfully used in inverse mode as a tool to obtain pressure distributions favorable to the maintenance of natural laminar flow over a range of cruise Mach numbers. Wing contours were obtained which yielded the desired pressure distribution in the presence of closely

coupled engine nacelles on the fuselage above the wing trailing edge.

During 1996 some preliminary studies indicated that the wings of both the McDonnell Douglas MD-11 and the Boeing 747-200 could be made shock-free in a representative cruise condition by using very small shape modifications, with consequent drag savings which could amount to several percent of the total drag. This led to a decision to evaluate adjoint-based design methods in the design of the McDonnell Douglas MDXX during the summer and fall of 1996. In initial studies wing redesigns were carried out for inviscid transonic flow modeled by the Euler equations. A redesign to minimize the drag at a specified lift and Mach number required about 40 design cycles, which could be completed overnight on a workstation.

Three main lessons were drawn from these initial studies: (i) the fuselage effect is too large to be ignored and must be included in the optimization, (ii) single-point designs could be too sensitive to small variations in the flight condition, typically producing a shock-free flow at the design point with a tendency to break up into a severe double shock pattern below the design point, and (iii) the shape changes necessary to optimize a wing in transonic flow are smaller than the boundary layer displacement thickness, with the consequence that viscous effects must be included in the final design.

In order to meet the first two of these considerations, the second phase of the study was concentrated on the optimization of wing-body combinations with multiple design points. These were still performed with inviscid flow to reduce computational cost and allow for fast turnaround. It was found that comparatively insensitive designs could be obtained by minimizing the drag at a fixed Mach number for three fairly closely spaced lift coefficients such as 0.5, 0.525, and 0.55, or alternatively three nearby Mach numbers with a fixed lift coefficient (see Figs. 21–24).

The third phase of the project was focused on the design with viscous effects using as a starting point wings which resulted from multipoint inviscid optimization. While the full viscous adjoint method was still under development, it was found that useful improvements could be realized, particularly in inverse mode, using the inviscid result to provide the target pressure, by coupling an inviscid adjoint solver to a viscous flow solver. Computer costs are many times larger, both because finer meshes are needed to resolve the boundary layer, and because more iterations are needed in the flow and adjoint solutions. In order to force the specified lift coefficient the number of iterations in each flow solution had to be increased from 15 to 100. To achieve overnight turnaround a fully parallel implementation of the software had to be developed. Finally, it was found that in order to

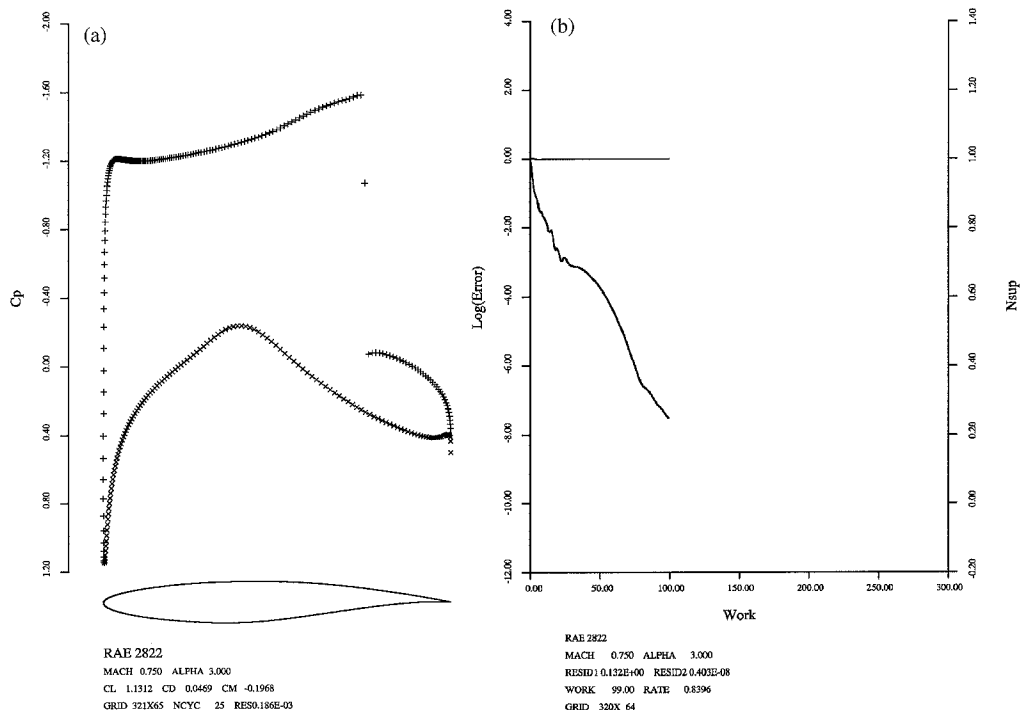


Fig. 21. RAE-2822 Airfoil at Mach 0.750 and  $\alpha = 3.0^\circ$  H-CUSP scheme. a:  $C_p$  after 25 Cycles.  $C_l = 1.1312$ ,  $C_d = 0.0469$ . b: Convergence.



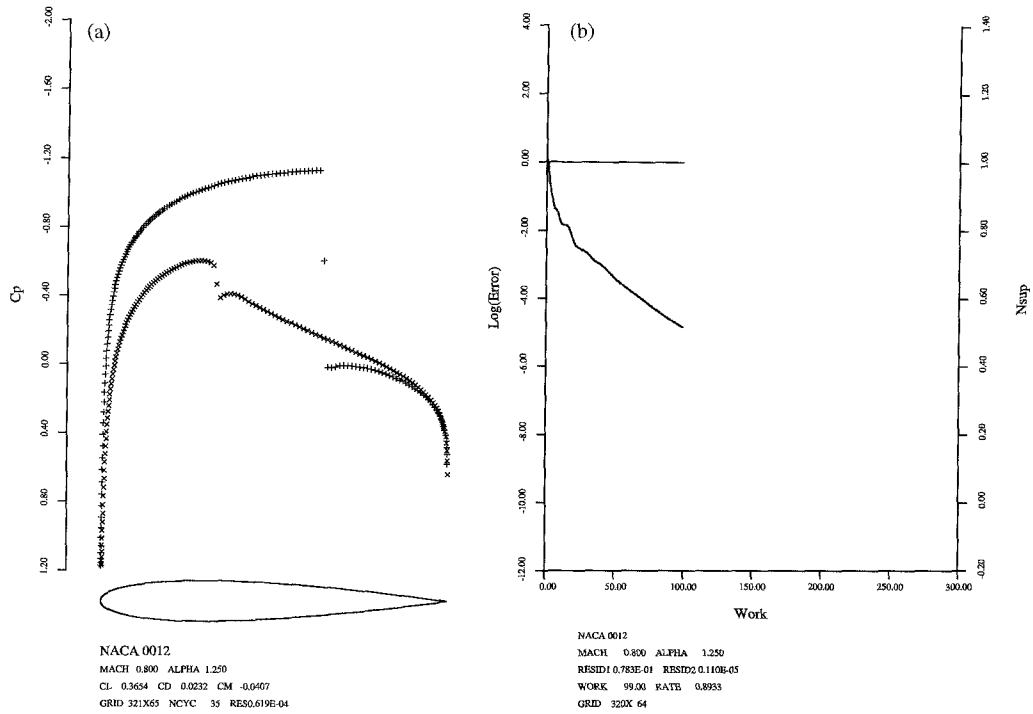


Fig. 22. NACA-0012 Airfoil at Mach 0.800 and  $\alpha = 1.25^\circ$  H-CUSP scheme. a:  $C_p$  after 35 Cycles.  $C_l = 0.3654$ ,  $C_d = 0.0232$ . b: Convergence.

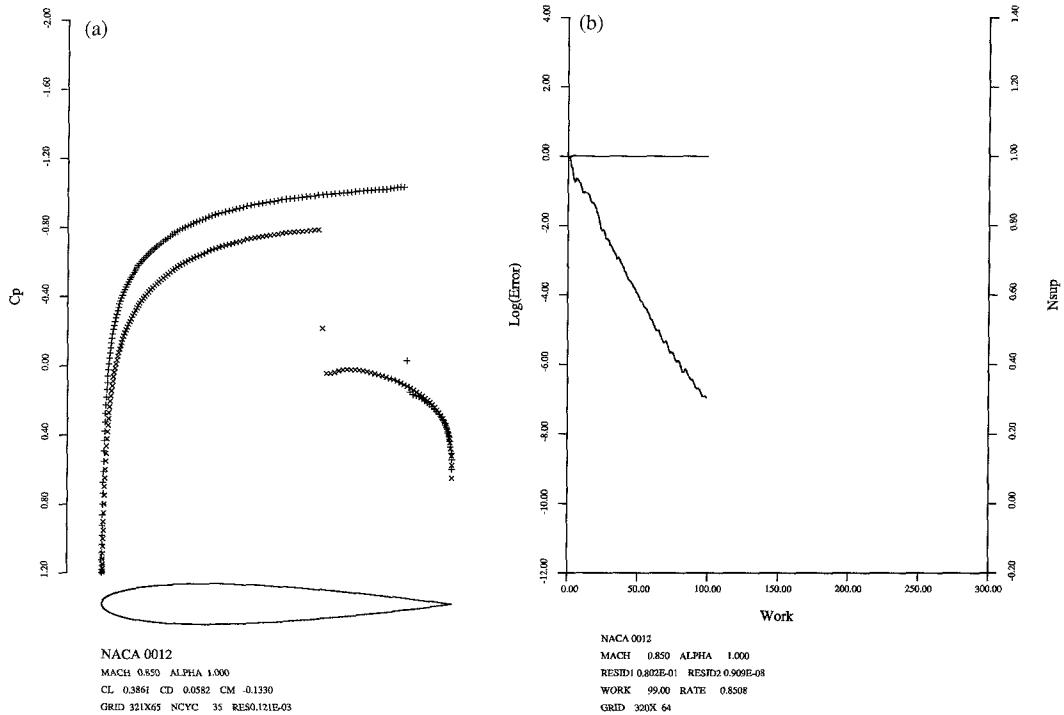


Fig. 23. NACA-0012 Airfoil at Mach 0.850 and  $\alpha = 1.0^\circ$  H-CUSP scheme. a:  $C_p$  after 35 Cycles.  $C_l = 0.3861$ ,  $C_d = 0.0582$ . b: Convergence.

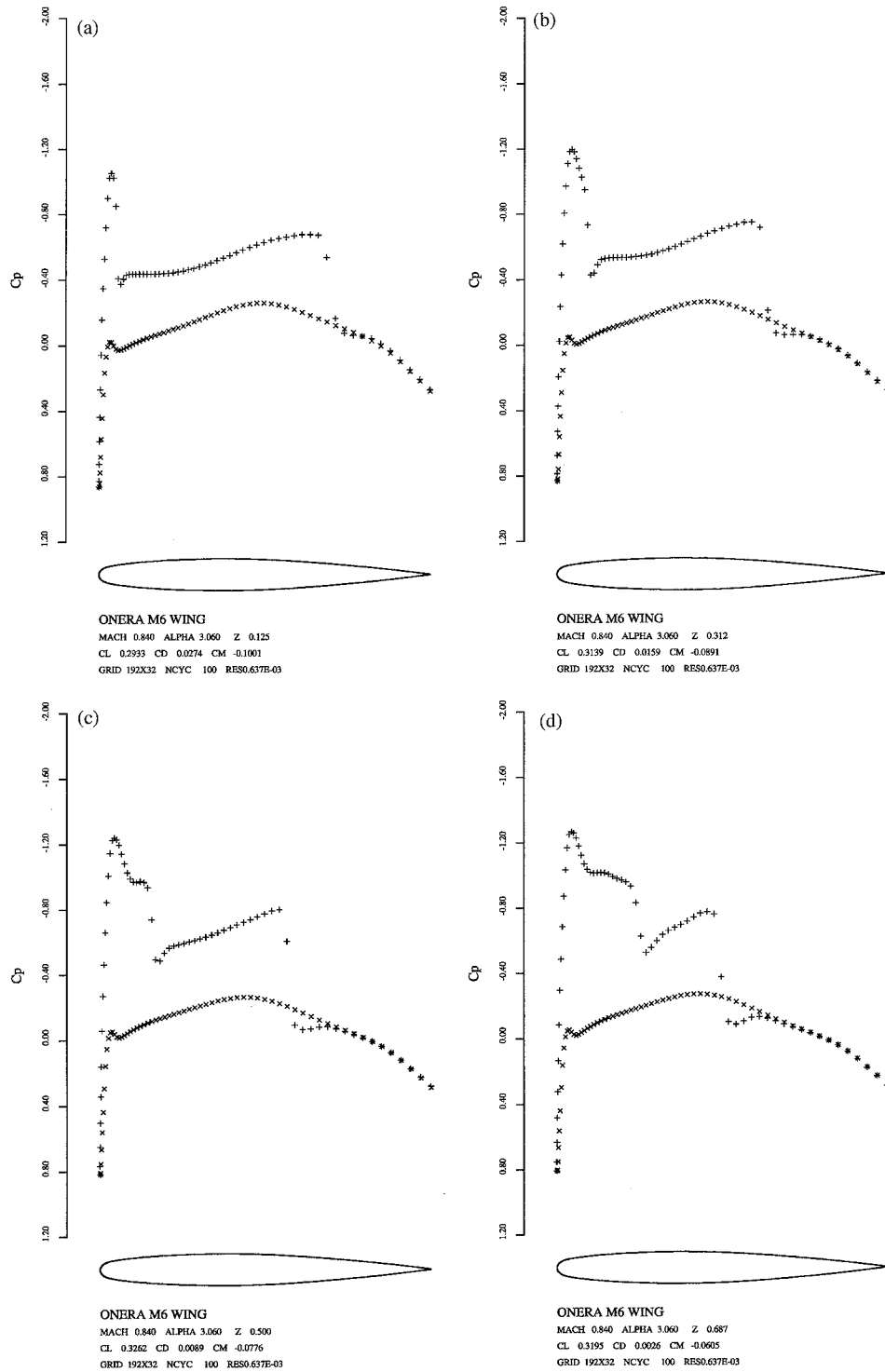


Fig. 24. Onera M6 Wing. Mach 0.840, angle of attack 3.06°, 192 × 32 × 48 Mesh.  $C_L = 0.3041$ ,  $C_D = 0.0131$ . H-CUSP scheme. a: 12.50% Span.  $C_l = 0.2933$ ,  $C_d = 0.0274$ . b: 31.25% Span.  $C_l = 0.3139$ ,  $C_d = 0.0159$ . c: 50.00% Span.  $C_l = 0.3262$ ,  $C_d = 0.0089$ . d: 68.75% Span.  $C_l = 0.3195$ ,  $C_d = 0.0026$ .

produce sufficiently accurate results, the number of mesh points had to be increased to about 1.8 million. In the final phase of this project it was planned to carry out a propulsion integration study using the multiblock versions of the software. This study was not completed due to the cancellation of the entire MDXX project.

During the summer of 1997, adjoint methods were again used to assist the McDonnell Douglas Blended Wing-Body project. By this time the viscous adjoint method was well developed, and it was found that it was needed to achieve truly smooth shock-free solutions. With an inviscid adjoint solver coupled to a viscous flow solver some improvements could be made, but the shocks could not be entirely eliminated.

The next subsection shows a wing design using the full viscous adjoint method in its current form, implemented in the computer program SYN107. The remaining subsections present results of optimizations for complete configurations in inviscid transonic and supersonic flow using the multiblock parallel design program, SYN107-MB.

#### 5.5.1. Transonic viscous wing-body design

A typical result of drag minimization in transonic viscous flow is presented below. This calculation is a re-design of a wing using the viscous adjoint optimization method with a Baldwin-Lomax turbulence model. The initial wing is similar to one produced during the MDXX design studies. Figs. 25–27 show the result of the wing-body redesign on a C-H mesh with  $288 \times 96 \times 64$  cells. The wing has sweep back of about  $38^\circ$  at the  $1/4$  chord.

A total of 44 iterations of the viscous optimization procedure resulted in a shock-free wing at a cruise design point of Mach 0.86, with a lift coefficient of 0.61 for the wing-body combination at a Reynolds number of 101 million based on the root chord. Using 48 processors of an SGI Origin2000 parallel computer, each design iteration takes about 22 min so that overnight turnaround for such a calculation is possible. Fig. 25 compares the pressure distribution of the final design with that of the initial wing. The final wing is quite thick, with a thickness to chord ratio of about 14% at the root and 9% at the tip. The optimization was performed with a constraint that the section modifications were not allowed to decrease the thickness anywhere. The design offers excellent performance at the nominal cruise point. A drag reduction of 2.2 counts was achieved from the initial wing which had itself been derived by inviscid optimization. Figs. 26 and 27 show the results of a Mach number sweep to determine the drag rise. The drag coefficients shown in the figures represent the total wing drag including shock, vortex, and skin friction contributions. It can be seen that a double shock pattern forms below the design point, while there is actually a slight increase in the drag coefficient at Mach 0.85. The tendency to produce double shocks below the design point is typical of supercritical wings. This wing has a low drag coefficient, however, over a wide range of conditions. Above the design point a single shock forms and strengthens as the Mach number increases, a behavior typical in transonic flow (see Fig. 28).

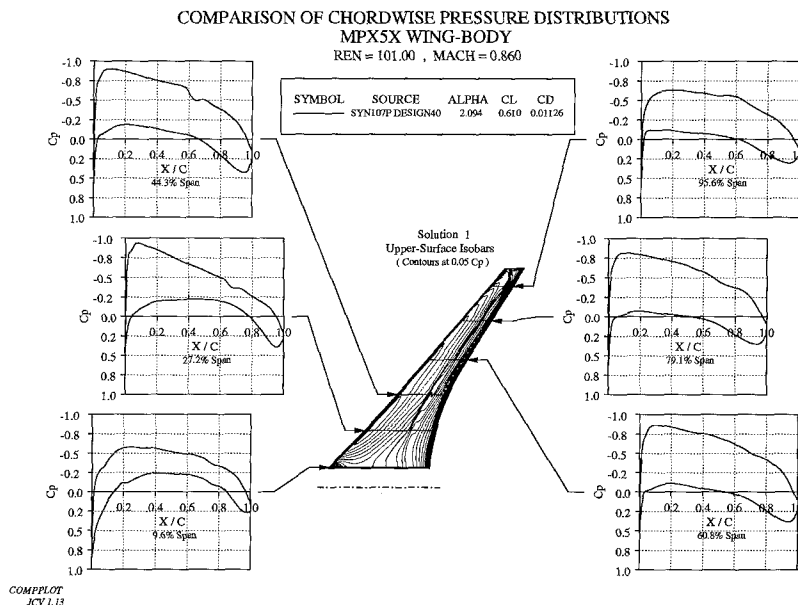


Fig. 25. Pressure distribution of the MPX5X at its design point.

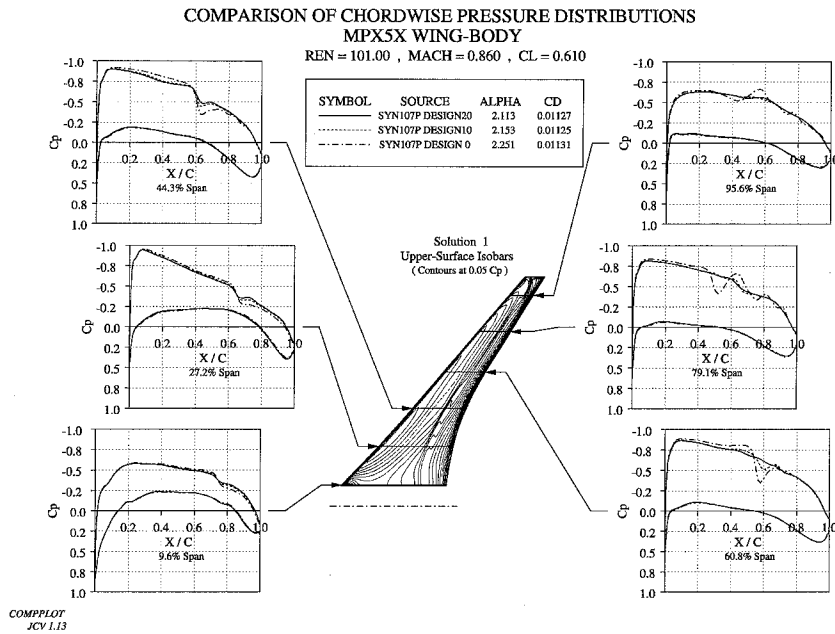


Fig. 26. Optimization sequence in the design of the MPX5X.

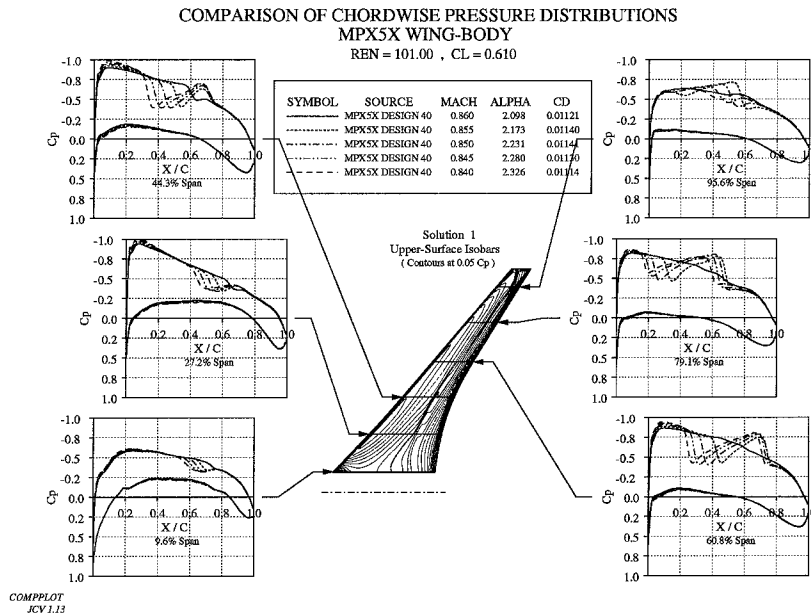


Fig. 27. Off design performance of the MPX5X below the design point.

### 5.5.2. Transonic multipoint constrained aircraft design

As a first example of the automatic design capability for complex configurations, a typical business jet configuration is chosen for a multipoint drag minimization run. The objective of the design is to alter the geometry of the

wing in order to minimize the configuration inviscid drag at three different flight conditions simultaneously. Realistic geometric spar thickness constraints are enforced. The geometry chosen for this analysis is a full configuration business jet composed of wing, fuselage, pylon, nacelle,

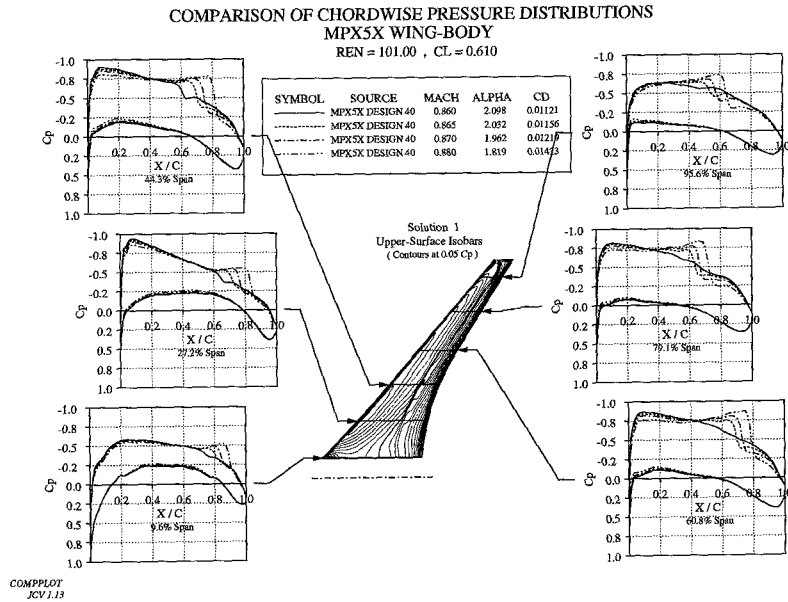


Fig. 28. Off design performance of the MPX5X above the design point.

and empennage. The inviscid multiblock mesh around this configuration follows a general C–O topology with special blocking to capture the geometric details of the nacelles, pylons and empennage. A total of 240 point-to-point matched blocks with 4,157,440 cells (including halos) are used to grid the complete configuration. This mesh allows the use of 4 multigrid levels obtained through recursive coarsening of the initial fine mesh. The upstream, downstream, upper and lower far field boundaries are located at an approximate distance of 15 wing semispans, while the far field boundary beyond the wing tip is located at a distance approximately equal to 5 semi-spans. An engineering-accuracy solution (with a decrease of 4 orders of magnitude in the average density residual) can be obtained in 100 multigrid cycles. This kind of solution can be routinely accomplished in under 20 min of wall clock time using 32 processors of an SGI Origin2000 computer.

The initial configuration was designed for Mach = 0.8 and  $C_L = 0.3$ . The three operating points chosen for this design are Mach = 0.81 with  $C_L = 0.35$ , Mach = 0.82 with  $C_L = 0.30$ , and Mach = 0.83 with  $C_L = 0.25$ . For each of the design points, both Mach number and lift coefficient are held fixed. In order to demonstrate the advantage of a multipoint design approach, the final solution at the middle design point will be compared with a single-point design at the same conditions. As the geometry of the wing is modified, the design algorithm computes new wing-fuselage intersections. The wing component is made up of six airfoil defining sections. Eighteen Hicks–Henne design variables are applied to

five of these sections for a total of 90 design variables. The sixth section at the symmetry plane is not modified. Spar thickness constraints were also enforced on each defining station at the  $x/c = 0.2$  and  $0.8$  locations. Maximum thickness was forced to be preserved at  $x/c = 0.4$  for all six defining sections. To ensure an adequate included angle at the trailing edge, each section was also constrained to preserve thickness at  $x/c = 0.95$ . Finally, to preserve leading edge bluntness, the upper surface of each section was forced to maintain its height above the camber line at  $x/c = 0.02$ . Combined, a total of 30 linear geometric constraints were imposed on the configuration.

Significant improvements were obtained with 5 design iterations using NPSOL. Table 4 summarizes the drag reductions that were obtained with a single-point design optimized at Mach 0.82, and a three-point design simultaneously optimized at Mach 0.81, Mach 0.82, and Mach 0.83. The  $C_D$  values have been normalized by the drag of the original configuration at Mach 0.82. Interestingly, the upper surface shapes for both final designs are very similar. However, in the case of the single-point design, a strong lower surface shock appears at the Mach = 0.83,  $C_L = 0.25$  design point. The three-point design is able to suppress the formation of this lower surface shock and achieves a 9 count drag benefit over the single-point design at this condition. However, it has a 1 count penalty at the single-point design condition. The three-point design features a weak single shock for one of the three design points and a very weak double shock at another design point. Fig. 29 shows the surface of the

Table 4  
Drag reduction for single and multipoint designs

Design Mach	Conditions $C_L$	Initial relative $C_D$	Single-point design relative $C_D$	Three-point design relative $C_D$
0.81	0.35	1.00257	0.85003	0.85413
0.82	0.30	1.00000	0.77350	0.77915
0.83	0.25	1.08731	0.81407	0.76836

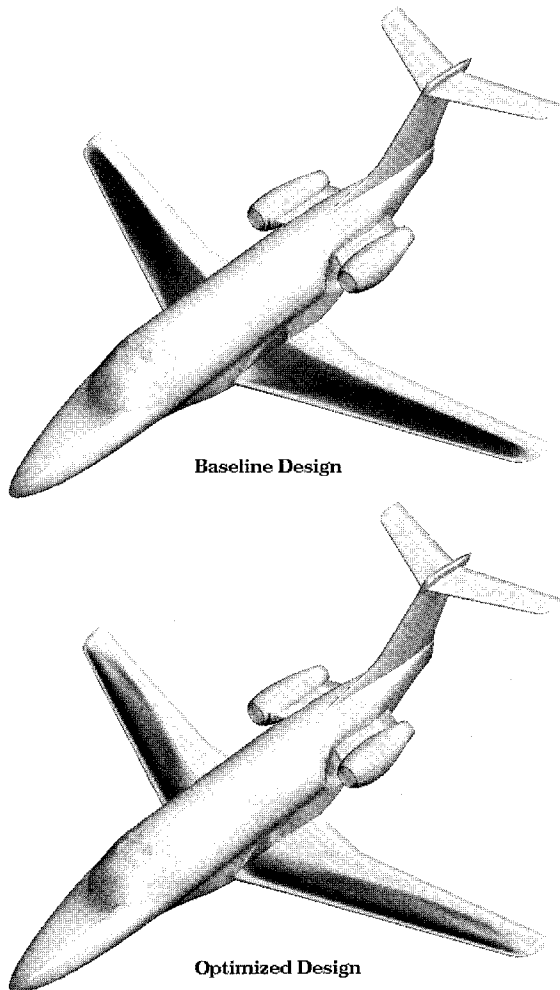


Fig. 29. Geometry surface colored by local  $C_p$  before and after redesign.

configuration colored by the local coefficient of pressure,  $C_p$ , before and after redesign for the middle design point. One can clearly observe that the strength of the shock wave on the upper surface of the configuration has been considerably reduced.

### 5.5.3. Supersonic constrained aircraft design

For supersonic design, provided that turbulent flow is assumed over the entire configuration, the inviscid Euler equations suffice for aerodynamic design since the pressure drag is not greatly affected by the inclusion of viscous effects. Moreover, flat plate skin friction estimates of viscous drag are often very good approximations. In this study, the generic supersonic transport configuration used in reference [208] is revisited.

The baseline supersonic transport configuration was sized to accommodate 300 passengers with a gross take-off weight of 750,000 lbs. The supersonic cruise point is Mach 2.2 with a  $C_L$  of 0.105. Fig. 30 shows that the planform is a cranked-delta configuration with a break in the leading edge sweep. The inboard leading edge sweep is  $68.5^\circ$  while the outboard is  $49.5^\circ$ . Since the Mach angle at  $M = 2.2$  is  $63^\circ$  it is clear that some leading edge bluntness may be used inboard without a significant wave drag penalty. Blunt leading edge airfoils were created with thickness ranging from 4% at the root to 2.5% at the leading edge break point. These symmetric airfoils were chosen to accommodate thick spars at roughly the 5% and 80% chord locations over the span up to the leading edge break. Outboard of the leading edge break where the wing sweep is ahead of the Mach cone, a sharp leading edge was used to avoid unnecessary wave drag. The airfoils were chosen to be symmetric, biconvex shapes modified to have a region of constant thickness over the mid-chord. The four-engine configuration features axisymmetric nacelles tucked close to the wing lower surface. This layout favors reduced wave drag by minimizing the exposed boundary layer diverter area. However, in practice, it may be problematic because of the channel flows occurring in the juncture region of the diverter, wing, and nacelle at the wing trailing edge.

The computational mesh on which the design is run has 180 blocks and 1,500,000 mesh cells (including halos), while the underlying geometry entities define the wing with 16 sectional cuts and the body with 200 sectional cuts. In this case, where we hope to optimize the shape of the wing, care must be taken to ensure that the nacelles remain properly attached with diverter heights being maintained.

The objective of the design is to reduce the total drag of the configuration at a single design point (Mach = 2.2,

$C_L = 0.105$ ) by modifying the wing shape. Just as in the transonic case, 18 design variables of the Hicks–Henne type are chosen for each wing defining section. Similarly, instead of applying them to all 16 sections, they are applied to 8 of the sections and then lofted linearly to the neighboring sections. Spar thickness constraints are imposed for all wing defining sections at  $x/c = 0.05$  and  $0.8$ . An additional maximum thickness constraint is specified along the span at  $x/c = 0.5$ . A final thickness constraint is enforced at  $x/c = 0.95$  to ensure a reasonable trailing edge included angle. An iso- $C_p$  representation of the initial and final designs is depicted in Fig. 30 for both the upper and lower surfaces.

It is noted that the strong oblique shock evident near the leading edge of the upper surface on the initial configuration is largely eliminated in the final design after 5 NPSOL design iterations. Also, it is seen that the upper

surface pressure distribution in the vicinity of the nacelles has formed an unexpected pattern. However, recalling that thickness constraints abound in this design, these upper surface pressure patterns are assumed to be the result of sculpting of the lower surface near the nacelles which affects the upper surface shape via the thickness constraints. For the lower surface, the leading edge has developed a suction region while the shocks and expansions around the nacelles have been somewhat reduced. Fig. 31 shows the pressure coefficients and (scaled) airfoil sections for four sectional cuts along the wing. These cuts further demonstrate the removal of the oblique shock on the upper surface and the addition of a suction region on the leading edge of the lower surface. The airfoil sections have been scaled by a factor of 2 so that shape changes may be seen more easily. Most notably, the section at 38.7% span has had the lower surface drastically

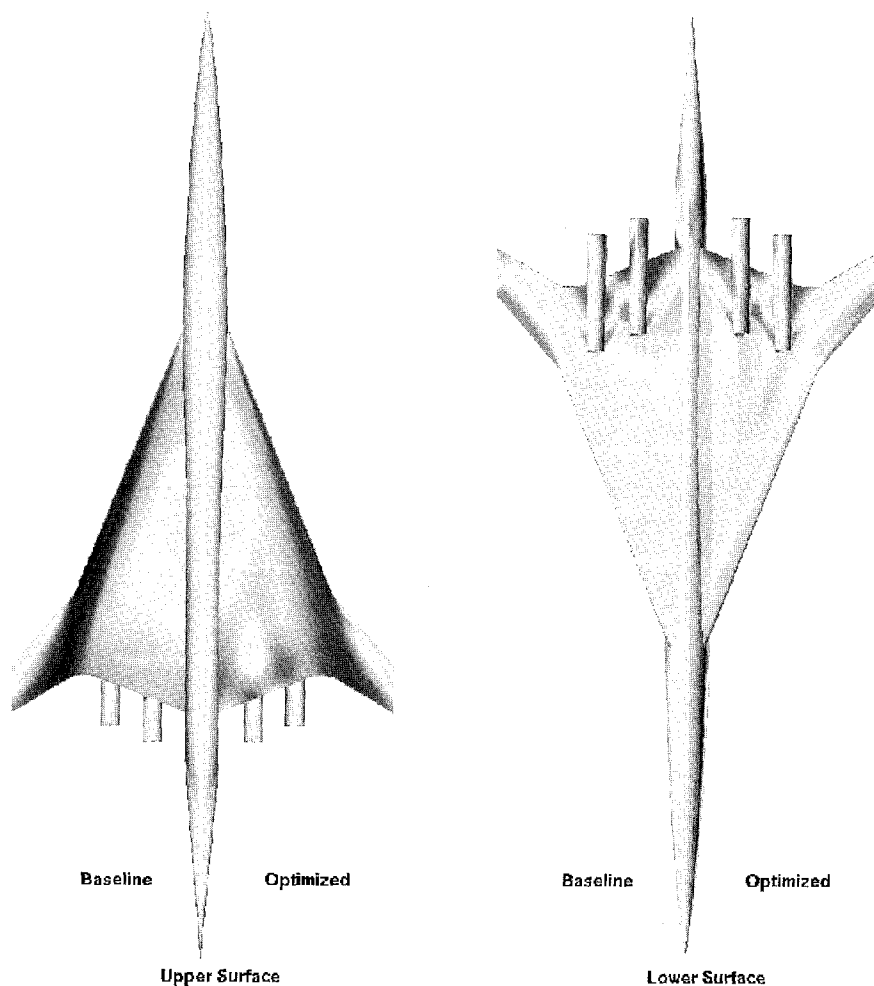


Fig. 30. Supersonic transport configuration. Iso- $C_p$  contours on upper and lower surfaces. Baseline and optimized designs.  $M = 2.2$ ,  $C_L = 0.105$ .

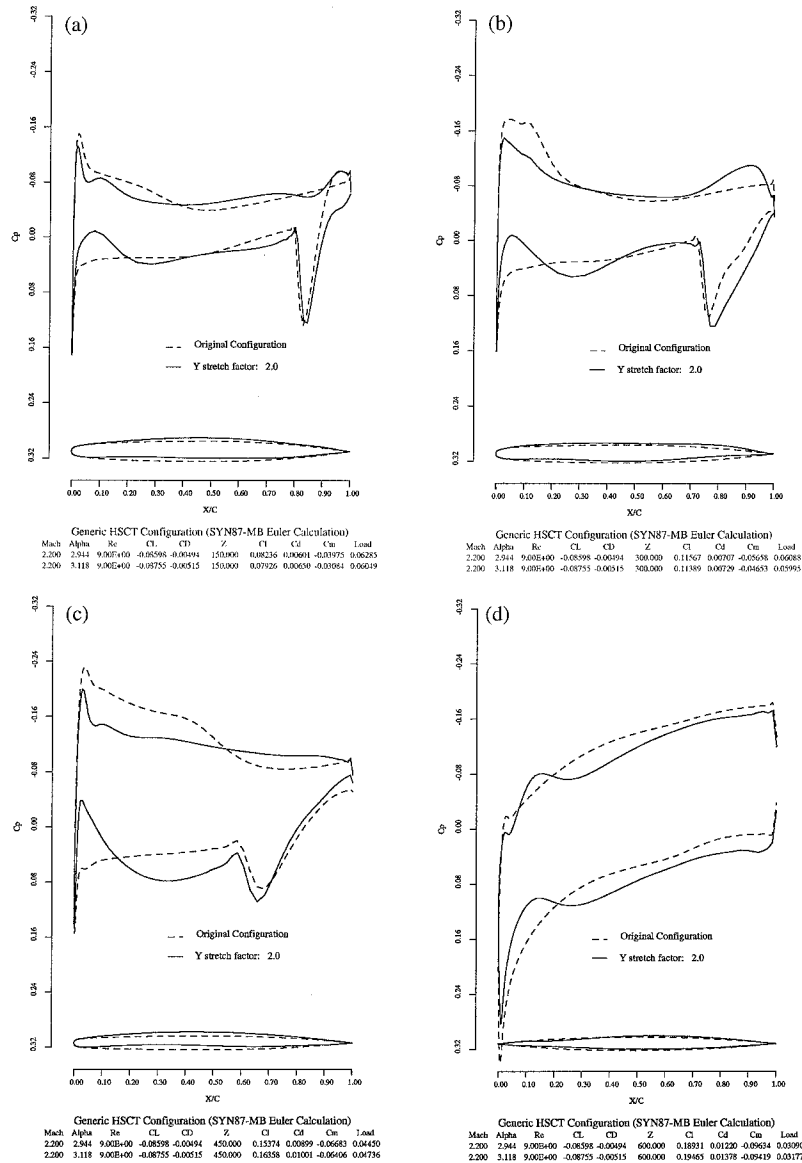


Fig. 31. Supersonic transport configuration. Drag minimization at fixed lift.  $M = 2.20$ ,  $C_L = 0.105$  144 Hicks-Henne variables. Spar constraints active, (---) initial pressures, (—) pressures after 5 design cycles. a: span station  $z = 0.194$  b: span station  $z = 0.387$  c: span station  $z = 0.581$  d: span station  $z = 0.775$ .

modified such that a large region of the aft airfoil has a forward-facing portion near where the pressure spike from the nacelle shock impinges on the surface. The final overall pressure drag was reduced by 8%, from  $C_D = 0.0088$  to  $0.0081$ .

## 6. Outlook and conclusions

Better algorithms and better computer hardware have contributed about equally to the progress of computa-

tional science in the last two decades. In 1970 the Control Data 6600 represented the state of the art in computer hardware with a speed of about  $10^6$  operations per second (one megaflop), while in 1990 the 8 processor Cray YMP offered a performance of about  $10^9$  operations per second (one gigaflop). Correspondingly, steady-state Euler calculations which required 5000–10,000 steps prior to 1980 could be performed in 10–50 steps in 1990 using multigrid acceleration. With the advent of massively parallel computers it appears that the progress of



computer hardware may even accelerate. Teraflop machines offering further improvement by a factor of 1000 are likely to be available within a few years. Parallel architectures will force a reappraisal of existing algorithms, and their effective utilization will require the extensive development of new parallel software.

In parallel with the transition to more sophisticated algorithms, the present challenge is to extend the effective use of CFD to more complex applications. A key problem is the treatment of multiple space and time scales. These arise not only in turbulent flows, but also in many other situations such as chemically reacting flows, combustion, flame fronts and plasma dynamics. Another challenge is presented by problems with moving boundaries. Examples include helicopter rotors, and rotor-stator interaction in turbomachinery. It can be anticipated that interdisciplinary applications in which CFD is coupled with the computational analysis of other properties of the design will play an increasingly important role. These applications may include structural, thermal and electromagnetic analysis. Aeroelastic problems and integrated control system and aerodynamic design are likely target areas. The development of improved algorithms continues to be important in providing the basic building blocks for numerical simulation. In particular, better error estimation procedures must be developed and incorporated in the simulation software to provide error control. The basic simulation software is only one of the needed ingredients, however. The flow solver must be embedded in a user-friendly system for geometry modeling, output analysis, and data management that will provide a complete numerical design environment. These are the ingredients which are needed for the full realization of the concept of a numerical wind tunnel. Figs. 18 and 19 illustrate the way in which a numerical wind tunnel might evolve from current techniques, which involve massive data handling tasks, to a fully integrated design environment.

As more powerful computational resources become available, computational simulation is in the process of becoming the principal tool of the aerodynamic design process because of the flexibility it provides for the rapid and comparatively inexpensive evaluation of alternative designs, and because it can be integrated in a numerical design environment providing for both multi-disciplinary analysis and multi-disciplinary optimization.

### Acknowledgements

The research described in this paper has benefited greatly from the generous support of the Air Force Office of Scientific Research under grant AF F49620-98-1-022. I am grateful to Juan J. Alonso and Luigi Martinelli for their assistance in assembling the text of this document.

### References

- [1] Hess JL, Smith AMO. Calculation of non-lifting potential flow about arbitrary three-dimensional bodies. Douglas Aircraft Report ES 40622, 1962.
- [2] Rubbert PE, Saaris GR. A general three-dimensional potential flow method applied to V/STOL aerodynamics. SAE Paper 680304, 1968.
- [3] Woodward F. An improved method for the aerodynamic analysis of wing-body-tail configurations in subsonic and supersonic flow, Part 1—theory and application. NASA CR 2228 Pt. 1, May 1973.
- [4] Murman EM, Cole JD. Calculation of plane steady transonic flows. AIAA J 1971;9:114–21.
- [5] Murman EM. Analysis of embedded shock waves calculated by relaxation methods. AIAA J 1974;12: 626–33.
- [6] Jameson A. Iterative solution of transonic flows over airfoils and wings, including flows at Mach 1. Commun Pure Appl Math 1974;27:283–309.
- [7] Jameson A. Transonic potential flow calculations in conservation form. Proceedings of the AIAA Second Computational Fluid Dynamics Conference, Hartford, 1975. p. 148–61.
- [8] Eberle A. A finite volume method for calculating transonic potential flow around wings from the minimum pressure integral. NASA TM 75324, 1978 (Translated from MBB UFE 1407(0)).
- [9] Hafez M, South JC, Murman EM. Artificial compressibility method for numerical solutions of the transonic full potential equation. AIAA J 1979;17:838–44.
- [10] Bauer F, Garabedian P, Korn D, Jameson A. Supercritical wing sections II. New York: Springer, 1975.
- [11] Oden JT, Demkowicz L, Liszka T, Rachowicz W. *h-p* adaptive finite element methods for compressible and incompressible flows. In: Veneri SL, Noor AK, editors. Proceedings of the Symposium on Computational Technology on Flight Vehicles, Washington, DC, Oxford: Pergamon, November 1990. p. 523–34.
- [12] Bristeau MO, Glowinski R, Periaux J, Perrier P, Pironneau O, Poirier C. On the numerical solution of nonlinear problems in fluid dynamics by least squares and finite element methods (II), application to transonic flow simulations. Comput Methods Appl Mech Eng 1985;51:363–94.
- [13] Lohner R, Morgan K, Peraire J, Zienkiewicz OC. Finite element methods for high speed flows. AIAA Paper 85-1531, AIAA 7th Computational Fluid Dynamics Conference, Cincinnati, OH, 1985.
- [14] Jameson A, Baker TJ, Weatherill NP. Calculation of inviscid transonic flow over a complete aircraft. AIAA Paper 86-0103, AIAA 24th Aerospace Sciences Meeting, Reno, NV, January 1986.
- [15] Jameson A, Baker TJ. Improvements to the aircraft Euler method. AIAA Paper 87-0452, AIAA 25th Aerospace Sciences Meeting, Reno, NV, January 1987.
- [16] Stoufflet B, Periaux J, Fezoui F, Dervieux A. Numerical simulation of 3-D hypersonic Euler flows around space vehicles using adapted finite elements. AIAA Paper 87-0560. AIAA 25th Aerospace Sciences Meeting, Reno, NV, January 1987.

- [17] Batina JT. Implicit flux-split Euler schemes for unsteady aerodynamic analysis involving unstructured dynamic meshes. AIAA Paper 90-0936, April 1990.
- [18] Mavriplis DJ, Jameson A. Multigrid solution of the Navier–Stokes equations on triangular meshes. AIAA J 1990;28(8):1415–25.
- [19] Mavriplis DJ, Martinelli L. Multigrid solution of compressible turbulent flow on unstructured meshes using a two-equation model. AIAA Paper 91-0237, AIAA 29th Aerospace Sciences Meeting, Reno, NV, January 1991.
- [20] Barth TJ. Aspects of unstructured grids and finite volume solvers for the Euler and Navier–Stokes equations. von Karman Institute for Fluid Dynamics Lecture Series Notes 1994-05, Brussels, 1994.
- [21] Martinelli L, Jameson A. Validation of a multigrid method for the Reynolds averaged equations. AIAA Paper 88-0414, 1988.
- [22] Jou WH. Boeing Memorandum, AERO-B113B-L92-018, September 1992. To Joseph Shang.
- [23] Spalart PR, Jou WH, Strelets M, Allmaras SR. Comments on the feasibility of LES for wings, and on a hybrid RANS/LES approach. In: Liu C, Liu Z, Sakell L, editors. Advances in DNS and LES, Greydon Press, 1997.
- [24] Ha MH. The impact of turbulence modelling on the numerical prediction of flows. In: Napolitano M, Solbetta F, editors. Proceedings of the 13th International Conference on Numerical Methods in Fluid Dynamics, Rome, Italy, July 1992. Berlin: Springer 1993. p. 27–46.
- [25] Cebeci T, Smith AMO. Analysis of turbulent boundary layers. New York: Academic Press, 1974.
- [26] Baldwin B, Lomax H. Thin layer approximation and algebraic model for separated turbulent flow. AIAA Paper 78-257, 1978.
- [27] Degani D, Schiff L. Computation of turbulent supersonic flows around pointed bodies having crossflow separation. J Comput Phys 1986;66:173–96.
- [28] Martinelli L, Jameson A, Malfa E. Numerical simulation of three-dimensional vortex flows over delta wing configurations. In: Napolitano M, Solbetta F, editors. Proceedings of the 13th International Conference on Numerical Methods in Fluid Dynamics, Rome, Italy, July 1992. Berlin: Springer, 1993. p. 534–8.
- [29] Johnson D, King L. A mathematically simple turbulence closure model for attached and separated turbulent boundary layers. AIAA J 1985;23:1684–92.
- [30] Rumsey CL, Vatsa VN. A comparison of the predictive capabilities of several turbulence models using upwind and centered-difference computer codes. AIAA Paper 93-0192, AIAA 31st Aerospace Sciences Meeting, Reno, NV, January 1993.
- [31] Kao TJ, Su TY, Yu NJ. Navier–Stokes calculations for transport wing-body configurations with nacelles and struts. AIAA Paper 93-2945, AIAA 24th Fluid Dynamics Conference, Orlando, July 1993.
- [32] Jones WP, Launder BE. The calculation of low-Reynolds-number phenomena with a two-equation model of turbulence. Int J Heat Transfer 1973;16:1119–30.
- [33] Wilcox DC. A half a century historical review of the  $k$ - $\omega$  model. AIAA Paper 91-0615, AIAA 29th Aerospace Sciences Meeting, Reno, NV, January 1991.
- [34] Speziale CG, Anderson EC, Abid R. A critical evaluation of two-equation models for near wall turbulence. AIAA Paper 90-1481, June 1990.
- [35] Abid R, Speziale CG, Thangam S. Application of a new  $k$ - $\tau$  model to near wall turbulent flows. AIAA Paper 91-0614, AIAA 29th Aerospace Sciences Meeting, Reno, NV, January 1991.
- [36] Menter F. Zonal two-equation  $k$ - $\omega$  turbulence models for aerodynamic flows. AIAA Paper 93-2906, AIAA 24th Fluid Dynamics Meeting, Orlando, July 1993.
- [37] Coakley TJ. Numerical simulation of viscous transonic airfoil flows. AIAA Paper 87-0416, AIAA 25th Aerospace Sciences Meeting, Reno, NV, January 1987.
- [38] Smith BR. A near wall model for the  $k$ - $l$  two equation turbulence model. AIAA Paper 94-2386, AIAA 25th Fluid Dynamics Conference, Colorado Springs, CO, June 1994.
- [39] Baldwin BS, Barth TJ. A one-equation turbulence transport model for high Reynolds number wall-bounded flows. AIAA Paper 91-0610, AIAA 29th Aerospace Sciences Meeting, Reno, NV, January 1991.
- [40] Spalart P, Allmaras S. A one-equation turbulent model for aerodynamic flows. AIAA Paper 92-0439, AIAA 30th Aerospace Sciences Meeting, Reno, NV, January 1992.
- [41] Yakhot V, Orszag SA. Renormalization group analysis of turbulence. I. Basic theory. J Sci Comput 1986;1:3–51.
- [42] Smith LM, Reynolds WC. On the Yakhot–Orszag renormalization group for deriving turbulence statistics and models. Phys Fluids A 1992;4:364–90.
- [43] Martinelli L, Yakhot V. RNG-based turbulence transport approximations with applications to transonic flows. AIAA Paper 89-1950, AIAA Ninth Computational Fluid Dynamics Conference, Buffalo, NY, June 1989.
- [44] Melton JE, Pandya SA, Steger JL. 3D Euler flow solutions using unstructured Cartesian and prismatic grids. AIAA Paper 93-0331, Reno, NV, January 1993.
- [45] Samant SS, Bussioletti JE, Johnson FT, Burkhart RH, Everson BL, Melvin RG, Young DP, Erickson LL, Madson MD. TRANAIR: a computer code for transonic analyses of arbitrary configurations. AIAA Paper 87-0034, 1987.
- [46] Berger M, LeVeque RJ. An adaptive Cartesian mesh algorithm for the Euler equations in arbitrary geometries. AIAA Paper 89-1930, 1989.
- [47] Landsberg AM, Boris JP, Sandberg W, Young TR. Naval ship superstructure design: complex three-dimensional flows using an efficient, parallel method. High Performance Computing 1993: Grand Challenges in Computer Simulation, 1993.
- [48] Baker TJ. Mesh generation by a sequence of transformations. Appl Numer Math 1986;2:515–28.
- [49] Eiseman PR. A multi-surface method of coordinate generation. J Comput Phys 1979;33:118–50.
- [50] Eriksson LE. Generation of boundary-conforming grids around wing-body configurations using transfinite interpolation. AIAA J 1982;20:1313–20.
- [51] Smith RE. Three-dimensional algebraic mesh generation. Proceedings of the AIAA Sixth Computational Fluid Dynamics Conference, Danvers, MA, 1983. AIAA Paper 83-1904.

- [52] Thompson JF, Thames FC, Mastin CW. Automatic numerical generation of body-fitted curvilinear coordinate system for field containing any number of arbitrary two-dimensional bodies. *J Comput Phys* 1974;15: 299–319.
- [53] Thompson JF, Warsi ZUA, Mastin CW. Boundary-fitted coordinate systems for numerical solution of partial differential equations: a review. *J Comput Phys* 1982;47:1–108.
- [54] Sorenson RL. Elliptic generation of compressible three-dimensional grids about realistic aircraft. In: Hauser J, Taylor C, editors. *International Conference on Numerical Grid Generation in Computational Fluid Dynamics*, Landshut, F.R.G., 1986.
- [55] Sorenson RL. Three-dimensional elliptic grid generation for an F-16. In: Steger JL, Thompson JF, editors. *Three-dimensional grid generation for complex configurations: recent progress, 1988*. AGARDograph.
- [56] Steger JL, Chaussee DS. Generation of body-fitted coordinates using hyperbolic partial differential equations. *SIAM J Sci Stat Comput* 1980;1:431–7.
- [57] Weatherill NP, Forsey CA. Grid generation and flow calculations for aircraft geometries. *J Aircraft* 1985;22:855–60.
- [58] Sawada K, Takanashi S. A numerical investigation on wing/nacelle interferences of USB configuration. *AIAA Paper 87-0455*, AIAA 25th Aerospace Sciences Meeting, Reno, NV, January 1987.
- [59] Benek JA, Buning PG, Steger JL. A 3-D Chimera grid embedding technique. *AIAA Paper 85-1523*, AIAA 7th Computational Fluid Dynamics Conference, Cincinnati, OH, 1985.
- [60] Benek JA, Donegan TL, Suhs NE. Extended Chimera grid embedding scheme with applications to viscous flows. *AIAA Paper 87-1126*, AIAA 8th Computational Fluid Dynamics Conference, Honolulu, HI, 1987.
- [61] Delaunay B. Sur la sphere vide. *Bull Acad Sci USSR VII: Class Sci Mat Nat* 1934;793–800.
- [62] Voronoi G. Nouvelles applications des parametres continus a la theorie des formes quadratiques. *Deuxieme Memoire: Recherches sur les paralleloedres primitifs*. *J Reine Angew Math* 1908;134:198–287.
- [63] Lohner R, Parikh P. Generation of three-dimensional unstructured grids by the advancing front method. *AIAA Paper 88-0515*, Reno, NV, January 1988.
- [64] McCormack RW, Paullay AJ. Computational efficiency achieved by time splitting of finite difference operators. *AIAA Paper 72-154*, 1972.
- [65] Hall MG. Cell vertex multigrid schemes for solution of the Euler equations. *Proceedings of the IMA Conference on Numerical Methods for Fluid Dynamics*, Reading, April 1985.
- [66] Jameson A. A vertex based multigrid algorithm for three-dimensional compressible flow calculations. In: Tezduar TE, Hughes TJR, editors. *Numerical methods for compressible flow—finite difference, element and volume techniques*. New York: ASME Publication AMD 78, 1986.
- [67] Radespiel R, Rossow C, Swanson RC. An efficient cell-vertex multigrid scheme for the three-dimensional Navier–Stokes equations. *Proceedings of the AIAA Ninth Computational Fluid Dynamics Conference*, Buffalo, NY, June, 1989. p. 249–60. *AIAA Paper 89-1953-CP*.
- [68] Lax PD, Wendroff B. Systems of conservation laws. *Commun Pure Appl Math* 1960;13:217–37.
- [69] Lax PD. Hyperbolic systems of conservation laws and the mathematical theory of shock waves. *SIAM Regional Ser Appl Math* 1973;11.
- [70] Harten A. High resolution schemes for hyperbolic conservation laws. *J Comput Phys* 1983;49:357–93.
- [71] Godunov SK. A difference method for the numerical calculation of discontinuous solutions of hydrodynamic equations. *Mat Sb* 1959;47:271–306 (Translated as *JPRS* 7225 by U.S. Dept. of Commerce, 1960).
- [72] Steger JL, Warming RF. Flux vector splitting of the inviscid gas dynamic equations with applications to finite difference methods. *J Comput Phys* 1981;40:263–93.
- [73] Boris JP, Book DL. Flux corrected transport, I SHASTA, a fluid transport algorithm that works. *J Comput Phys* 1973;11:38–69.
- [74] Van Leer B. Towards the ultimate conservative difference scheme. II. Monotonicity and conservation combined in a second order scheme. *J Comput Phys* 1974;14:361–70.
- [75] Van Leer B. Flux vector splitting for the Euler equations. In: Krause E, editor. *Proceedings of the Eighth International Conference on Numerical Methods in Fluid Dynamics*, Aachen, 1982. p. 507–12.
- [76] Roe PL. Approximate Riemann solvers, parameter vectors, and difference schemes. *J Comput Phys* 1981;43:357–72.
- [77] Osher S, Solomon F. Upwind difference schemes for hyperbolic systems of conservation laws. *Math Comput* 1982;38:339–74.
- [78] Osher S, Chakravarthy S. High resolution schemes and the entropy condition. *SIAM J Numer Anal* 1984;21:955–84.
- [79] Sweby PK. High resolution schemes using flux limiters for hyperbolic conservation laws. *SIAM J Numer Anal* 1984;21:995–1011.
- [80] Anderson BK, Thomas JL, Van Leer B. A comparison of flux vector splittings for the Euler equations. *AIAA Paper 85-0122*, AIAA 23rd Aerospace Sciences Meeting, Reno, NV, January 1985.
- [81] Jameson A. Non-oscillatory shock capturing scheme using flux limited dissipation. In: Engquist BE, Osher S, Somerville RCJ, editors. *Large scale computations in fluid mechanics, Part 1, Lectures in Applied Mathematics*, vol. 22. Providence, RI: AMS, 1985. p. 345–70.
- [82] Yee HC. On symmetric and upwind TVD schemes. *Proceedings of the Sixth GAMM Conference on Numerical Methods in Fluid Mechanics*, Gottingen, September 1985.
- [83] Hughes TJR, Franca LP, Mallet M. A new finite element formulation for computational fluid dynamics, I, Symmetric forms of the compressible Euler and Navier–Stokes equations and the second law of thermodynamics. *Comput Methods Appl Mech Eng* 1986;59:223–31.
- [84] Woodward P, Colella P. The numerical simulation of two-dimensional fluid flow with strong shocks. *J Comput Phys* 1984;54:115–73.

- [85] Barth TJ, Jespersen DC. The design and application of upwind schemes on unstructured meshes. AIAA Paper 89-0366, AIAA 27th Aerospace Sciences Meeting, Reno, NV, January 1989.
- [86] Barth TJ, Frederickson PO. Higher order solution of the Euler equations on unstructured grids using quadratic reconstruction. AIAA Paper 90-0013, AIAA 28th Aerospace Sciences Meeting, January 1990.
- [87] Lax PD. Hyperbolic systems of conservation laws. SIAM Regional Ser Appl Math 1973;11.
- [88] Majda A, Osher S. Numerical viscosity and the entropy condition. Commun Pure Appl Math 1979;32:797–838.
- [89] Tadmor E. Numerical viscosity and the entropy condition for conservative difference schemes. Math Comput 1984;32:369–82.
- [90] Osher S. Riemann solvers, the entropy condition, and difference approximations. SIAM J Numer Anal 1984;121:217–35.
- [91] Osher S, Tadmor E. On the convergence of difference approximations to scalar conservation laws. Math Comput 1988;50:19–51.
- [92] Aiso H. Admissibility of difference approximations for scalar conservation laws. Hiroshima Math J 1993;23:15–61.
- [93] Jameson A, Schmidt W, Turkel E. Numerical solution of the Euler equations by finite volume methods using Runge-Kutta time stepping schemes. AIAA Paper 81-1259, June 1981.
- [94] Swanson RC, Turkel E. On central-difference and upwind schemes. J Comput Phys 1992;101:297–306.
- [95] Jameson A. Analysis and design of numerical schemes for gas dynamics 1, artificial diffusion, upwind biasing, limiters and their effect on multigrid convergence. Int J Comput Fluid Dyn 1995;4:171–218.
- [96] Venkatakrishnan V. Convergence to steady state solutions of the Euler equations on unstructured grids with limiters. AIAA Paper 93-0880, AIAA 31st Aerospace Sciences Meeting, Reno, NV, January 1993.
- [97] Jameson A. Artificial diffusion, upwind biasing, limiters and their effect on accuracy and multigrid convergence in transonic and hypersonic flows. AIAA Paper 93-3359, AIAA 11th Computational Fluid Dynamics Conference, Orlando, FL, July 1993.
- [98] Rao SV, Deshpande SM. A class of efficient kinetic upwind methods for compressible flows. Report, 91 FM 11, Indian Institute of Science, 1991.
- [99] Balakrishnan N, Deshpande SM. New upwind schemes with wave-particle splitting for inviscid compressible flows. Report 91 FM 12, Indian Institute of Science, 1991.
- [100] Liou M-S, Steffen CJ. A new flux splitting scheme. J Comput Phys 1993;107:23–39.
- [101] Wada Y, Liou M-S. A flux splitting scheme with high-resolution and robustness for discontinuities. AIAA Paper 94-0083, AIAA 32nd Aerospace Sciences Meeting, Reno, NV, January 1994.
- [102] Jameson A. Analysis and design of numerical schemes for gas dynamics 2, artificial diffusion and discrete shock structure. Int J Comput Fluid Dyn 1995;5:1–38.
- [103] Chakravarthy SR, Harten A, Osher S. Essentially non-oscillatory shock capturing schemes of uniformly very high accuracy. AIAA Paper 86-0339, AIAA 24th Aerospace Sciences Meeting, Reno, NV, January 1986.
- [104] Shu CW, Zang TA, Erlebacher G, Whitaker D, Osher S. High-order ENO schemes applied to two- and three-dimensional compressible flow. Appl Numer Math 1992;9:45–71.
- [105] Shu CW, Osher S. Efficient implementation of essentially non-oscillatory shock-capturing schemes. J Comput Phys 1988;77:439–71.
- [106] Shu CW, Osher S. Efficient implementation of essentially non-oscillatory shock-capturing schemes II. J Comput Phys 1989;83:32–78.
- [107] Deshpande SM. On the Maxwellian distribution, symmetric form and entropy conservation for the Euler equations. NASA TP 2583, 1986.
- [108] Croisille JP, Villedieu P. Kinetic flux splitting schemes for hypersonic flows. In: Napolitano M, Sobetta F, editors. Proceedings of the 13th International Congress on Numerical Methods in Fluid Dynamics, Rome. Berlin: Springer, July 1992. p. 310–3.
- [109] Eppard W, Grossman B. A multi-dimensional kinetic-based upwind solver for the Euler equations. AIAA Paper 93-3303, AIAA 11th Computational Fluid Dynamics Conference, Orlando, FL, July 1993.
- [110] Prendergast K, Xu K. Numerical hydrodynamics from gas kinetic theory. J Comput Phys 1993;109:53–66.
- [111] Xu K, Martinelli L, Jameson A. Gas-kinetic finite volume methods, flux-vector splitting and artificial diffusion. J Comput Phys 1995;120:48–65.
- [112] Hirsch C, Lacol C, Deconinck H. Convection algorithms based on a diagonalization procedure for the multi-dimensional Euler equations. AIAA Paper 87-1163, AIAA 8th Computational Fluid Dynamics Conference, Hawaii, June 1987.
- [113] Powell KG, van Leer B. A genuinely multidimensional upwind cell-vertex scheme for the Euler equations. AIAA Paper 89-0095, AIAA 27th Aerospace Sciences Meeting, Reno, NV, January 1989.
- [114] Van Leer B. Progress in multi-dimensional upwind differencing. In: Napolitano M, Solbetta F, editors. Proceedings of the 13th International Conference on Numerical Methods in Fluid Dynamics, Rome, July 1992. Berlin: Springer, 1993. p. 1–26.
- [115] Deconinck H, Paillère H, Struijs R, Roe PL. Multi-dimensional upwind schemes based on fluctuation-splitting of conservation laws. Comput Mech 1993; 11:323–40.
- [116] Sidilkover D. Multi-dimensional upwinding and multigrid. AIAA Paper 95-1759, AIAA 12th Computational Fluid Dynamics Conference, San Diego, CA, June 1995.
- [117] Paillère H, Deconinck H. A review of multi-dimensional upwind residual distribution schemes for the Euler equations. In: Hafez M, Oshima K, editors. Computational fluid dynamics review 1995. New York: Wiley, 1995. p. 141–60.
- [118] Hirsch C, Van Ransbeeck P. Multi-dimensional upwinding and artificial dissipation. In: Caughey DA, Hafez MM, editors. Frontiers of computational fluid dynamics 1994. Technical Report. New York: Wiley, 1994. p. 597–626.

- [119] Jayaram M, Jameson A. Multigrid solution of the Navier–Stokes equations for flow over wings. AIAA Paper 88-0705, AIAA 26th Aerospace Sciences Meeting, Reno, NV, January 1988.
- [120] Rieger H, Jameson A. Solution of steady three-dimensional compressible Euler and Navier–Stokes equations by an implicit LU scheme. AIAA Paper 88-0619, AIAA 26th Aerospace Sciences Meeting, Reno, NV, January 1988.
- [121] Liu F, Jameson A. Multigrid Navier–Stokes calculations for three-dimensional cascades. AIAA Paper 92-0190, AIAA 30th Aerospace Sciences Meeting, Reno, NV, January 1992.
- [122] Parthasarathy V, Kallinderis Y, Nakajima K. A hybrid adaptation method and directional viscous multigrid with prismatic-tetrahedral meshes. AIAA Paper 95-0670, AIAA 33rd Aerospace Sciences Meeting, Reno, Nevada, January 1995.
- [123] Venkatakrishnan V. A perspective on unstructured grid flow solvers. AIAA J 1996;34:533–47.
- [124] Venkatakrishnan V. Newton solution of inviscid and viscous problems. AIAA Paper 88-0413, AIAA 26th Aerospace Sciences Meeting, Reno, NV, January 1988.
- [125] Giles M, Drela M, Thompson WT. Newton solution of direct and inverse transonic Euler equations. AIAA Paper 85-1530, Cincinnati, 1985.
- [126] Beam RW, Warming RF. An implicit finite difference algorithm for hyperbolic systems in conservation form. J Comput Phys 1976;23:87–110.
- [127] Pulliam TH, Steger JL. Implicit finite difference simulations of three-dimensional compressible flow. AIAA J 1980;18:159–67.
- [128] Hassan O, Morgan K, Peraire J. An adaptive implicit/explicit finite-element method for high speed flows. AIAA Paper 89-0363, AIAA 27th Aerospace Sciences Meeting, Reno, NV, January 1989.
- [129] Lohner R, Martin D. An implicit linelet-based solver for incompressible flows. AIAA Paper 92-0668, AIAA 30th Aerospace Sciences Meeting, Reno, NV, January 1992.
- [130] Jameson A, Turkel E. Implicit schemes and LU decompositions. Math Comput 1981;37:385–97.
- [131] Obayashi S, Kuwakara K. LU factorization of an implicit scheme for the compressible Navier–Stokes equations. AIAA Paper 84-1670, AIAA 17th Fluid Dynamics and Plasma Dynamics Conference, Snowmass, CO, June 1984.
- [132] Chakravarthy SR. Relaxation methods for unfactored implicit upwind schemes. AIAA Paper 84-0165, AIAA 22nd Aerospace Sciences Meeting, Reno, NV, January 1984.
- [133] Yoon S, Jameson A. Lower-upper Symmetric-Gauss–Seidel method for the Euler and Navier–Stokes equations. AIAA Paper 87-0600, AIAA 25th Aerospace Sciences Meeting, Reno, NV, January 1987.
- [134] Chipman R, Jameson A. Fully conservative numerical solutions for unsteady irrotational transonic flow about airfoils. AIAA Paper 79-1555, AIAA 12th Fluid and Plasma Dynamics Conference, Williamsburg, VA, July 1979.
- [135] Jameson A. Multigrid algorithms for compressible flow calculations. Second European Conference on Multigrid Methods, Cologne, Princeton University Report MAE 1743, October 1985.
- [136] Jameson A. Transonic flow calculations for aircraft. In: Brezzi F, editor. *Lecture Notes in Mathematics, Numerical Methods in Fluid Dynamics*. Berlin: Springer, 1985. p. 156–242.
- [137] Rizzi A, Eriksson LE. Computation of flow around wings based on the Euler equations. J Fluid Mech 1984;148:45–71.
- [138] Fedorenko RP. The speed of convergence of one iterative process. USSR Comput Math Math Phys 1964;4:227–35.
- [139] Brandt A. Multi-level adaptive solutions to boundary value problems. Math Comput 1977;31:333–90.
- [140] Hackbusch W. On the multi-grid method applied to difference equations. Computing 1978;20:291–306.
- [141] Ni RH. A multiple grid scheme for solving the Euler equations. AIAA J 1982;20:1565–71.
- [142] Jameson A. Solution of the Euler equations by a multigrid method. Appl Math Comput 1983;13:327–56.
- [143] Caughey DA. A diagonal implicit multigrid algorithm for the Euler equations. AIAA Paper 87-453, AIAA 25th Aerospace Sciences Meeting, Reno, NV, January 1987.
- [144] Anderson WK, Thomas JL, Whitfield DL. Multigrid acceleration of the flux split Euler equations. AIAA Paper 86-0274, AIAA 24th Aerospace Sciences Meeting, Reno, NV, January 1986.
- [145] Hemker PW, Spekreijse SP. Multigrid solution of the steady Euler equations. Proceedings of the Oberwolfach Meeting on Multigrid Methods, December 1984.
- [146] Mulder WA. A new multigrid approach to convection problems. J Comput Phys 1989;83:303–23.
- [147] Mulder WA. A high-resolution Euler solver based on multigrid, semi-coarsening, and defect correction. J Comput Phys 1992;100:91–104.
- [148] Allmaras S. Analysis of a local matrix preconditioner for the 2-D Navier–Stokes equations. AIAA Paper 93-3330, AIAA 11th Computational Fluid Dynamics Conference, Orlando, FL, July 1993.
- [149] Allmaras S. Analysis of semi-implicit preconditioners for multigrid solution of the 2-D Navier–Stokes equations. AIAA Paper 95-1651, AIAA 12th Computational Fluid Dynamics Conference, San Diego, CA, June 1995.
- [150] Allmaras S. Algebraic smoothing analysis of multigrid methods for the 2-D compressible Navier–Stokes equations. AIAA Paper 97-1954, AIAA 13th Computational Fluid Dynamics Conference, Snowmass, CO, July, 1997.
- [151] Pierce NA, Giles MB. Preconditioning compressible flow calculations on stretched meshes. AIAA Paper 96-0889, AIAA 34th Aerospace Sciences Meeting, Reno, NV, January 1996.
- [152] Pierce NA, Giles MB, Jameson A, Martinelli L. Accelerating three-dimensional Navier–Stokes calculations. AIAA Paper 97-1953, AIAA 13th Computational Fluid Dynamics Conference, Snowmass, CO, July 1997.
- [153] Jameson A, Mavriplis DJ. Multigrid solution of the Euler equations on unstructured and adaptive grids. In: McCormick S, editor. *Multigrid methods, theory, applications and supercomputing, Lecture Notes in Pure and Applied Mathematics*, vol 110. April 1987. p. 413–30.

- [154] Peraire J, Peirö J, Morgan K. A 3D finite-element multigrid solver for the Euler equations. AIAA Paper 92-0449, AIAA 30th Aerospace Sciences Conference, Reno, NV, January 1992.
- [155] Lallemand MH, Dervieux A. A multigrid finite-element method for solving the two-dimensional Euler equations. In: McCormick SF, editor. Proceedings of the Third Copper Mountain Conference on Multigrid Methods, Lecture Notes in Pure and Applied Mathematics, Copper Mountain, April 1987. p. 337–63.
- [156] Lallemand MH, Steve H, Dervieux A. Unstructured multigriding by volume aggregation: Current status. *Comput Fluids* 1992;21:397–433.
- [157] Mavriplis DJ, Venkatakrishnan V. A 3D agglomeration multigrid solver for the Reynolds-averaged Navier–Stokes equations on unstructured meshes. *Int J Numer Methods Fluids* 1996;23:1–18.
- [158] Crumpton PI, Giles MB. Implicit time accurate solutions on unstructured dynamic grids. AIAA Paper 95-1671, AIAA 12th Computational Fluid Dynamics Conference, San Diego, CA, June 1995.
- [159] Jameson A. Time dependent calculations using multigrid, with applications to unsteady flows past airfoils and wings. AIAA Paper 91-1596, AIAA 10th Computational Fluid Dynamics Conference, Honolulu, Hawaii, June 1991.
- [160] Dahlquist G. A special stability problem for linear multi-step methods. *BIT* 1963;3:27–43.
- [161] Gear CW. The numerical integration of stiff ordinary differential equations. Report 221, University of Illinois Department of Computer Science, 1967.
- [162] Melson ND, Sanetrik MD, Atkins HL. Time-accurate Navier–Stokes calculations with multigrid acceleration. Proceedings of the Sixth Copper Mountain Conference on Multigrid Methods, Copper Mountain, April 1993.
- [163] Alonso JJ, Jameson A. Fully-implicit time-marching aeroelastic solutions. AIAA Paper 94-0056, AIAA 32nd Aerospace Sciences Meeting, Reno, NV, January, 1994.
- [164] Alonso JJ, Martinelli L, Jameson A. Multigrid unsteady Navier–Stokes calculations with aeroelastic applications. AIAA Paper 95-0048, AIAA 33rd Aerospace Sciences Meeting, Reno, NV, January 1995.
- [165] Belov A, Martinelli L, Jameson A. A new implicit algorithm with multigrid for unsteady incompressible flow calculations. AIAA Paper 95-0049, AIAA 33rd Aerospace Sciences Meeting, Reno, NV, January 1995.
- [166] Venkatakrishnan V, Mavriplis DJ. Implicit method for the computation of unsteady flows on unstructured grids. *J Comput Phys* 1996;127:380–97.
- [167] Van Leer B, Lee WT, Roe PL. Characteristic time stepping or local preconditioning of the Euler equations. AIAA Paper 91-1552, AIAA 10th Computational Fluid Dynamics Conference, Honolulu, Hawaii, June 1991.
- [168] Turkel E. Preconditioned methods for solving the incompressible and low speed equations. *J Comput Phys* 1987;72:277–98.
- [169] Mavriplis DJ. Multigrid strategies for viscous flow solvers on anisotropic unstructured meshes. AIAA Paper 97-1952, AIAA 13th Computational Fluid Dynamics Conference, Snowmass, CO, July 1997.
- [170] Shlomo Ta'asan. Canonical forms of multidimensional, steady inviscid flows. ICASE Report 93-34, Institute for Computer Applications in Science and Engineering, Hampton, VA, 1993.
- [171] Sidilkover D. Some approaches towards constructing optimally efficient multigrid solvers for the inviscid flow equations. ICASE Report 97-39, ICASE, August 1997.
- [172] Roberts TW, Sidilkover D, Swanson RC. Textbook multigrid efficiency for the steady Euler equations. AIAA Paper 97-1949, AIAA 13th Computational Fluid Dynamics Conference, Snowmass, CO, July 1997.
- [173] Rai MM, Moin P. Direct numerical simulation of transition and turbulence in a spatially evolving boundary layer. AIAA Paper 91-1607 CP, AIAA 10th Computational Fluid Dynamics Conference, Honolulu, HI, June 1991.
- [174] Lele SK. Compact finite difference schemes with spectral-like resolution, CTR Manuscript 107, 1990.
- [175] Carpenter MH, Gottlieb D, Abarbanel S. Time-stable boundary conditions for finite-difference schemes solving hyperbolic systems: methodology and application to high-order compact schemes. ICASE Report 93-9, Hampton, VA, March 1993.
- [176] Orszag S, Gottlieb D. Numerical analysis of spectral methods. *SIAM Regional Ser Appl Math* 1977;26.
- [177] Canuto C, Hussaini MY, Quarteroni A, Zang DA. Spectral methods in fluid dynamics. Berlin: Springer, 1987.
- [178] Karniadakis GE, Orszag SA. Nodes, modes and flow codes. *Phys Today* 1993;34–42.
- [179] Berger M, Jameson A. Automatic adaptive grid refinement for the Euler equations. *AIAA J* 1985;23:561–8.
- [180] Dannenhoffer JF, Baron JR. Robust grid adaptation for complex transonic flows. AIAA Paper 86-0495, AIAA 24th Aerospace Sciences Meeting, Reno, NV, January 1986.
- [181] Lohner R, Morgan K, Peraire J. Improved adaptive refinement strategies for the finite element aerodynamic configurations. AIAA Paper 86-0499, AIAA 24th Aerospace Sciences Meeting, Reno, NV, January 1986.
- [182] Holmes DG, Lamson SH. Adaptive triangular meshes for compressible flow solutions. Proceedings First International Conference on Numerical Grid Generation in Computational Fluid Dynamics, Landshut, FRG, July 1986. p. 413–24.
- [183] Quirk JJ. An alternative to unstructured grids for computing gas dynamics flows about arbitrarily complex two-dimensional bodies. ICASE Report 92-7, Hampton, VA, February, 1992.
- [184] Lefebvre D, Peraire J, Morgan K. Finite element least squares solutions of the Euler equations using linear and quadratic approximations. *Int J Comput Fluid Dyn* 1993;1:1–23.
- [185] Peraire J, Peirö J, Morgan K. Adaptive remeshing for three-dimensional compressible flow computations. *J Comput Phys* 1992;103(2):269–85.
- [186] Busch Jr RJ. Computational fluid dynamics in the design of the Northrop/McDonnell Douglas YF-23 ATF prototype. AIAA Paper 91-1627, AIAA 21st Fluid Dynamics, Plasmadynamics & Lasers Conference, Honolulu, Hawaii, 1991.

- [187] Cliff SE, Thomas SD. Euler/experimental correlations of sonic boom pressure signatures. AIAA Paper 91-3276, AIAA 9th Applied Aerodynamics Conference, Baltimore, September 1991.
- [188] Cummings RM, Rizk YM, Schiff LB, Chaderjian NM. Navier–Stokes predictions for the F-18 wing and fuselage at large incidence. *J Aircraft* 1992;29:565–74.
- [189] Farmer J, Martinelli L, Jameson A, Cowles G. Fully-nonlinear CFD techniques for ship performance analysis and design. AIAA Paper 95-1690, AIAA 12th Computational Fluid Dynamics Conference, San Diego, CA, June 1995.
- [190] Lions JL. Optimal control of systems governed by partial differential equations. New York: Springer, 1971 (Translated by S.K. Mitter).
- [191] Jameson A. Aerodynamic design via control theory. *J Sci Comput* 1988;3:233–60.
- [192] Jameson A. Automatic design of transonic airfoils to reduce the shock induced pressure drag. In: Proceedings of the 31st Israel Annual Conference on Aviation and Aeronautics, Tel Aviv, February 1990. p. 5–17.
- [193] Jameson A. Optimum aerodynamic design via boundary control. AGARD FDP/Von Karman Institute Lecture Notes on Optimum Design Methods in Aerodynamics. AGARD Report 803, 1994. p. 3-1–3-33.
- [194] Pironneau O. Optimal shape design for elliptic systems. New York: Springer, 1984.
- [195] Pironneau O. Optimal shape design for aerodynamics. AGARD FDP/Von Karman Institute Lecture Notes on Optimum Design Methods in Aerodynamics, AGARD Report 803, 1994. p. 6-1–6-40.
- [196] Baysal O, Elshaky ME. Aerodynamic design optimization using sensitivity analysis and computational fluid dynamics. AIAA Paper 91-0471, 29th Aerospace Sciences Meeting, Reno, NV, January 1991.
- [197] Ta'asan S, Kuruvila G, Salas MD. Aerodynamic design and optimization in one shot. AIAA Paper 92-005, 30th Aerospace Sciences Meeting and Exhibit, Reno, NV, January 1992.
- [198] Cabuk H, Shung CH, Modi V. Adjoint operator approach to shape design for internal incompressible flow. In: Dulikravich GS, editor. Proceedings of the Third International Conference on Inverse Design and Optimization in Engineering Sciences, 1991. p. 391–404.
- [199] Huan JC, Modi V. Optimum design for drag minimizing bodies in incompressible flow. *Inverse Problems Eng* 1994;1:1–25.
- [200] Desai M, Ito K. Optimal controls of Navier–Stokes equations. *SIAM J Control Optim* 1994;32(5):1428–46.
- [201] Anderson WK, Venkatakrishnan V. Aerodynamic design and optimization on unstructured grids with a continuous adjoint formulation, AIAA Paper 97-0643, AIAA 35th Aerospace Sciences Meeting, Reno, NV, January 1997.
- [202] Elliot J, Peraire J. Practical 3D aerodynamic design and optimization using unstructured meshes. AIAA Paper 96-4710, 6th AIAA/NASA/USAF Multidisciplinary and Optimization Symposium, Seattle, WA, September 1996.
- [203] Jameson A, Martinelli L, Pierce NA. Optimum aerodynamic design using the Navier–Stokes equations. *Theoret Computat Fluid Dyn* 1998;10:213–37.
- [204] Jameson A, Alonso JJ, Reuther J, Martinelli L, Vassberg JC. Aerodynamic shape optimization techniques based on control theory. AIAA Paper 98-2538, AIAA 29th Fluid Dynamics Conference, Albuquerque, NM, June 1998.
- [205] Reuther J, Jameson A. Aerodynamic shape optimization of wing and wing-body configurations using control theory. AIAA Paper 95-0213, AIAA 33rd Aerospace Sciences Meeting and Exhibit, Reno, NV, January 1995.
- [206] Jameson A. Optimum aerodynamic design using the Control Theory. *Comput Fluid Dyn Rev* 1995;495–528.
- [207] Gallman J, Reuther J, Pfeiffer N, Forrest W, Bernstorff D. Business jet wing design using aerodynamic shape optimization. AIAA Paper 96-0554, 34th Aerospace Sciences Meeting and Exhibit, Reno, Nevada, January 1996.
- [208] Reuther J, Alonso JJ, Rimlinger MJ, Jameson A. Aerodynamic shape optimization of supersonic aircraft configurations via an adjoint formulation on parallel computers. AIAA Paper 96-4045, 6th AIAA/NASA/ISSMO Symposium on Multidisciplinary Analysis and Optimization, Bellevue, WA, September 1996.